Politécnica
UFRJ

AN ARBITRARY LAGRANGIAN-EULERIAN FINITE ELEMENT METHOD FOR VORTEX-INDUCED VIBRATIONS PREDICTION

Gabriel de Lucas Garden

Projeto de Graduação apresentado ao Curso de Engenharia Mecânica da Escola Politécnica, Universidade Federal do Rio de Janeiro, como parte dos requisitos necessários à obtenção do título de Engenheiro.

Orientadores: Gustavo Rabello dos Anjos
Su Jian

Rio de Janeiro
Setembro de 2025

UNIVERSIDADE FEDERAL DO RIO DE JANEIRO

Escola Politécnica

Departamento de Engenharia Mecânica

MÉTODO DOS ELEMENTOS FINITOS SOB UMA ABORDAGEM LAGRANGIANA-EULERIANA ARBITRÁRIA PARA A PREDIÇÃO DA VIBRAÇÃO INDUZIDA POR VÓRTICES

Gabriel de Lucas Garden

PROJETO FINAL SUBMETIDO AO CORPO DOCENTE DO DEPARTAMENTO DE ENGENHARIA MECÂNICA DA ESCOLA POLITÉCNICA DA UNIVERSIDADE FEDERAL DO RIO DE JANEIRO COMO PARTE DOS REQUISITOS NECESSÁRIOS PARA A OBTENÇÃO DO GRAU DE ENGENHEIRO MECÂNICO.

Aprovada por:

_____

Prof. Gustavo Rabello dos Anjos, Ph.D.

_____

Prof. Su Jian, D.Sc.

_____

Prof. Marcelo Amorim Savi, D.Sc.

_____

Prof. Daniel Alves Castello, D.Sc.

RIO DE JANEIRO, RJ – BRASIL

SETEMBRO DE 2025

de Lucas Garden, Gabriel

Método dos Elementos Finitos sob uma Abordagem Lagrangiana-Euleriana Arbitrária para a Predição da Vibração Induzida por Vórtices/ Gabriel de Lucas Garden. – Rio de Janeiro: UFRJ/Escola Politécnica, 2025.

XIX, 87 p.: il.; 29, 7cm.

Orientadores: Gustavo Rabello dos Anjos

Su Jian

Projeto de Graduação – UFRJ/ Escola Politécnica/ Curso de Engenharia Mecânica, 2025.

Bibliography: p. 68 – 70.

1. FEM. 2. ALE. 3. VIV. 4. Unconditionally stable. I. Rabello dos Anjos, Gustavo *et al.*. II. Universidade Federal do Rio de Janeiro, UFRJ, Curso de Engenharia Mecânica. III. Método dos Elementos Finitos sob uma Abordagem Lagrangiana-Euleriana Arbitrária para a Predição da Vibração Induzida por Vórtices.

"The main thing is to be yourself and not allow people to disturb you and change you."
Ayrton Senna

Acknowledgements

First and foremost, I would like to express my deepest gratitude to my advisors Prof. Gustavo Rabello dos Anjos and Prof. Su Jian. Without their guidance I would not have been able to develop this work. In addition, a special thanks goes to Prof. Gustavo for the numerous discussions we have had during the development of the numerical code. Thank you both for your continued support.

Following that, I would like to say thank you to the colleagues and friends I have made during my undergraduate course. I am sure that without you my time spent at the University would have been worse. So thank you for enduring the undergraduate course alongside me.

Next, I would like to thank my friends and colleagues from LASME, the research laboratory in which I spent the past two and a half years. The amount of experience I got from my time as an undergraduate research student is immeasurable. I got to travel to new places in order to learn new things as well as present the work I developed during my time at the laboratory. A bonus from these trips was that I had the pleasure of meeting new people working on different subjects which is always nice to hear about. And I would also like to say a special thank you to the ones who know who they are for making the days at the lab better.

Last but not least, I would like to express my gratitude to my parents for allowing me to make my own choices. And more importantly, thank you both for your love and support during my undergraduate studies.

Resumo do Projeto de Graduação apresentado à Escola Politécnica/UFRJ como parte dos requisitos necessários para a obtenção do grau de Engenheiro Mecânico

MÉTODO DOS ELEMENTOS FINITOS SOB UMA ABORDAGEM LAGRANGIANA-EULERIANA ARBITRÁRIA PARA A PREDIÇÃO DA VIBRAÇÃO INDUZIDA POR VÓRTICES

Gabriel de Lucas Garden

Setembro/2025

Orientadores: Gustavo Rabello dos Anjos
Su Jian

Departamento: Engenharia Mecânica

Para estudar as vibrações induzidas por vórtices (VIV), um método numérico é proposto para resolver as equações de Navier Stokes. As equações bidimensionais da dinâmica de fluidos são descritas em uma formulação Lagrangiana-Euleriana arbitrária (ALE) e discretizadas espacialmente usando o Método dos Elementos Finitos (FEM), no qual o elemento quadrilateral Mini foi empregado para satisfazer a condição de Ladyzhenskaya–Babuška–Brezzi (LBB). Já a discretização temporal é obtida por meio de um método Semi-Lagrangiano (SL) explícito de primeira ordem. Além disso, um procedimento de busca e interpolação computacionalmente eficiente é adotado para dar suporte ao esquema SL. O código computacional desenvolvido funciona com malhas quadrilaterais estruturadas ou não estruturadas devido a uma biblioteca de integração Gaussiana. Diversos problemas de referência foram simulados para validar adequadamente a implementação da metodologia. Além disso, foram realizadas simulações de oscilação forçada e livre para estudar o VIV de fluxo cruzado, enquanto o cilindro suportado elasticamente foi simulado sob diversas condições para estudar as vibrações em linha e transversais do corpo rígido em função do número de Reynolds.

Abstract of Undergraduate Project presented to POLI/UFRJ as a partial fulfillment of the requirements for the degree of Mechanical Engineer

AN ARBITRARY LAGRANGIAN-EULERIAN FINITE ELEMENT METHOD FOR VORTEX-INDUCED VIBRATIONS PREDICTION

Gabriel de Lucas Garden

September/2025

Advisors: Gustavo Rabello dos Anjos
Su Jian

Department: Mechanical Engineering

Vortex-induced vibration (VIV) is a well-known problem in the offshore industry, especially when dealing with riser dynamics. This issue arises due to the nonlinear interaction between the fluid flow past cylindrical structures, which generate a von Karman vortex street. The flow of fluids around blunt objects creates a wake behind the geometry, which excites the structure, making it oscillate in the transverse and longitudinal directions of the flow. To accurately model the intricate dynamics of this phenomenon, this work employs the bidimensional incompressible Navier-Stokes equations within the arbitrary Lagrangian-Eulerian (ALE) framework. The finite element method (FEM) has been chosen to discretize the equations and the five-noded quadrilateral was used to discretize the fluid domain, which automatically satisfies the Ladyzhenskaya–Babuška–Brezzi (LBB) condition. In order to stabilize the numerical code for higher Reynolds numbers, a first-order semi-Lagrangian (SL) scheme has been used. This method is unconditionally stable thus, large time steps may be used if necessary. The search-interpolation algorithm is remarkably efficient since it starts by inquiring about one of the node's neighbouring elements. On the other hand, the solid structure was considered a rigid body therefore, its boundary was non-deformable. Several benchmark test cases have been investigated to confirm

the accuracy of the proposed methodology. As for results, forced and free oscillation simulations were conducted to study cross-flow VIV. While the elastically supported cylinder was simulated under different Reynolds numbers to investigate both in-line and transverse vibrations of the rigid body.

Contents

List of Figures

List of Tables

Nomenclature

Roman letters

$\hat{\mathbf{c}}$	Convective velocity vector
c_d	Drag coefficient
c_l	Lift coefficient
$\mathbf{d}^e$	Element divergent matrix
D	Diameter
$\mathbf{D}$	Divergent matrix
$\mathbf{E}$	Strain rate tensor
f_s	Vortex shedding frequency
$\mathbf{F}$	Force vector
Fr	Froude number
$\mathbf{g}$	Gravity
$\mathbf{g}^e$	Element gradient matrix
$\mathbf{G}$	Gradient matrix
$\mathbf{G_v}$	Velocity gradient matrix
$\mathbf{I}$	Identity matrix
$\mathbf{k}^e$	Element stiffness matrix
$\mathbf{K}$	Stiffness matrix
L	Characteristic length
L_k	Pressure shape function
m^*	Non-dimensional mass
$\mathbf{m}^e$	Element mass matrix
$\mathbf{M}$	Mass matrix
$\mathbf{M}_\Gamma$	Boundary mass matrix

$\mathbf{n}$	Normal vector
$\hat{\mathbf{n}}_i$	Nodal normal vector
N_i	Velocity shape function
p	Pressure
q	Pressure test function
Re	Reynolds number
St	Strouhal number
t	Time
U	Free-stream velocity
$\mathbf{v}$	Velocity vector
$\hat{\mathbf{v}}$	Mesh velocity vector
$\mathbf{v}_\Gamma$	Boundary velocity
V	Volume
$\mathbf{w}$	Velocity test function
$\mathbf{x}$	Spatial coordinates vector
$\mathbf{x}_d$	Departure point

Greek letters

Γ	Boundary
δ	Kronecker delta
Δt	Time step
ζ	Damping ratio
η	Natural coordinate
μ	Dynamic viscosity
ν	Kinematic viscosity
ξ	Natural coordinate
ρ	Fluid density
$\boldsymbol{\sigma}$	Stress tensor
$\boldsymbol{\tau}$	Viscous stress tensor
Ω	Fluid domain

Chapter 1

Introduction

In this introductory chapter, a brief historical overview on the oil/gas and offshore industries is presented. Then the physical problem of interest and objective of this work are formally introduced. Finally, this chapter ends with the organization of the whole work.

1.1 Motivation

According to the International Energy Agency, as of 2022, the net income of the global oil and gas industry surpassed the mark of USD 4 trillion in net income. Such high income suggests that, despite the increasing search for alternative energy sources, oil and gas still are very much at the forefront of this global sector, and shows no signs of slowing down any time soon.

Its history, however began more than four thousand years ago. Although it was not until 1847, when a Scottish chemist by the name of James Young, noticed a seepage inside a coal mine that the industry began to take shape into what it has become nowadays. Even so, the first commercial oil well came twelve years after Young's discovery, in Pennsylvania.

The oil industry however, would only install the first offshore drilling and production unit in 1947 around 28 km away from the coast of Louisiana, in the Gulf of Mexico. Later, in 1961, the first semi-submersible platform appeared, the Blue Water Rig No. 1, which was operated by Shell, Fig. 1.1. This rig spudded an record-setting offshore well in 91 meters of water in the Gulf of Mexico. As time

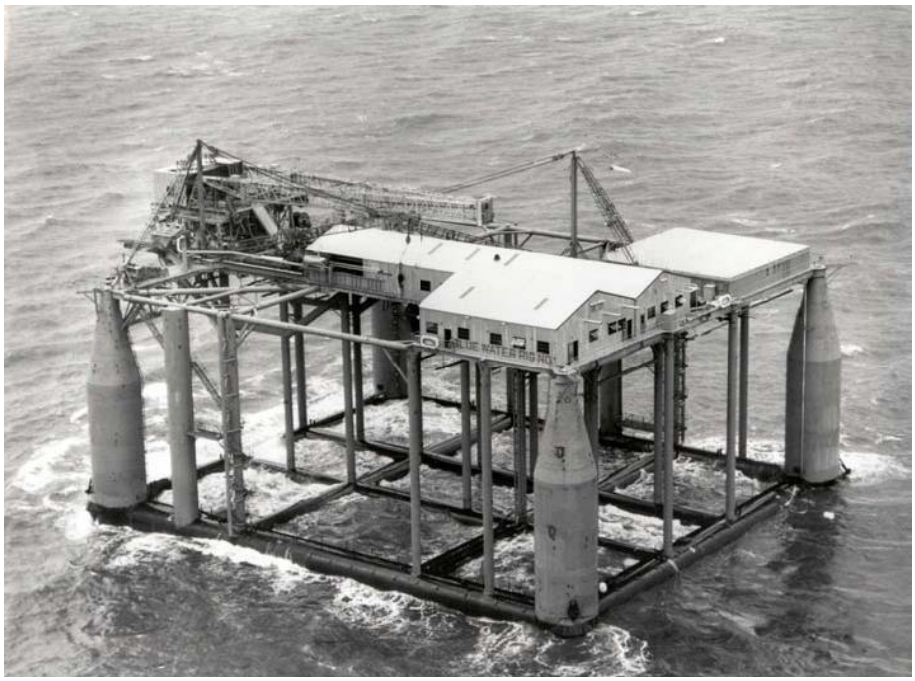

Figure 1.1: Blue Water Rig No. 1, operated by Shell in 1962. (Source: Wikipedia)

went by, the search for oil and gas reservoirs in increasingly deeper waters presented new challenges to the industry.

The pipe that connects the wellhead to the offshore platform is known as a marine riser. A marine riser can be subdivided into two categories: drilling and production. The first is a vertical pipe that guides the drill bit during the drilling operation. The later, are used to transfer crude oil from the subsea wellhead to the offshore facility, Chandrasekaran [10]. Since the depths of these wells began to steadily increase over the years, the length of these pipes followed and they became more susceptible to the deep-water currents. This environmental condition generated concern with regards to vortex-induced vibrations (VIV) of these structures, since they are now subjected to vibration related failure, Vandiver [11]. In order to avoid environmental damages and financial loss due to this fluid-structure interaction (FSI), the accurate prediction of VIV became extremely important.

FSI is a multi-physics subject that is observed in man-made and natural systems. This phenomenon is commonly found in aerospace, ocean, biomedical and civil engineering fields. With respect to offshore industry, a specific type of FSI is well-known, the VIV, as it can greatly influence riser structural dynamics, Williamson and Govardhan [12]. Owing to the fact that as the vortex shedding phenomenon occurs,

oscillating body forces appear, which in turn, induces vibrations on the immersed body. In the context of riser dynamics, when subjected to extreme environmental conditions, these vibrations may lead to structural failure due to mechanical fatigue as previously mentioned.

1.2 Objective

The objective of this work was to develop a computational code in order to simulate VIV. The finite element method (FEM) is used to discretize the governing equations for an incompressible Newtonian fluid. While the arbitrary Lagrangian-Eulerian (ALE) framework is used to allow for a moving mesh scheme. This allows for the dynamics of the rigid body to evolve throughout the simulation seamlessly. Moreover, a first-order semi-Lagrangian method was also used to allow for the simulation of higher Reynolds number with the benefit that this scheme is unconditionally stable regardless of the time step.

1.3 Organization

The contents of this work are organized as follows:

- Chapter 1 - Introduction: A brief motivation with respect to the relevance of the proposed work as well as its objective are presented.
- Chapter 2 - Literature Review: An extensive review on published works in the fields of Finite Elements and Vortex-Induced Vibrations are presented.
- Chapter 3 - Methodology: The governing equations are derived and the different methods employed are explained.
- Chapter 4 - Validation and Results: Simulations used to validate the developed methodology as well as the different studied cases are presented.
- Chapter 5 - Conclusion: A brief summary of the work and future improvements are presented.

Chapter 2

Literature Review

This chapter includes the literature review on the physical problem being tackled by this work, as well as a review on the numerical method used to discretize the governing equations.

2.1 Vortex-Induced Vibrations

According to Kaneko *et al.* [1], flow-induced vibrations (FIV) may be classified into two major categories based on the vibration mechanism: vortex-induced vibrations and fluidelastic vibrations. Aerodynamic flutter and galloping are examples of fluidelastic instabilities. These classifications are given considering a single phase external flow, there are other definitions if a different flow field is considered, see Fig. 2.1. This work, however deals with VIV only.

Human knowledge of vortices dates back to Leonardo da Vinci's sketches from the sixteenth century. In one of them, da Vinci sketched the water flow past a blunt geometry of rectangular cross section emphasizing the symmetrical vortices in the wake, see Fig. 2.2. In spite of da Vinci's curiosity, the first scientific study of the vortex shedding phenomenon was performed by Strouhal [13] in 1878. He experimented with stretched wires which experienced vortex shedding. From his work, it was concluded that the frequency of the shedding vortices were independent of the tension and elasticity of the wires. Moreover, it was from his work that the infamous non-dimensional relationship between the free-stream velocity, shedding frequency and diameter. This non-dimensional number is now known as the Strouhal

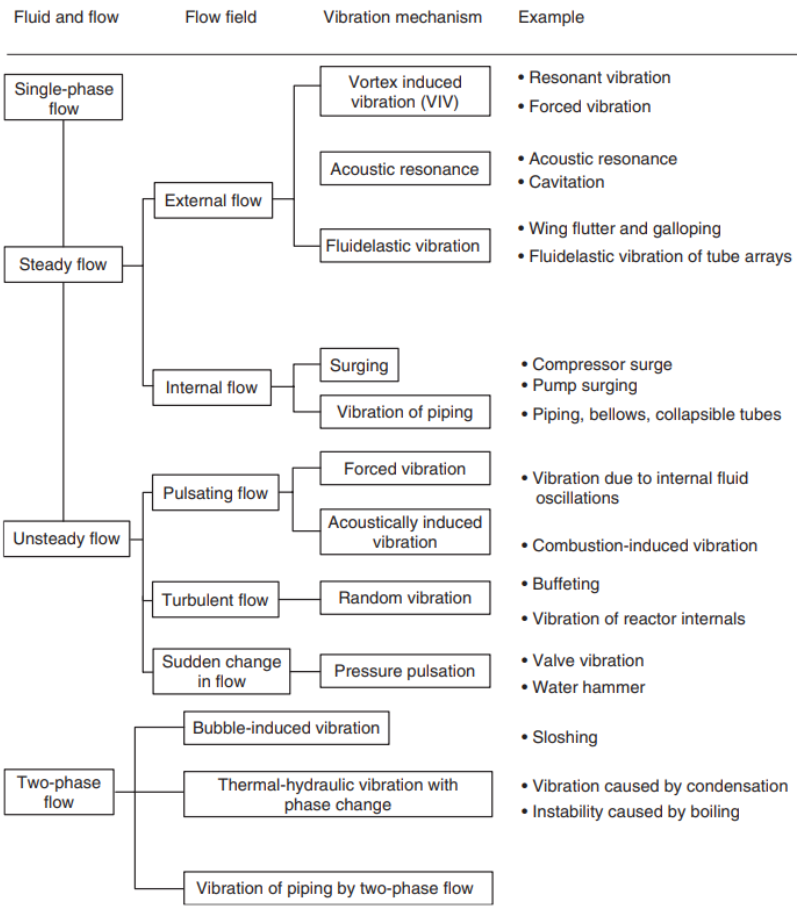

Figure 2.1: FIV classifications, adapted from Kaneko *et al.* [1].

number:

$$St = \frac{f_s D}{U}. \tag{2.1}$$

The vortex shedding process results in a repeating pattern of swirling vortices known as the von Kárman vortex street. This phenomenon was named after him due to his contribution on the mathematical understanding of this intricate fluid dynamics problem in his work from 1911 and 1912 [14]. It was von Kárman that suggested the alternating arrangement of the vortices.

In 1964, Bishop and Hassan [15] published what is now considered a classical paper on forced vibrations. They conducted an experiment by placing a circular cylinder in flowing water. This cylinder was forced to oscillate at different frequencies. From their studies, three main conclusions were made: (*i*) The forces acting on the cylinder may be modelled by a non-linear self-excited fluid oscillator. (*ii*) The fluid oscillator experiences hysteresis and frequency demultiplication. (*iii*) It

Figure 2.2: Leonardo da Vinci, movement of water, ca. 1513.

was also observed that the oscillator experiences synchronization within a certain range. Inside this range the lift and drag amplitudes will reach a maximum near a critical frequency.

In 1966, Lienhard [2] gathered the available data on the drag, lift and vortex shedding for a rigid circular cylinder. With this he plotted an envelope which described the relationship between the Strouhal and Reynolds number, see Fig. 2.3. The author emphasized that the Strouhal number is accurate within 5% over most Reynolds numbers. However, the relationship's behaviour in the transition region is poorly understood and the author suggested further studies.

In 1967, Koopmann [8] conducted an experiment to determine to what effect the forced oscillations of a circular cylinder affect the wake structures at low Reynolds number. He identified lower and upper limits of the locked-in region for different Reynolds numbers. As well as noticing that the bandwidth of synchronization grows with the amplitude of vibration imposed on the cylinder.

Feng [5] performed experiments on a wind tunnel in which he studied the vortex shedding and displacement amplitude of a circular and D-section cylinders. These

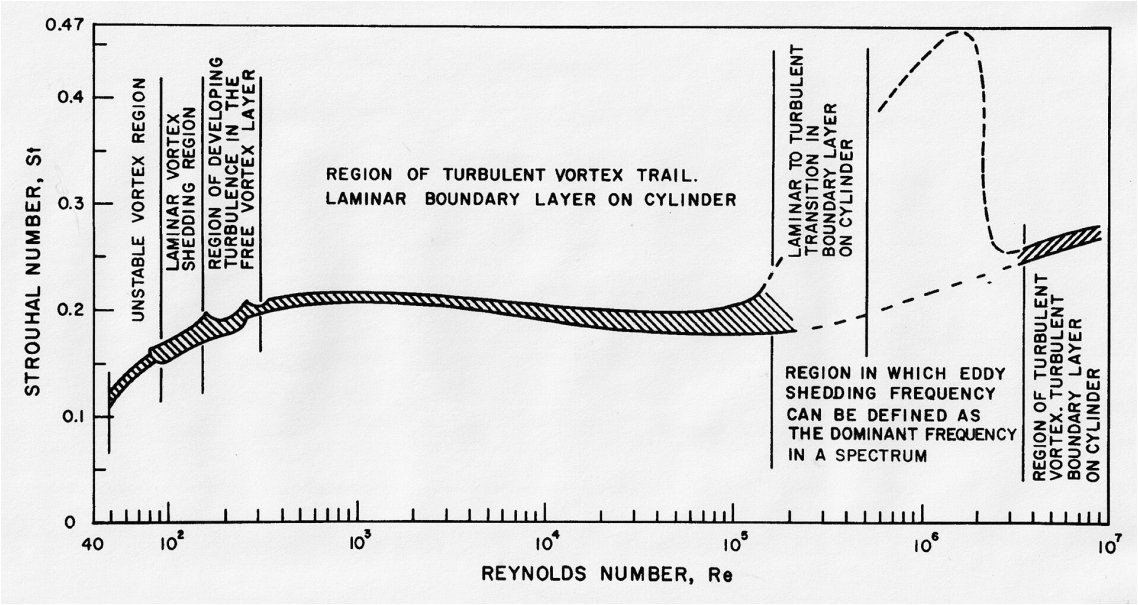

Figure 2.3: Behaviour of the Strouhal number as a function of the Reynolds number for a circular cylinder, from Lienhard [2].

phenomena were investigated for an elastically mounted cylinder. Considering the experiments of the circular cylinder only, Feng observed that there was hysteresis for low damping cases while hysteresis was not present in high damping ones. It was observed that the max amplitude and locked-in region, when the vortex shedding frequency remains the same as the oscillation frequency, became smaller as the damping ratio was increased. Feng also noticed that the max amplitude occurs at a lower dimensionless velocity as the damping was increased.

In 1974, Blevins [16] developed a two degree of freedom (DOF) phenomenological model for VIV of a circular cylinder following the idea introduced by Bishop and Hassan [15]. The Iwan-Blevins model was based on a control volume for the vortex shedding phenomenon and von Karman's idealization of the vortex street. His model for forced oscillations used a van der Pol oscillator. The model's parameters were determined experimentally through fixed and oscillating cylinder data. Blevins also pointed out that during forced harmonic oscillations, as the forcing frequency approaches the shedding frequency, the evolution of the lift coefficient also becomes harmonic. Later, in 1990 Blevins released a book entitled *Flow-Induced Vibrations*, which included his model as well as some other ones.

Williamson and Roshko [3] conducted experiments in order to better understand

the formation of vortex patterns behind an oscillating cylinder. To do so, they widened the oscillation amplitude range up to 5 cylinder diameters and presented their results in the amplitude-wavelength plane. They demonstrated the existence of multiple synchronization regions beyond the fundamental lock-in one, see Fig. 2.4. The vortex patterns near the lock-in region were also documented, which can be seen in Fig. 2.5. For the larger amplitude synchronization zones, it was observed that the resulting vortex street can grow immensely. And despite the symmetry observed in the body's movement, the patterns observed can be asymmetric.

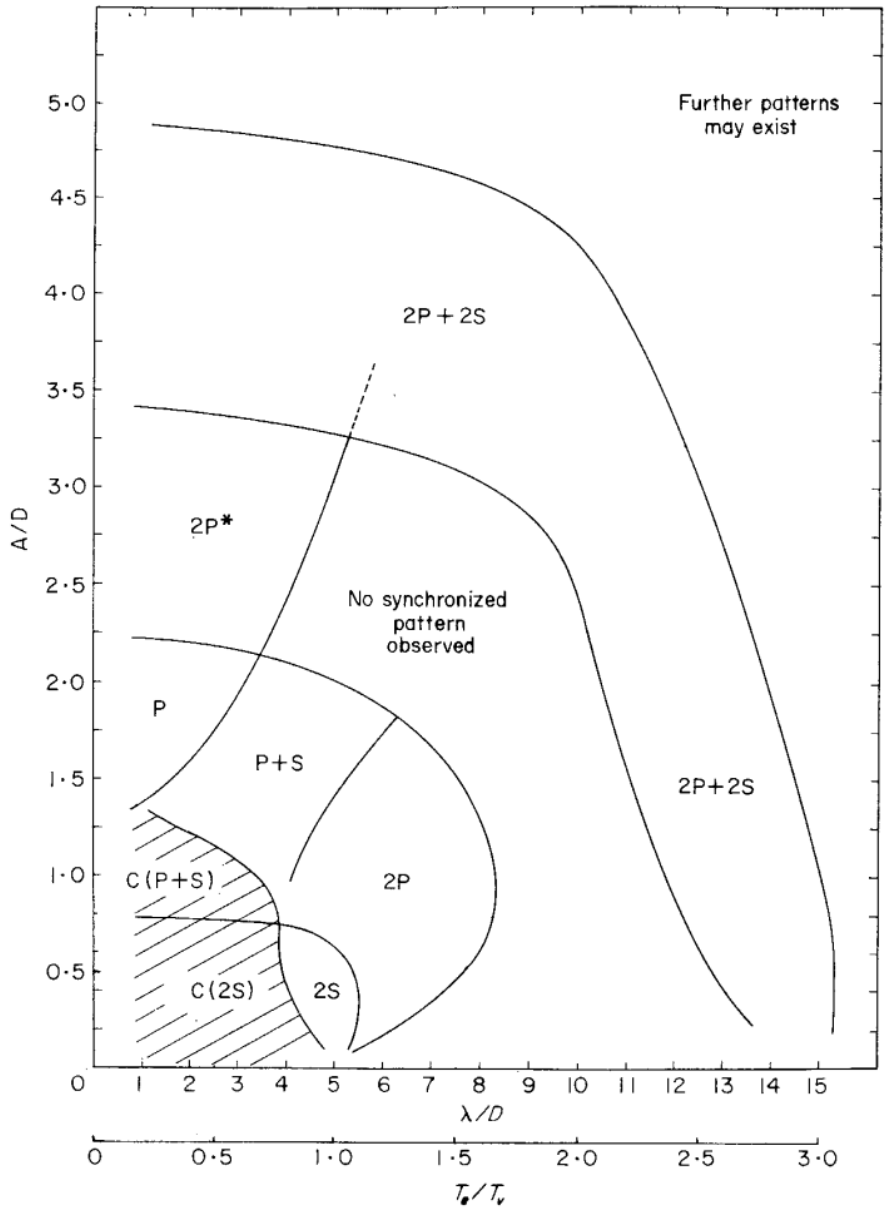

Figure 2.4: Different vortex patterns observed by Williamson and Roshko [3] throughout the entire experimental amplitude range.

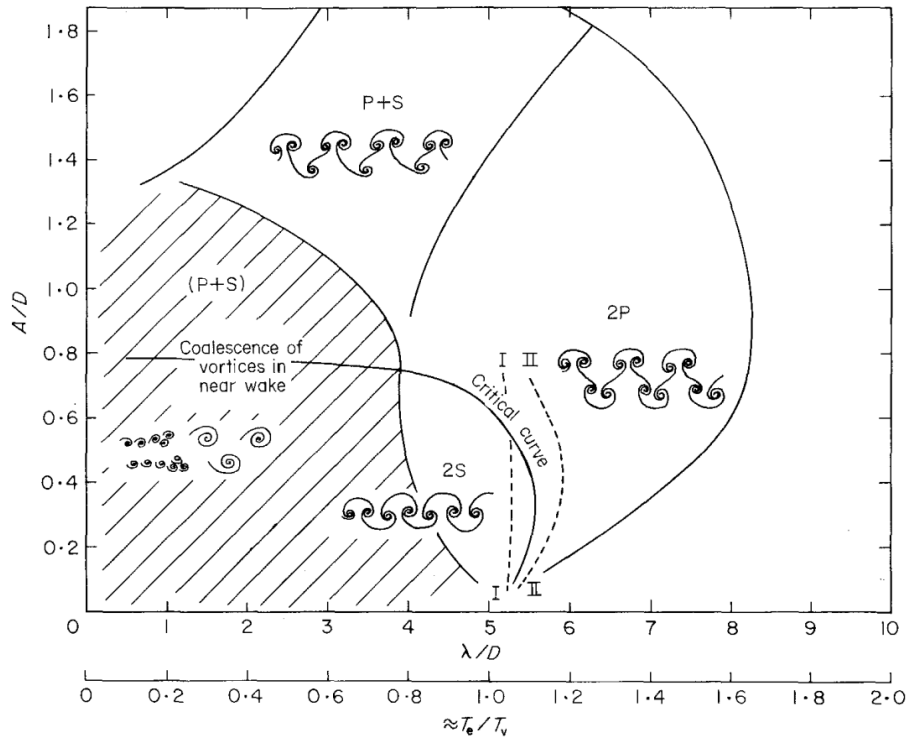

Figure 2.5: The different vortex patterns observed by Williamson and Roshko [3] near the lock-in region.

Blackburn and Karnadiakis [17] performed numerical simulations of forced and free vibrations in cross-flow of a circular cylinder. They developed a spectral element method (SEM) to solve the bidimensional Navier-Stokes equations using a three-level high-order time-split scheme for time integration. In which they employed an eight-order Legendre-Lagrangian polynomials as interpolants within each mesh element. It is also mentioned that the method is applicable to three dimensional flows. The results showed good agreement with available experimental data, emphasizing the power of numerical simulations.

In 1996, Khalak and Williamson [4] conducted an experiment to measure lift, drag and position of an extremely low mass and damping circular cylinder. This was possible due to low friction and lightweight design which achieved a lower damping ratio when compared to earlier studies. They also concluded that the fluctuating lift and drag forces are sensitive to the boundary conditions at the cylinder's end. It was also observed that the cylinder's response has two branches of resonance: lower and upper, which was previously neglected, see Fig. 2.6. They also studied the behaviour of the system when varying m^*, it was concluded that the lower m^* gives

the greater response. This behaviour was also observed in a bidimensional direct numerical simulations of Newman and Karniadakis [18].

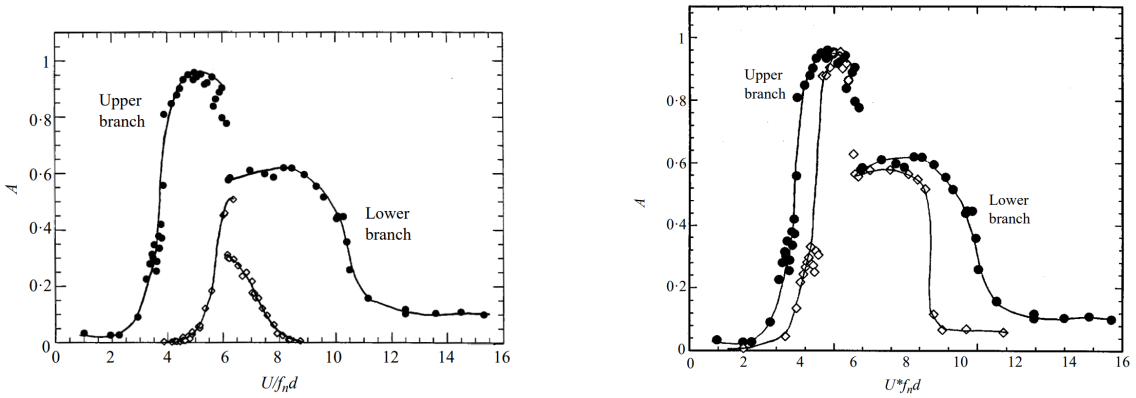

(a) (b)

Figure 2.6: (a) Comparison of Khalak and Williamson's [4] results for low mass-damping (•), and Feng's [5] (⋄) the mass-damping parameter, $m^*\zeta$, is about 30 times smaller for Khalak's experimental conditions. (b) Comparison of the observed results for $m^* = 2.4$ (•), and $m^* = 10.3$ (⋄), while the mass-damping parameter was the same.

Mittal and Kumar [19] used a stabilized space-time finite element formulation to study cross-flow and in-line oscillations of a circular cylinder at Reynolds number 325. They noticed a phenomenon called *soft lock-in*, in which the oscillation frequency does not exactly match the structural frequency, that is, a slight detuning is present. This happened when the cylinder's mass was close to the mass of the displaced fluid, and disappeared when the cylinder's mass was much larger. The authors concluded that the detuning of the vortex-shedding frequency from the structural frequency is a mechanism of the oscillator to self-limit its vibration amplitude. Singh and Mittal [20] studied the hysteresis and vortex shedding modes at $Re = 100$ while Prasanth and Mittal [9] studied VIV by fixing the Reynolds number and varying the reduced natural frequency of the system and by fixing the natural frequency and varying the Reynolds number from 60 to 200. Both of these studies used the finite element formulation introduced in Mittal and Kumar [19].

Shiels *et al.* [21] performed numerical simulations using the viscous vortex method to investigate the cross-flow oscillations of an elastically supported circular cylinder at $Re = 100$. They introduced a new variable into the analysis named

effective elasticity, k^*_{eff} while studying the response for the undamped system. The effective elasticity combines the effects of inertial and elastic forces into a single dimensionless parameter.

Nobari and Naderan [22] studied the two-dimensional flow around an oscillating circular cylinder using the FEM coupled with the ALE formulation, to account for mesh movement. The authors independently analysed forced cross-flow and in-line oscillations, varying oscillation amplitude and frequency. They observed that lock-on occurred near the Strohaul frequency for the cross-flow vibrations while the synchronization happened near twice the Strouhal frequency for in-line oscillations. The vortex patterns for different oscillation conditions was also analysed.

Plackzek *et al.* [23] performed numerical simulations of an oscillating cylinder in cross-flow at $Re = 100$. The authors used an finite volume code to solve the bidimensional Navier-Stokes equations coupled with the ALE formulation. They studied forced oscillations to identify the lock-in boundaries as well as free vibrations using the dimensionless parameter k^*_{eff}, introduced by Shiels *et al.* [21].

Williamson and Govardhan [12], Tamura [24], Wu *et al.* [25] and Huera-Huarte [26] published extensive reviews on vortex and flow-induced vibrations. In which they summarize published results as well as present the different models developed for VIV. These are excellent papers if the reader wishes to understand the physical phenomenon as well as get acquainted with the plethora of material available in this complex field of fluid-structure interactions.

From the brief review herein presented, VIV may be defined as a self-excited, yet self-limited physical phenomenon. It is also clear that there are three ways to study vortex-induced vibrations: CFD , experimentally and wake-oscillator models. While the first two methods are used to fundamentally understand the physical phenomenon, the later is very useful in predicting the dynamics of structures under VIV. The current work, however deals with CFD to study VIV.

2.2 Finite Element Method

The origin of the finite element method may be traced back to 1941, however the term "Finite Element Method" was coined by Clough in 1960 [27]. Up to this date,

the FEM was exclusively used to solve solid mechanics problems. As such, multiple references on the application of the FEM in the field of solids are well-established, see [28, 29, 30]. Nevertheless, the pioneering work which applied the FEM to field problems was published in 1965 by Zienkiewicz and Cheung [31].

When utilizing the FEM to discretize the Navier-Stokes equations, one obtains a saddle-point problem due to the velocity-pressure coupling, as well as the incompressibility condition. And depending on the type of element employed, the saddle-point problem will not have an unique solution. In order to guarantee that the discretization will yield in a well-posed problem a certain condition must be satisfied. The works from Ladyzhenskaya [32], Babuška [33] and Brezzi [34], culminated in the inf-sup or Ladyzhenskaya-Babuška-Brezzi condition, which determines whether the discretization of a saddle-point problem is stable.

Taylor and Hood [35], applied the FEM to solve the bidimensional Navier-Stokes equations using two different formulations: velocity-pressure and stream function-vorticity. Both of them were discretized using the Galerkin method. Nevertheless, the $\mathbf{v} - p$ formulation used parabolic isoparametric elements, the $\psi - \omega$ formulation used the cubic quadrilateral since the second derivatives of the shape functions are needed. They conclude their work emphasizing that the $\mathbf{v} - p$ formulation is more feasible due to the fact that pressure boundary conditions are directly specified. Furthermore, this formulation facilitates the use of the FEM in three dimensions because the $\psi - \omega$ one requires the use of plate-bending type elements that cannot be easily extended to the third dimension.

Huyakorn *et al.* [6], performed a comparison between four types of mixed interpolation finite elements used to discretize the $\mathbf{v} - p$ formulation of the Navier-Stokes equations. These four types were: six-node triangular elements, eight-node serendipity elements, nine-node Lagrangian elements and four-node quadrilateral elements. They concluded that for the most accurate results for velocity and pressure fields, the Lagrangian element must be employed while the serendipity one yields the less accurate pressure distribution. Moreover, the four-noded element will generate erroneous pressure solutions depending on the boundary conditions.

In 1980, Gresho *et al.* [36], developed a Galerkin finite element method (GFEM) to solve the incompressible Navier-Stokes and Boussinesq equations in two dimen-

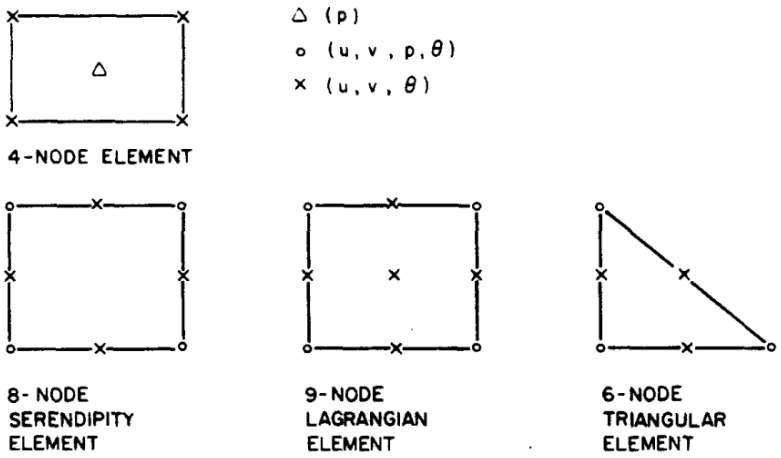

Figure 2.7: Mixed interpolation elements considered in Huyakorn *et al.* [6].

sions. The GFEM was applied the governing equations in primitive variables $(\mathbf{v}, p, T)$, yielding in a coupled system of ordinary differential equations in time. They employed a quadratic approximation for velocity and temperature while using a linear one for the pressure in order to satisfy the LBB condition. The element of choice was the nine-noded quadrilateral, which they reported performs badly for strong thermally-coupled flows. This occurs due to the approximation space used for the pressure, which sometimes fail to adequately enforce incompressibility.

The arbitrary Lagrangian-Eulerian (ALE) framework was first developed in the context of a finite difference scheme for all flow speeds, detailed in Hirt *et al.* [37]. Considering the FEM however, the ALE description for incompressible viscous flows was developed by Hughes *et al.* [38], while Donea *et al.* [39] applied the ALE to inviscid compressible flows. Both of them used the ALE formulation to properly simulate fluid-structure interactions, which yielded in satisfactory results.

In 1982, Brooks and Hughes [40] developed the Streamline Upwind/Petrov-Galerkin (SUPG) for convection dominated flows. They used an implicit pressure/explicit velocity transient algorithm that allows for the treatment of the incompressibility condition and multiple iterations within a single time step. The developed method has the robustness of an upwind method, as spurious wiggles do not appear in the solution. The method is also free of artificial diffusion, often present in upwinding schemes. In the context of finite elements, this method is also easily implemented since it does not require higher order or exotic weighting functions.

Pironneau [41] developed a second order algorithm combining the method of characteristics and the FEM to solve the convection-diffusion equation. He applied said scheme to solve linear transport-diffusion equation and also extended it to the Navier-Stokes equations. This scheme was of the upwinding type and proved itself stable even when the Reynolds number is infinite, that is, the Euler equation.

Codina [42] presented a review on the available finite element methods for the convection-diffusion-reaction equation. In which he highlights the similarities and differences between the five methods described therein. They are: SUPG, Space-time Galerkin/least-squares method (ST-GLS), Sub-grid scale method (SGS), Characteristic Galerkin (CG) and Taylor-Galerkin method (TG). Codina shows that the main difference between the presented methods lies in the different definitions of an operator applied to the test functions, which is responsible for the stabilizing properties of each method.

More recently, Anjos [43] developed a three-dimensional finite element code to solve for the hydrodynamic field near the rotating electrode in an electrochemical cell. The Galerkin method was applied in the spatial discretization of the Navier-Stokes equations, while the convective term was treated through the material derivative, which in turn, was discretized by a first-order explicit semi-Lagrangian scheme. A few years later, Anjos extended this work to simulate two-phase flows with phase change to study micro scale interlayer cooling systems, see [44]. In which he utilized the ALE description to account for moving boundaries inside the fluid domain, thus effectively capturing two-phase flows moving interfaces.

The finite element method coupled with the arbitrary Lagrangian-Eulerian framework continues to be employed in fluid-structure interaction modelling and simulation in diverse fields of study. Sun *et al.* [45] developed an advanced ALE mixed finite element method to solve cardiovascular fluid-structure interaction problems that arise from cardiovascular diseases that culminate in aneurysms attached to the vascular wall. Darbhamulla and Jaiman [46] proposed an ALE-FE framework for the prediction of cavitating turbulent flows interacting with flexible structures. While Palmer *et al.* [47] used the Petrov-Galerkin FEM coupled with the ALE scheme to determine the performance of Oscillating Water Column (OWC) under second-order Stokes waves. Lastly, Sun *et al.* [48] developed an immersed multi-

material arbitrary Lagrangian Eulerian finite element method to effectively capture fluid-structure interactions considering multi-phase flows.

Chapter 3

Methodology

In this chapter, the governing equations for an incompressible Newtonian fluid are derived, obtaining the Navier-Stokes equations. These equations are then presented in a non-dimensional form, which allows for a better understanding of the terms in the equations. After that, the arbitrary Lagrangian-Eulerian framework is formally introduced and the governing equations are written in this formulation. Every differential equation is subjected to boundary and/or initial conditions, hence a brief description of these conditions are also shown. Later, the spatial and temporal discretization methods are introduced in order to obtain the discrete system of equations. Then the chapter ends with a few comments about the computational aspects and a full algorithm for the solution of the Navier-Stokes equations written in an ALE reference frame.

3.1 Governing Equations

This chapter will introduce the differential equations that govern fluid flow. The equations are written in the arbitrary Lagrangian-Eulerian reference frame. Since the fluid is considered to be a *continuum*, three independent dynamical laws may be used to describe fluid flow:

- Conservation of mass
- Conservation of momentum
- Conservation of energy

In this work, however, the third law will be disregarded as it will not be used to study the phenomena of interest.

3.1.1 Conservation of Mass

According to Panton [49], this conservation law states that the time rate of change of the mass of a of a material region is zero. In other words, it means that the rate in which mass enters a control volume is the same as the rate of mass leaving plus the accumulation of mass within this volume.

The mass of the material region is computed by integrating the density over the volume. In mathematical terms:

$$\frac{\mathrm{d}}{\mathrm{d}t}\int_V \rho \,\mathrm{d}V = 0. \tag{3.1}$$

Using the Reynolds transport theorem, Eq. (3.1) is rewritten as:

$$\int_V \frac{\partial \rho}{\partial t}\,\mathrm{d}V + \int_S \rho \mathbf{v}\cdot\mathbf{n}\,\mathrm{d}S = 0, \tag{3.2}$$

by applying the Gauss theorem to the surface integral in Eq. (3.2), the whole equation is written in terms of a volume integral:

$$\int_V \frac{\partial \rho}{\partial t} + \nabla\cdot(\rho\mathbf{v})\,\mathrm{d}V = 0. \tag{3.3}$$

Since Eq. (3.3) is valid for all volumes lying entirely in the fluid domain, it means that the integrand must be equal to zero, hence:

$$\frac{\partial \rho}{\partial t} + \nabla\cdot(\rho\mathbf{v})\,\mathrm{d}V = 0, \tag{3.4}$$

which is known as the continuity equation. Since the present work deals with incompressible fluids, $\rho =$ constant, Eq. (3.4) is simplified to:

$$\nabla\cdot\mathbf{v} = 0. \tag{3.5}$$

3.1.2 Conservation of Momentum

This conservation law states that for a given fluid with density, ρ which flows through a control volume V, its momentum accumulation rate is equal to the net flux of momentum out of the control volume plus the resultant of surface and body

forces. This conservation law is analogous to Newton's second law for a point mass. Mathematically it can be stated as:

$$\frac{\mathrm{d}}{\mathrm{d}t}\int_V \rho\mathbf{v}\,\mathrm{d}V = \mathbf{F}_S + \mathbf{F}_B. \tag{3.6}$$

Using the Reynolds transport theorem to rewrite the left-hand side of Eq. (3.6):

$$\frac{\mathrm{d}}{\mathrm{d}t}\int_V \rho\mathbf{v}\,\mathrm{d}V = \int_V \frac{\partial(\rho\mathbf{v})}{\partial t}\,\mathrm{d}V + \int_S \rho\mathbf{v}\mathbf{v}\cdot\mathbf{n}\,\mathrm{d}S, \tag{3.7}$$

while the resultant surface and body forces may be expressed as:

$$\mathbf{F}_S = \int_S \boldsymbol{\sigma}\cdot\mathbf{n}\,\mathrm{d}S, \tag{3.8}$$

$$\mathbf{F}_B = \int_V \rho\mathbf{g}\,\mathrm{d}V, \tag{3.9}$$

where $\boldsymbol{\sigma}$ represents the stress tensor and $\mathbf{g}$ the gravitational acceleration. Therefore, Eq. (3.6) is written as:

$$\int_V \frac{\partial(\rho\mathbf{v})}{\partial t}\,\mathrm{d}V + \int_S \rho\mathbf{v}\mathbf{v}\cdot\mathbf{n}\,\mathrm{d}S = \int_S \boldsymbol{\sigma}\cdot\mathbf{n}\,\mathrm{d}S + \int_V \rho\mathbf{g}\,\mathrm{d}V. \tag{3.10}$$

Using Gauss' theorem in Eq. (3.10) to transform surface integrals into volume integrals yields:

$$\int_V \frac{\partial(\rho\mathbf{v})}{\partial t}\,\mathrm{d}V + \int_V \nabla\cdot(\rho\mathbf{v}\mathbf{v})\,\mathrm{d}V = \int_V \nabla\cdot\boldsymbol{\sigma}\,\mathrm{d}V + \int_V \rho\mathbf{g}\,\mathrm{d}V. \tag{3.11}$$

Similarly to the conservation of mass, Eq. (3.11) must be valid for any control volume, hence:

$$\frac{\partial(\rho\mathbf{v})}{\partial t} + \nabla\cdot(\rho\mathbf{v}\mathbf{v}) = \nabla\cdot\boldsymbol{\sigma} + \rho\mathbf{g}. \tag{3.12}$$

Expanding the left-hand side of Eq. (3.12) using the derivative product rule and the following identity, $\nabla\cdot(U\mathbf{A}) = \mathbf{A}\cdot(\nabla U) + U(\nabla\cdot\mathbf{A})$, it becomes:

$$\frac{\partial(\rho\mathbf{v})}{\partial t} + \nabla\cdot(\rho\mathbf{v}\mathbf{v}) = \mathbf{v}\frac{\partial\rho}{\partial t} + \rho\frac{\partial\mathbf{v}}{\partial t} + \mathbf{v}\cdot(\nabla\rho\mathbf{v}) + \rho\mathbf{v}(\nabla\cdot\mathbf{v}). \tag{3.13}$$

As this work deals with incompressible fluids:

$$\frac{\partial\rho}{\partial t} = 0,$$

$$\nabla\cdot\mathbf{v} = 0,$$

therefore Eq. (3.12) simplifies to:

$$\rho\left(\frac{\partial\mathbf{v}}{\partial t} + \mathbf{v}\cdot\nabla\mathbf{v}\right) = \nabla\cdot\boldsymbol{\sigma} + \mathbf{g}. \tag{3.14}$$

Based on the assumptions made to derive the previous equations, the stress tensor is defined as:

$$\boldsymbol{\sigma} = -p\mathbf{I} + \boldsymbol{\tau}, \tag{3.15}$$

where p represents the mechanical pressure, $\mathbf{I}$ is a 3×3 identity matrix and $\boldsymbol{\tau}$ is the viscous stress tensor. Equation (3.15) in matrix notation is:

$$\begin{bmatrix} \sigma_{xx} & \sigma_{xy} & \sigma_{xz} \\ \sigma_{yx} & \sigma_{yy} & \sigma_{yz} \\ \sigma_{zx} & \sigma_{zy} & \sigma_{zz} \end{bmatrix} = \begin{bmatrix} -p_x & 0 & 0 \\ 0 & -p_y & 0 \\ 0 & 0 & -p_z \end{bmatrix} + \begin{bmatrix} \tau_{xx} & \tau_{xy} & \tau_{xz} \\ \tau_{yx} & \tau_{yy} & \tau_{yz} \\ \tau_{zx} & \tau_{zy} & \tau_{zz} \end{bmatrix}. \tag{3.16}$$

Substitution of Eq. (3.15) into (3.14), yields:

$$\rho\left(\frac{\partial \mathbf{v}}{\partial t} + \mathbf{v}\cdot\nabla\mathbf{v}\right) = -\nabla p + \nabla\cdot\boldsymbol{\tau} + \mathbf{g}. \tag{3.17}$$

From Eq. (3.17), it becomes clear that a definition for the viscous stress tensor is still needed, hence the assumption of Newtonian fluid is adopted.

3.1.3 Newtonian Fluids

By definition, a fluid continuously deforms under shear stress. Its general behaviour may be described by the relationship between the applied shear stress and shear rate. For Newtonian fluids this relation is linear and is mathematically expressed by, Panton [49]:

$$\boldsymbol{\tau} = -\frac{2}{3}\mu\delta\left(\nabla\cdot\mathbf{v}\right) + 2\mu\mathbf{E}, \tag{3.18}$$

where μ is the dynamic viscosity, δ is the Kronecker delta and $\mathbf{E}$ is the strain rate tensor, which is defined as:

$$\mathbf{E} = \frac{1}{2}\left[\nabla\mathbf{v} + (\nabla\mathbf{v})^T\right]. \tag{3.19}$$

However, due to the continuity equation, Eq. (3.5), the viscous stress tensor, Eq. (3.18) simplifies to:

$$\boldsymbol{\tau} = \mu\left[\nabla\mathbf{v} + (\nabla\mathbf{v})^T\right]. \tag{3.20}$$

3.1.4 Navier-Stokes Equations

The continuity equation coupled with the conservation of momentum equation in which the viscous stress tensor, $\boldsymbol{\tau}$ is substituted by Eq. (3.20), may be referred

as the Navier-Stokes equations. The energy equation could also be coupled with the other two, however its inclusion is beyond the scope of this work.

For an incompressible, viscous flow these equations are:

$$\nabla \cdot \mathbf{v} = 0, \tag{3.21}$$

$$\frac{\partial \mathbf{v}}{\partial t} + \mathbf{v} \cdot \nabla \mathbf{v} = -\frac{1}{\rho}\nabla p + \nabla \cdot \left[\nu(\nabla \mathbf{v} + \nabla \mathbf{v}^T)\right] + \mathbf{g}, \tag{3.22}$$

where ν is the kinematic viscosity and it is defined as $\nu = \mu/\rho$. Taking into account the incompressibility condition and rewriting Eq. (3.22) in terms of the material derivative yields:

$$\frac{\mathrm{D}\mathbf{v}}{\mathrm{D}t} = -\frac{1}{\rho}\nabla p + \nu \nabla^2 \mathbf{v} + \mathbf{g}. \tag{3.23}$$

Equations (3.22) and (3.23) represent the conservation of momentum in the Eulerian and Lagrangian descriptions, respectively. The material derivative notation is preferred since it is more convenient to understand the semi-Lagrangian method, which will be explained later.

3.1.5 Non-dimensional Navier-Stokes Equations

The procedure derived in this section in unnecessary if the objective is only to solve the Navier-Stokes equations. However, such a procedure allows for a better understanding of the terms in the equations. Thus, this methodology starts by defining non dimensional variables:

$$\mathbf{x}^* = \frac{\mathbf{x}}{L} \qquad \mathbf{v}^* = \frac{\mathbf{v}}{U} \qquad t^* = \frac{tU}{L} \qquad p^* = \frac{p}{\rho U^2}$$

$$\mathbf{g}^* = \frac{\mathbf{g}}{\mathrm{g}_\infty} \qquad \frac{\partial}{\partial t^*} = \frac{L}{U}\frac{\partial}{\partial t} \qquad \nabla^* = \frac{\nabla}{L} \qquad \nabla^{2^*} = \frac{\nabla^2}{L^2}$$

where the superscript * identifies that variable as non dimensional. Substitution of these newly defined variables in Eqs. (3.21) and (3.22) yields:

$$\frac{U}{L}\nabla^* \cdot \mathbf{v}^* = 0, \tag{3.24}$$

$$\frac{U^2}{L}\frac{\partial \mathbf{v}^*}{\partial t^*} + \frac{U^2}{L}\mathbf{v}^* \cdot \nabla^* \mathbf{v}^* = -\frac{\rho U^2}{\rho L}\nabla^* p^* + \frac{\nu U}{L^2}\nabla^* \cdot \left[\nabla^* \mathbf{v}^* + (\nabla^* \mathbf{v}^*)^T\right] + \mathrm{g}_\infty \mathbf{g}^*. \tag{3.25}$$

Multiplying the continuity and momentum equations above by L/U and L/U^2, respectively:

$$\nabla^* \cdot \mathbf{v}^* = 0, \tag{3.26}$$

$$\frac{\partial \mathbf{v}^*}{\partial t^*} + \mathbf{v}^* \cdot \nabla^* \mathbf{v}^* = -\nabla^* p^* + \frac{\nu}{UL} \nabla^* \cdot \left[\nabla^* \mathbf{v}^* + (\nabla^* \mathbf{v}^*)^T \right] + \frac{\mathrm{g}_\infty L}{U^2} \mathbf{g}^*. \tag{3.27}$$

From the equations above, two non dimensional numbers may be identified, the Reynolds and Froude numbers, they are:

$$Re = \frac{UL}{\nu} \qquad\qquad Fr = \frac{U}{\sqrt{\mathrm{g}L}}$$

where the Re number represents the ratio between inertial and viscous forces, and the Fr number, the ratio between inertial and gravitational forces. For example, if $Re < 1$ it means that the viscous forces are dominant whereas if $Re >> 1$, the inertial forces are dominant. This analysis allows for the characterization of the flow in question, that is, laminar flows occur at low Reynolds while turbulent flow occurs at high Reynolds. The Froude number however is less important than the Reynolds one, considering the objective of this study. It becomes relevant in flows where a free-surface is present, for example. This number is used to characterize flows in which the effects of gravity cannot be neglected.

Therefore by using the non dimensional numbers, dropping the superscript and accounting for the incompressibility condition, Eqs. (3.22) and (3.23) may be rewritten in non-dimensional form:

$$\nabla \cdot \mathbf{v} = 0, \tag{3.28}$$

$$\frac{\partial \mathbf{v}}{\partial t} + \mathbf{v} \cdot \nabla \mathbf{v} = -\nabla p + \frac{1}{Re} \nabla^2 \mathbf{v} + \frac{1}{Fr^2} \mathbf{g}. \tag{3.29}$$

3.1.6 Arbitrary Lagrangian-Eulerian

There are two main ways to specify the dynamics of a fluid, one of them follows the fluid particle and the other observes the flow through a fixed point in the domain. They are known as Lagrangian and Eulerian descriptions.

In the Lagrangian framework any flow variable may be expressed as $\varphi(\mathbf{x_0}, t)$, where $\mathbf{x_0}$ is the position of the particle's centre of mass at some initial instant, t_0, Batchelor [50]. Hence, the material derivative is used to describe the fluid dynamics. However, from a computational standpoint this description is not feasible since its

unable to follow large distortions of the computational domain without constant remeshing operations, Donea [51]. This is necessary because the mesh nodes are displaced at each time step by the calculated fluid's velocity. Figure 3.1 represents a one-dimensional example.

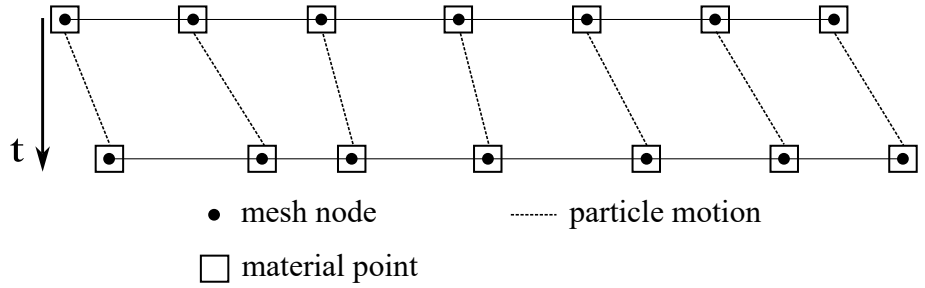

Figure 3.1: Lagrangian framework schematics: mesh nodes move with the calculated flow field velocity.

While in the Eulerian description flow quantities are defined as functions of time, t and position in space, $\mathbf{x} = (x, y, z)$. Computationally speaking it can handle large distortions since the mesh no longer moves with the fluid velocity. Nevertheless, it lacks when it comes to precise definition of interfaces. Figure 3.2 represents the Eulerian framework in one-dimension.

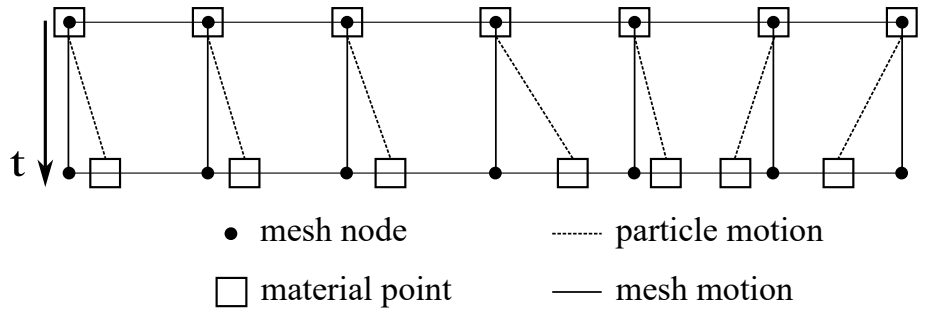

Figure 3.2: Eulerian description schematics: mesh nodes are fixed in space throughout time.

That said, the arbitrary Lagrangian-Eulerian (ALE) framework tries to combine the best features of the Lagrangian and Eulerian descriptions. In the ALE framework, mesh nodes may move in a Lagrangian fashion, be fixed in a Eulerian manner or moved in some arbitrary way with velocity $\hat{\mathbf{v}}$. There are three possible scenarios when considering the mesh velocity. If $\hat{\mathbf{v}} = 0$ the Eulerian description is recovered, if $\hat{\mathbf{v}} = \mathbf{v}$ the mesh moves with the same velocity as the fluid particle which recovers

the Lagrangian viewpoint. Meanwhile, if $\hat{\mathbf{v}} \neq \mathbf{v} \neq 0$ the mesh moves with an arbitrary velocity and the ALE framework is achieved. Figure 3.3 illustrates the ALE description in one-dimension.

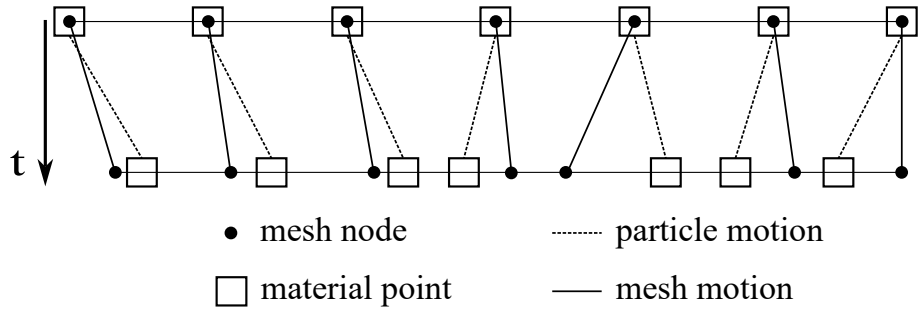

Figure 3.3: ALE framework schematics: a generalized description in which the mesh nodes can move with an arbitrary velocity or stay fixed.

The non-dimensional incompressible Navier-Stokes equations written in an ALE reference frame are:

$$\frac{\partial \mathbf{v}}{\partial t} + \hat{\mathbf{c}} \cdot \nabla \mathbf{v} = -\nabla p + \frac{1}{Re} \nabla^2 \mathbf{v} + \mathbf{g}, \tag{3.30}$$

in which a convective velocity, $\hat{\mathbf{c}}$ is defined as $\hat{\mathbf{c}} = \mathbf{v} - \hat{\mathbf{v}}$.

3.1.7 Boundary and Initial Conditions

In order to solve differential equations boundary and initial conditions are of the utmost relevance, since they are used to obtain unique solutions for these equations. With respect to the numerical modelling of the Navier-Stokes equations, the following boundary conditions are used:

- No-slip condition: All velocity components are equal to zero, therefore the fluid is at rest. This condition is usually applied to walls and stationary objects in the flow.

- Free-slip condition: Normal velocity component with respect to the boundary is equal to zero, however the tangential component is unrestricted.

- Kinematic coupling condition: This condition is applied to a moving boundary within the fluid domain. The moving boundary velocity is used as the boundary condition for the fluid problem. That is, $\mathbf{v} = \dot{\mathbf{x}}$.

- Inflow condition: Used at the boundary which denotes the entrance of fluid. For this condition, $\mathbf{v} = \mathbf{v}_{\text{inlet}}$.

- Outflow condition: Defined as $p = 0$, which means that the fluid flow is exiting through that boundary. It represents a situation where flow details are unknown prior to the solution.

3.2 Finite Element Method

In this chapter the weak form of the equations solved by the computational code will be presented.

3.2.1 Variational Form

Since this work deals with incompressible fluids the equations that govern the fluid problem are the momentum and continuity equations:

$$\frac{\partial \mathbf{v}}{\partial t} + \hat{\mathbf{c}} \cdot \nabla \mathbf{v} = -\nabla p + \frac{1}{Re} \nabla^2 \mathbf{v}, \tag{3.31}$$

$$\nabla \cdot \mathbf{v} = 0, \tag{3.32}$$

which are valid in a arbitrary domain $\Omega \subset \mathbb{R}^m$. Subjected to the following boundary conditions:

$$\mathbf{v} = \mathbf{v}_\Gamma \text{ and } \nabla p \cdot \mathbf{n} = 0 \text{ in } \Gamma_1, \tag{3.33}$$

$$p = p_\Gamma \text{ and } (\mathbf{n} \cdot \nabla)\mathbf{v} \cdot \mathbf{n} = 0 \text{ in } \Gamma_2. \tag{3.34}$$

Firstly, a Hilbert space must be defined as:

$$L^2(\Omega) = \left\{ v : \Omega \to \mathbb{R} \;\middle|\; \int_\Omega v^2 \, \mathrm{d}\Omega < \infty \right\}, \tag{3.35}$$

where $L^2(\Omega)$ is an infinite dimensional space characterized by the Lebesgue integral, which is used to define the norm and inner product. Next, the Sobolev space that guarantees enough regularity for all terms in the weak formulation to be well-defined is given by:

$$H^1(\Omega) = \left\{ v \in L^2(\Omega) \;\middle|\; \frac{\partial v}{\partial x_i} \in L^2(\Omega),\ i = 1, 2, \ldots \right\}. \tag{3.36}$$

Now, the velocity subspace is defined as:

$$\mathbb{V} = H^1(\Omega)^m = \left\{ \mathbf{v} = (v_1, \ldots, v_m) \;\middle|\; v_i \in H^1(\Omega), \forall\, i = 1, \ldots, m \right\}, \tag{3.37}$$

which is essential to ensure the test functions satisfy the boundary conditions and the divergence free condition, since this work deals with incompressible flows. Note that $\mathbb{V} = H^1(\Omega)^m$ is the Cartesian product of m spaces $H^1(\Omega)$ where:

$$\mathbb{V}_\Gamma = \{ \mathbf{v} \in \mathbb{V} \mid \mathbf{v} = \mathbf{v}_\Gamma \text{ in } \Gamma_1 \}, \tag{3.38}$$

$$\mathbb{P}_\Gamma = \left\{ q \in L^2(\Omega) \;\middle|\; q = p_\Gamma \text{ in } \Gamma_2 \right\}. \tag{3.39}$$

The variational formulation consists in finding the solutions $\mathbf{v}(\mathbf{x}, t) \in \mathbb{V}_\Gamma$ and $p(\mathbf{x}, t) \in \mathbb{P}_\Gamma$.

In order to obtain the weak form of equations (3.31) and (3.32), they need to be multiplied by test functions, $\mathbf{w}$ and q, belonging to suitable spaces and integrated on Ω.

$$\int_\Omega \left(\frac{\partial \mathbf{v}}{\partial t} + \hat{\mathbf{c}} \cdot \nabla \mathbf{v} \right) \cdot \mathbf{w} \, \mathrm{d}\Omega + \int_\Omega \nabla p \cdot \mathbf{w} \, \mathrm{d}\Omega - \int_\Omega \frac{1}{Re} \nabla^2 \mathbf{v} \cdot \mathbf{w} \, \mathrm{d}\Omega = 0. \tag{3.40}$$

So as to rewrite some of terms present on Eq. (3.40) the following Green formulae are necessary, Quarteroni [52]:

$$\int_\Omega \varphi \nabla \cdot \mathbf{b} \, \mathrm{d}\Omega = -\int_\Omega \mathbf{b} \cdot \nabla \varphi \, \mathrm{d}\Omega + \int_\Gamma \varphi \mathbf{b} \cdot \mathbf{n} \, \mathrm{d}\Gamma, \tag{3.41}$$

$$-\int_\Omega \nabla^2 u v \, \mathrm{d}\Omega = \int_\Omega \nabla u \cdot \nabla v \, \mathrm{d}\Omega - \int_\Gamma (\nabla u \cdot \mathbf{n}) v \mathrm{d}\Gamma. \tag{3.42}$$

Since an ALE formulation will be used, the first term on Eq. (3.40) is treated as a material derivative:

$$\int_\Omega \left(\frac{\partial \mathbf{v}}{\partial t} + \hat{\mathbf{c}} \cdot \nabla \mathbf{v} \right) \cdot \mathbf{w} \, \mathrm{d}\Omega = \int_\Omega \frac{\mathrm{D}\mathbf{v}}{\mathrm{D}t} \cdot \mathbf{w} \, \mathrm{d}\Omega. \tag{3.43}$$

Using Green's formula for the divergence, Eq. (3.41), the second term of Eq. (3.40):

$$\int_\Omega \nabla p \cdot \mathbf{w} \, \mathrm{d}\Omega = \int_\Gamma p(\mathbf{w} \cdot \mathbf{n}) \, \mathrm{d}\Gamma - \int_\Omega p \nabla \cdot \mathbf{w} \, \mathrm{d}\Omega. \tag{3.44}$$

For the last term in Eq. (3.40), Green's formula for the laplacian is used, Eq. (3.42):

$$-\int_\Omega \frac{1}{Re} \nabla^2 \mathbf{v} \cdot \mathbf{w} \, \mathrm{d}\Omega = -\frac{1}{Re} \int_\Gamma (\nabla \mathbf{v} \cdot \mathbf{n}) \cdot \mathbf{w} \, \mathrm{d}\Gamma + \frac{1}{Re} \int_\Omega \nabla \mathbf{v} : \nabla \mathbf{w} \, \mathrm{d}\Omega. \tag{3.45}$$

The space in which the test function $\mathbf{w}$ belongs to is chosen so that $\mathbf{w} = 0$, on the boundaries where Dirichlet conditions are prescribed for $\mathbf{v}$, that is

$$\mathbb{W} = \{\mathbf{w} \in \mathrm{H}^1(\Omega) \mid \mathbf{w}_\Gamma = 0 \text{ in } \Gamma_1\}. \tag{3.46}$$

Therefore, the final variational form for the momentum equation is

$$\int_\Omega \frac{\mathrm{D}\mathbf{v}}{\mathrm{D}t} \cdot \mathbf{w} \, \mathrm{d}\Omega - \int_\Omega p \nabla \cdot \mathbf{w} \, \mathrm{d}\Omega + \frac{1}{Re} \int_\Omega \nabla \mathbf{v} : \nabla \mathbf{w} \, \mathrm{d}\Omega = 0. \tag{3.47}$$

The weak form of the continuity equation is straightforward:

$$\int_\Omega (\nabla \cdot \mathbf{v}) q \, \mathrm{d}\Omega = 0. \tag{3.48}$$

3.2.2 Spatial Discretization

In this section, the Galerkin method will be formally introduced so as to spatially discretize Eqs. (3.47) and (3.48). The Galerkin method is characterized by utilizing the interpolating functions as the weighting functions. In order to discretize the domain, the main variables need to be approximated:

$$\mathbf{v}(\mathbf{x}, t) \approx \sum_{i=1}^{n} N_i(\mathbf{x}) \mathbf{v}_i(t), \tag{3.49}$$

$$\mathbf{w}(\mathbf{x}, t) \approx \sum_{j=1}^{n} N_j(\mathbf{x}) \mathbf{w}_j(t), \tag{3.50}$$

$$p(\mathbf{x}, t) \approx \sum_{k=1}^{m} L_k(\mathbf{x}) p_k(t), \tag{3.51}$$

$$q(\mathbf{x}, t) \approx \sum_{r=1}^{m} L_r(\mathbf{x}) q_r(t). \tag{3.52}$$

In the approximations above, N_i and L_k are the interpolating or shape functions for velocity components u, v and pressure, respectively. These functions are conveniently defined so that its value at nodes i is equal to 1 and 0 at nodes j, that is:

$$N_i(\mathbf{x}) = \begin{cases} 1 \text{ if } \mathbf{x} = \mathbf{x}_i, \\ 0 \text{ if } \mathbf{x} = \mathbf{x}_j. \end{cases} \tag{3.53}$$

Since the Galerkin method is adopted, $N_i = N_j$ and n equals the number of velocity nodes while m, the number of pressure nodes. Its essential to keep in mind that $\mathbf{v}_i$ and $\mathbf{w}_j$ are bidimensional vectors:

$$\mathbf{v} = (u, v), \tag{3.54}$$

$$\mathbf{w} = (w_x, w_y). \tag{3.55}$$

Making the suitable substitutions on Eq. (3.47), yields:

$$\begin{aligned}\int_\Omega \frac{\mathrm{D}}{\mathrm{D}t}\Big(\sum_i N_i \mathbf{v}_i\Big)\cdot\Big(\sum_j N_j \mathbf{w}_j\Big)\,\mathrm{d}\Omega - \int_\Omega \Big(\sum_k L_k p_k\Big)\nabla\cdot\Big(\sum_j N_j \mathbf{w}_j\Big)\,\mathrm{d}\Omega + \\ \frac{1}{Re}\int_\Omega \nabla\Big(\sum_i N_i \mathbf{v}_i\Big) : \nabla\Big(\sum_j N_j \mathbf{w}_j\Big)\,\mathrm{d}\Omega = 0.\end{aligned} \tag{3.56}$$

Rearranging Eq. (3.56) and dividing both sides by $\mathbf{w}_j$:

$$\begin{aligned}\sum_j\sum_i \frac{\mathrm{D}\mathbf{v}_i}{\mathrm{D}t}\int_\Omega N_i N_j\,\mathrm{d}\Omega - \sum_k\sum_j p_k \int_\Omega L_k \nabla\cdot N_j\,\mathrm{d}\Omega + \\ \frac{1}{Re}\sum_j\sum_i \mathbf{v}_i \int_\Omega \nabla N_i : \nabla N_j\,\mathrm{d}\Omega = 0,\end{aligned} \tag{3.57}$$

the term $\nabla \cdot N_j$ can also be expressed as $\nabla^T N_j$. Equation (3.57) will be rewritten in the element domain, Ω^e instead of the whole domain, Ω:

$$\begin{aligned}\sum_e\sum_j\sum_i \frac{\mathrm{D}\mathbf{v}_i}{\mathrm{D}t}\int_{\Omega^e} N_i N_j\,\mathrm{d}\Omega^e - \sum_e\sum_k\sum_j p_k \int_{\Omega^e} L_k \nabla\cdot N_j\,\mathrm{d}\Omega^e + \\ \frac{1}{Re}\sum_e\sum_j\sum_i \mathbf{v}_i \int_{\Omega^e} \nabla N_i : \nabla N_j\,\mathrm{d}\Omega^e = 0.\end{aligned} \tag{3.58}$$

Considering now the weak form of the continuity equation, with substitution of $\mathbf{v}$ and q by their respective approximations:

$$\int_\Omega \Big(\nabla\cdot\sum_i N_i \mathbf{v}_i\Big)\sum_r L_r q_r\,\mathrm{d}\Omega = 0. \tag{3.59}$$

Rearrangement of Eq. (3.59) and moving onto the element domain results in:

$$\sum_e\sum_r\sum_i \mathbf{v}_i \int_{\Omega^e} (\nabla\cdot N_i) L_r\,\mathrm{d}\Omega^e = 0 \tag{3.60}$$

The integrals in Eq. (3.58) result in element matrices which are defined as:

$$\mathbf{m}^e = \int_{\Omega^e} N_i N_j\,\mathrm{d}\Omega^e, \tag{3.61}$$

$$\mathbf{g}^e = \int_{\Omega^e} L_k \nabla\cdot N_j\,\mathrm{d}\Omega^e, \tag{3.62}$$

$$\mathbf{d}^e = \int_{\Omega^e} (\nabla\cdot N_i) L_r\,\mathrm{d}\Omega^e, \tag{3.63}$$

$$\mathbf{k}^e = \int_{\Omega^e} \nabla N_i : \nabla N_j\,\mathrm{d}\Omega^e. \tag{3.64}$$

Equations (3.58) and (3.60) may be written in matrix notation:

$$\sum_e \mathbf{m}^e \frac{\mathrm{D}\mathbf{v}_i}{\mathrm{D}t} - \sum_e \mathbf{g}^e p_k + \frac{1}{Re} \sum_e \mathbf{k}^e \mathbf{v}_i = 0, \tag{3.65}$$

$$\sum_e \mathbf{d}^e \mathbf{v}_i = 0. \tag{3.66}$$

In essence, Eqs. (3.65) and (3.66) represent the system of equations that needs to be solved in order to find $\mathbf{v}$ and p. However, they are written in the element domain, Ω^e while we are looking for a solution in the global domain, Ω. Thus an assembly operation needs to be performed so that the system can be expressed in the domain of interest.

$$\mathbf{M} = \mathcal{A}(\mathbf{m}^e), \tag{3.67}$$

$$\mathbf{G} = \mathcal{A}(\mathbf{g}^e), \tag{3.68}$$

$$\mathbf{D} = \mathcal{A}(\mathbf{d}^e), \tag{3.69}$$

$$\mathbf{K} = \mathcal{A}(\mathbf{k}^e), \tag{3.70}$$

where $\mathcal{A}$ is the assembly operator. Hence, Eqs. (3.65) and (3.66) are rewritten in terms of the global matrices:

$$\mathbf{M}\frac{\mathrm{D}\mathbf{v}_i}{\mathrm{D}t} - \mathbf{G}p_k + \frac{1}{Re}\mathbf{K}\mathbf{v}_i = 0, \tag{3.71}$$

$$\mathbf{D}\mathbf{v}_i = 0. \tag{3.72}$$

It is important to state that there is a relationship between the divergent and gradient matrices used:

$$\mathbf{D} = \mathbf{G}^T,$$

this way only the assembly of the gradient matrix is necessary.

The material derivative in Eq. (3.71) still needs to be discretized, that is where the semi-Lagrangian method acts upon.

3.2.3 Semi-Lagrangian Scheme

In this section the methodology used to discretize the material derivative will be formally presented. The principles of the semi-Lagrangian method dates back to the 1950's, in which a graphical method was used to solve the barotropic vorticity

equation, an atmospheric numerical model, Fjørtoft [53]. By the end of the decade, the first use of this method in advection problems comes in Wiin-Nielsen [54] referenced as quasi-Lagrangian advection. In this paper, the author focused on the backwards tracing of a set of particles over a single time step, originating the idea of **departure points**. Since the departure points rarely coincide with a grid point, an interpolation using the neighbouring grid points becomes necessary to determine the value of the variable of interest.

Throughout the 60's and 70's the semi-Lagrangian method was applied to different numerical models. However, it was in 1981 when Robert [55], demonstrated that compared to the Eulerian formulation for advection, the semi-Lagrangian scheme could use significantly larger time steps and remain numerically stable. The following year, Bates and MacDonald [56], verified that the scheme in [55] is stable. They also derived the semi-Lagrangian method for bidimensional problems, using bilinear or bi-quadratic interpolation schemes to evaluate the departure point value.

The use of the semi-Lagrangian method to discretize the material derivative in the Navier Stokes equations first appeared in Pironneau [41]. However, more recently Anjos [57] presented one- and two-step versions of the semi-Lagrangian scheme employed in two-phase flows.

Consider a scalar function γ, its material derivative in three dimensions is:

$$\frac{\mathrm{D}\gamma}{\mathrm{D}t} = \frac{\partial\gamma}{\partial t} + u\frac{\partial\gamma}{\partial x} + v\frac{\partial\gamma}{\partial y} + w\frac{\partial\gamma}{\partial z}. \tag{3.73}$$

This operator is then discretized by a first order finite difference approximation:

$$\frac{\mathrm{D}\gamma}{\mathrm{D}t} \approx \frac{\gamma^{n+1} - \gamma_d^n}{\Delta t}, \tag{3.74}$$

in which γ_d^n is the value of the scalar function at the departure point, $\mathbf{x}_d$. The departure point is calculated by:

$$\mathbf{x}_d = \mathbf{x}^n - \mathbf{v}^n \Delta t, \tag{3.75}$$

where $\mathbf{x}^n$ is always a node belonging to the original mesh, $\mathbf{v}$ is the calculated field velocity at instant n and Δt is the time step utilized in the simulation.

As the governing equations are written in the ALE framework, Eq. (3.75) has to be slightly modified in order to account for the moving mesh, hence the revised

equation for the departure points is:

$$\mathbf{x}_d = \mathbf{x}^n - (\mathbf{v}^n - \hat{\mathbf{v}}^n)\Delta t, \tag{3.76}$$

where $\hat{\mathbf{v}}$ is the mesh velocity for the current iteration.

Since the departure points do not coincide with mesh nodes the search-interpolation procedure from Xiu [58] is adapted to the current work. As the departure points are the displaced mesh nodes, the search starts from one of the node's neighbouring elements, shown in Fig. 3.4.

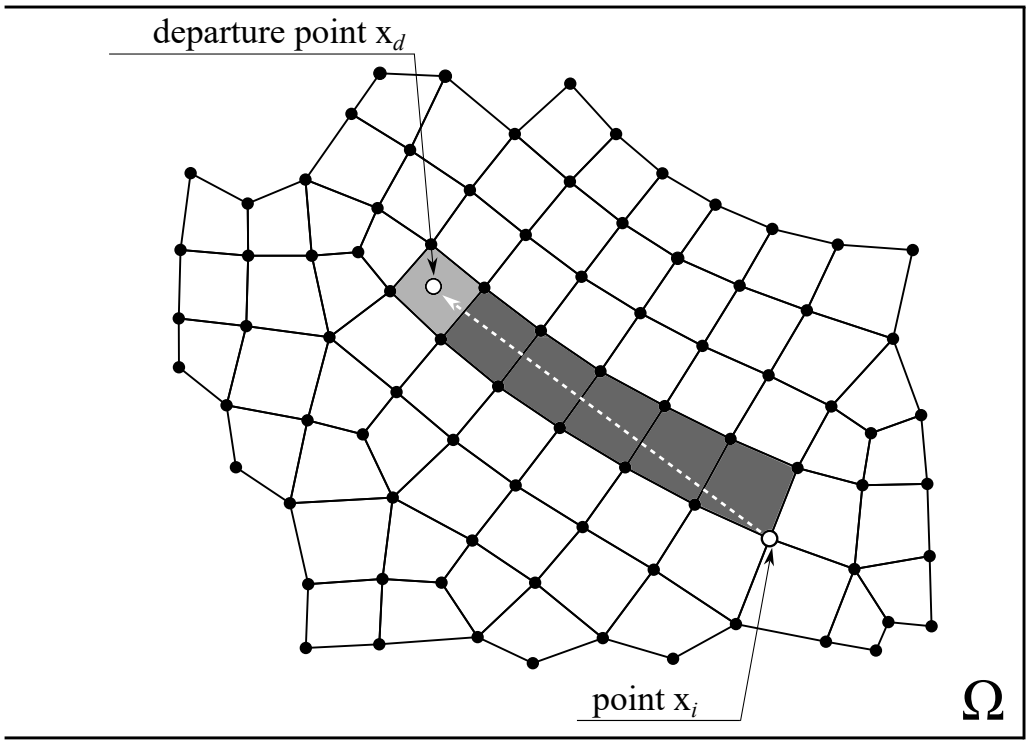

Figure 3.4: Schematic figure illustrating how the search algorithm works.

To check if the departure point is inside that element, the dot product between the vector connecting the element nodes, $\mathbf{x}_i$ to the departure point, $\mathbf{x}_d$ and the normal edge vector is computed, Fig. 3.5:

$$(\mathbf{x}_d - \mathbf{x}_i) \cdot \mathbf{n}_i \geq 0.$$

If all scalar products are positive, the departure point is inside the current element, however if the departure point is outside the current element, one of the dot products will be negative and the departure point will be located in the direction of that edge. This way the next element to be searched is identified, making the trajectory of the searching procedure linear.

The interpolation procedure is straightforward, since the shape functions of the finite element are used to interpolate the desired fields. That is:

$$\mathbf{v}_d = \sum_i^n N_i(\mathbf{x})\mathbf{v}_i, \tag{3.77}$$

in which $N_i(\mathbf{x})$ are the shape functions from the finite element employed in the spatial discretization.

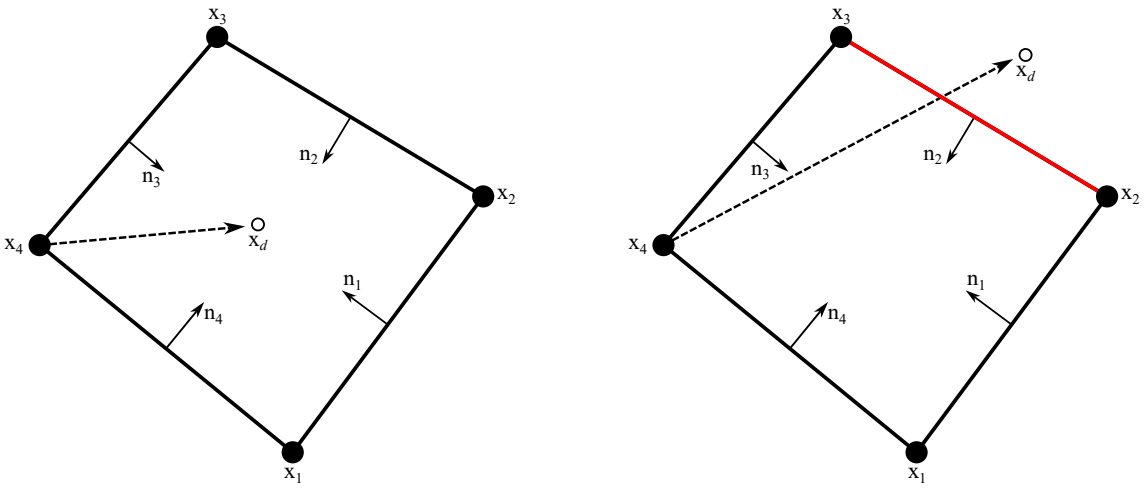

(a) (b)

Figure 3.5: Illustration of the procedure used to check if the departure point is inside an element. In (a) the displaced node is found inside the searched element, while in (b) the node is found outside the currently searched element and the search goes to the element that is adjacent to the second edge.

With the discretization of the substantial derivative using the semi-Lagrangian scheme, Eq. (3.71) is written as:

$$\mathbf{M}\frac{\mathbf{v}_i^{n+1} - \mathbf{v}_d^n}{\Delta t} - \mathbf{G}p_k^{n+1} + \frac{1}{Re}\mathbf{K}\mathbf{v}_i^{n+1} = 0. \tag{3.78}$$

Equations (3.72) and (3.78) are expressed in a block matrix notation:

$$\begin{bmatrix} \frac{\mathbf{M}}{\Delta t} + \frac{1}{Re}\mathbf{K} & -\mathbf{G} \\ \mathbf{D} & 0 \end{bmatrix} \cdot \begin{bmatrix} \mathbf{v}^{n+1} \\ p^{n+1} \end{bmatrix} = \begin{bmatrix} \frac{\mathbf{M}}{\Delta t}\mathbf{v}_d^n + \mathbf{bc}_\mathbf{v} \\ 0 + \mathbf{bc}_p \end{bmatrix}, \tag{3.79}$$

which may also be written in terms of the velocity components, u and v:

$$\begin{bmatrix} \frac{\mathbf{M}}{\Delta t} + \frac{1}{Re}\mathbf{K} & 0 & -\mathbf{G}_\mathbf{x} \\ 0 & \frac{\mathbf{M}}{\Delta t} + \frac{1}{Re}\mathbf{K} & -\mathbf{G}_\mathbf{y} \\ \mathbf{D}_\mathbf{x} & \mathbf{D}_\mathbf{y} & 0 \end{bmatrix} \cdot \begin{bmatrix} u^{n+1} \\ v^{n+1} \\ p^{n+1} \end{bmatrix} = \begin{bmatrix} \frac{\mathbf{M}}{\Delta t}u_d^n + \mathbf{bc}_u \\ \frac{\mathbf{M}}{\Delta t}v_d^n + \mathbf{bc}_v \\ 0 + \mathbf{bc}_p \end{bmatrix}. \tag{3.80}$$

In generic notation, the system is expressed as:

$$\mathbf{Ax} = \mathbf{b}, \tag{3.81}$$

in which:

$$\mathbf{A} = \begin{bmatrix} \frac{\mathbf{M}}{\Delta t} + \frac{1}{Re}\mathbf{K} & 0 & -\mathbf{G_x} \\ 0 & \frac{\mathbf{M}}{\Delta t} + \frac{1}{Re}\mathbf{K} & -\mathbf{G_y} \\ \mathbf{D_x} & \mathbf{D_y} & 0 \end{bmatrix}, \quad \mathbf{x} = \begin{bmatrix} u^{n+1} \\ v^{n+1} \\ p^{n+1} \end{bmatrix}, \quad \mathbf{b} = \begin{bmatrix} \frac{\mathbf{M}}{\Delta t}u_d^n + \mathbf{bc}_u \\ \frac{\mathbf{M}}{\Delta t}v_d^n + \mathbf{bc}_v \\ 0 + \mathbf{bc}_p \end{bmatrix}.$$

3.2.4 Mesh Element

In order to satisfy the "inf-sup" or Ladyzhenskaya–Babuška–Brezzi (LBB) condition a specific type of finite element needed to be chosen. The element of choice was the Mini quadrilateral. This type of element was first developed for the triangular element by Arnold *et al.* [59] to solve the Stokes problem. Later, Bai [60] adapted the previously development methodology to the $Q_1 - Q_1$ element, creating the Mini quadrilateral element. This element is the classical bilinear quadrilateral with an added node at its centroid enriched by a bubble function. That way the velocity field is calculated at five nodes while the pressure is calculated at the four vertices, satisfying the LBB condition.

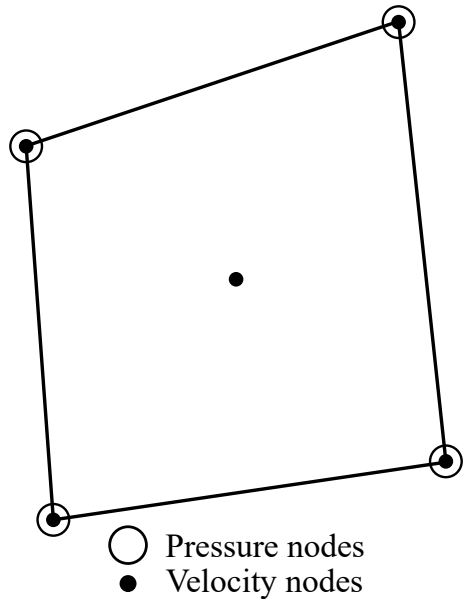

Figure 3.6: Schematics of the Mini quadrilateral element.

The shape functions for this element in natural coordinates are:

$$N_1 = \frac{(1-\xi)}{2}\frac{(1-\eta)}{2} - \frac{1}{4}(1-\xi^2)(1-\eta^2), \tag{3.82}$$

$$N_2 = \frac{(1+\xi)}{2}\frac{(1-\eta)}{2} - \frac{1}{4}(1-\xi^2)(1-\eta^2), \tag{3.83}$$

$$N_3 = \frac{(1+\xi)}{2}\frac{(1+\eta)}{2} - \frac{1}{4}(1-\xi^2)(1-\eta^2), \tag{3.84}$$

$$N_4 = \frac{(1-\xi)}{2}\frac{(1+\eta)}{2} - \frac{1}{4}(1-\xi^2)(1-\eta^2), \tag{3.85}$$

$$N_5 = (1-\xi^2)(1-\eta^2). \tag{3.86}$$

3.2.5 Numerical Integration

In order to use an unstructured mesh, a Gaussian integration library developed by professor Gustavo R. dos Anjos was used. The quadrature method was chosen because it yields the exact results for the evaluated integrals and it is numerically attractive. The numerical integration method used in this library will be explained herein.

This integration scheme is used to assemble the finite element matrices, therefore the integrals that need to be evaluated are of the form:

$$\int_{\Omega^e} f(x,y)\ \mathrm{d}\Omega^e = \int\int f(x,y)\ \mathrm{d}x\ \mathrm{d}y. \tag{3.87}$$

However, to use Gaussian quadrature to evaluate this integral, a transformation of coordinates needs to be performed first, since the integration method works only in the natural domain, which is bounded by the closed interval $[-1,1]$. In this domain $x \longrightarrow \xi$ and $y \longrightarrow \eta$, hence the double integral in Eq. (3.87) becomes:

$$I = \int_{-1}^{1}\int_{-1}^{1} f(x(\xi,\eta), y(\xi,\eta))\ |\det(\mathbf{J})|\ \mathrm{d}\xi\ \mathrm{d}\eta, \tag{3.88}$$

in which $\mathbf{J}$ is the Jacobian matrix, responsible for the transformation of coordinates from Cartesian to natural. Geometrically, the determinant of the Jacobian represents the area of the element in the Cartesian domain. Thus, the original integral can be evaluated in any domain through a transformation of coordinates. The integral in Eq. (3.88) is then approximated by:

$$I \approx \sum_{i}^{np_\xi}\sum_{j}^{np_\eta} f(\xi_i,\eta_j)\ |\det(\mathbf{J})|\ w_i w_j, \tag{3.89}$$

where np is the number of quadrature (integration) points, (ξ_i, η_j) are the natural coordinates of the Gaussian points and w is the weight associated with the integration points. This integration method can exactly evaluate integrals of polynomials of order $2n-1$ with n integration points.

For more detailed information on numerical integration, see Hughes [28] and Zienkiewicz [61].

3.2.6 Body Forces

The force a fluid exerts over a body is given by:

$$\mathbf{F} = \int_{\Gamma} \boldsymbol{\sigma} \cdot \mathbf{n} \, \mathrm{d}\Gamma, \tag{3.90}$$

where $\boldsymbol{\sigma}$ represents the stress tensor. As previously shown, this tensor may be written as:

$$\boldsymbol{\sigma} = -p\mathbf{I} + \mu[\nabla \mathbf{v} + (\nabla \mathbf{v})^T], \tag{3.91}$$

in which, μ represents the dynamic viscosity if dealing with the dimensional problem or $\mu = 1/Re$, if dealing with the non-dimensional form of the governing equations. Considering the problem in two dimensions, the matrix notation of the newtoninan stress tensor is equal to:

$$\boldsymbol{\sigma} = \begin{bmatrix} -p & 0 \\ 0 & -p \end{bmatrix} + \mu \begin{bmatrix} \frac{\partial u}{\partial x} & \frac{\partial u}{\partial y} \\ \frac{\partial v}{\partial x} & \frac{\partial v}{\partial y} \end{bmatrix} + \mu \begin{bmatrix} \frac{\partial u}{\partial x} & \frac{\partial v}{\partial x} \\ \frac{\partial u}{\partial y} & \frac{\partial v}{\partial y} \end{bmatrix}, \tag{3.92}$$

$$\boldsymbol{\sigma} = \begin{bmatrix} -p + 2\mu\frac{\partial u}{\partial x} & \mu\left(\frac{\partial u}{\partial y} + \frac{\partial v}{\partial x}\right) \\ \mu\left(\frac{\partial v}{\partial x} + \frac{\partial u}{\partial y}\right) & -p + 2\mu\frac{\partial v}{\partial y} \end{bmatrix}. \tag{3.93}$$

In terms of the finite element matrices:

$$\sigma_{xx} = -p + 2\mu \mathbf{G}_{\mathbf{v_x}} u, \tag{3.94}$$

$$\sigma_{xy} = \sigma_{yx} = \mu(\mathbf{G}_{\mathbf{v_y}} u + \mathbf{G}_{\mathbf{v_x}} v), \tag{3.95}$$

$$\sigma_{yy} = -p + 2\mu \mathbf{G}_{\mathbf{v_y}} v. \tag{3.96}$$

With the stress tensor calculated, the forces may be computed by:

$$F_x = \oint_{\Gamma} \left[-p + 2\mu\frac{\partial u}{\partial x}\right] n_x + \left[\mu\left(\frac{\partial u}{\partial y} + \frac{\partial v}{\partial x}\right)\right] n_y \, \mathrm{d}\Gamma, \tag{3.97}$$

$$F_y = \oint_\Gamma \left[\mu \left(\frac{\partial v}{\partial x} + \frac{\partial u}{\partial y} \right) \right] n_x + \left[-p + 2\mu \frac{\partial v}{\partial y} \right] n_y \, \mathrm{d}\Gamma. \tag{3.98}$$

In terms of the discretized domain and operators:

$$F_x = \mathbf{M}_\Gamma \cdot [(-p + 2\mu \mathbf{G}_{\mathbf{v_x}} u) n_x + \mu (\mathbf{G}_{\mathbf{v_y}} u + \mathbf{G}_{\mathbf{v_x}} v) n_y], \tag{3.99}$$

$$F_y = \mathbf{M}_\Gamma \cdot [(-p + 2\mu \mathbf{G}_{\mathbf{v_y}} v) n_y + \mu (\mathbf{G}_{\mathbf{v_x}} v + \mathbf{G}_{\mathbf{v_y}} u) n_x], \tag{3.100}$$

in which $\mathbf{M}_\Gamma$ is the boundary mass matrix and $\mathbf{G}_\mathbf{v}$ is the gradient operator for the velocity vector. The boundary element mass matrix is defined for the line segment between two nodes and is given by:

$$\mathbf{m}_\Gamma^e = \frac{h}{6} \begin{bmatrix} 2 & 1 \\ 1 & 2 \end{bmatrix}, \tag{3.101}$$

where h is the length of the line segment, which is given by:

$$h = \sqrt{(x_j - x_i)^2 + (y_j - y_i)^2}. \tag{3.102}$$

An assembly process is necessary to obtain $\mathbf{M}_\mathbf{\Gamma}$. Visually speaking, $\mathbf{m}_\Gamma^e$ corresponds to the line segment connecting two adjacent black dots in Fig. 3.7, while $\mathbf{M}_\Gamma$ represents the whole closed boundary.

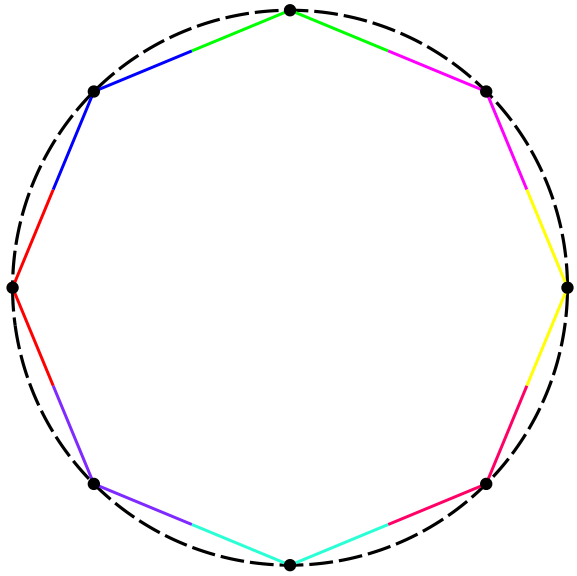

Figure 3.7: Illustration of the integration region, each colour represents the region over which the integration is taking part, based on the definition of the normal nodal vectors.

Since $\mathbf{v}$ and p are stored at the mesh nodes, the normal vector used Eq. (3.90) must also be defined at the nodes. In order to compute nodal normal vectors, the

tangent edge vectors for the boundary Γ are computed first. Then they are rotated by 90° so that they become edge normal vectors. With these edge normals the unit nodal normals can be estimated as the summation of the adjacent edge normals with respect to the node of interest, for example:

$$\hat{\mathbf{n}}_i = \frac{\mathbf{n}_1 + \mathbf{n}_2}{||\mathbf{n}_1 + \mathbf{n}_2||}. \tag{3.103}$$

An illustration of the described procedure is presented in Fig. 3.8.

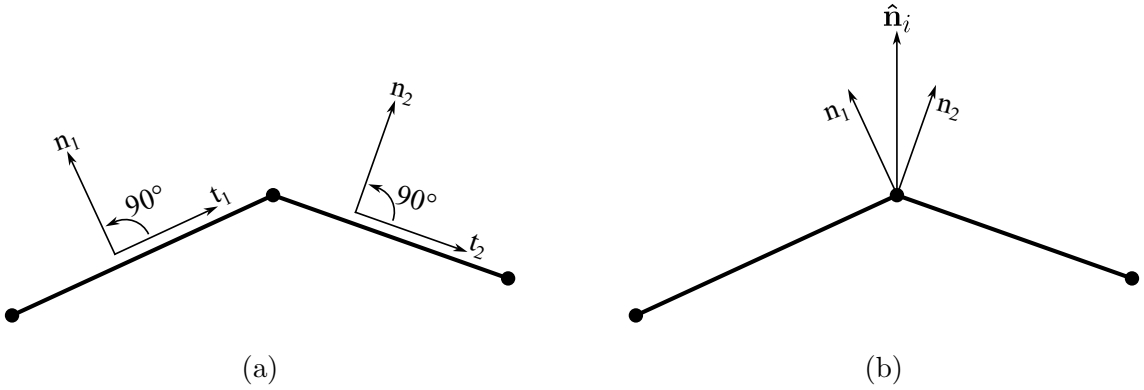

(a) (b)

Figure 3.8: Representation of the normal vector in a bidimensional space. (a) The normal edge vector is calculated by computing the tangential edge vector and rotating it by 90° degrees. (b) The nodal normal vector is then computed by the summation of the adjacent normal edge vectors.

The relationship between the computed forces and the non-dimensional drag and lift coefficients is given by:

$$c_d = \frac{F_x}{\frac{1}{2}\rho D U^2}, \tag{3.104}$$

$$c_l = \frac{F_y}{\frac{1}{2}\rho D U^2}. \tag{3.105}$$

3.3 Computational Code

In this section, aspects of the computational code will be explained. Mesh generation, data structures and the main algorithm will be detailed in the following text.

3.3.1 Mesh Generation

In order to numerically solve the Navier-Stokes equations using the FEM a spatial discretization of the fluid domain must be performed first. This discretization is done by the open source mesh generator software *Gmsh* [62]. Unfortunately, *Gmsh* does not support the Mini element, therefore a straightforward post-meshing processing is required to add the bubble node.

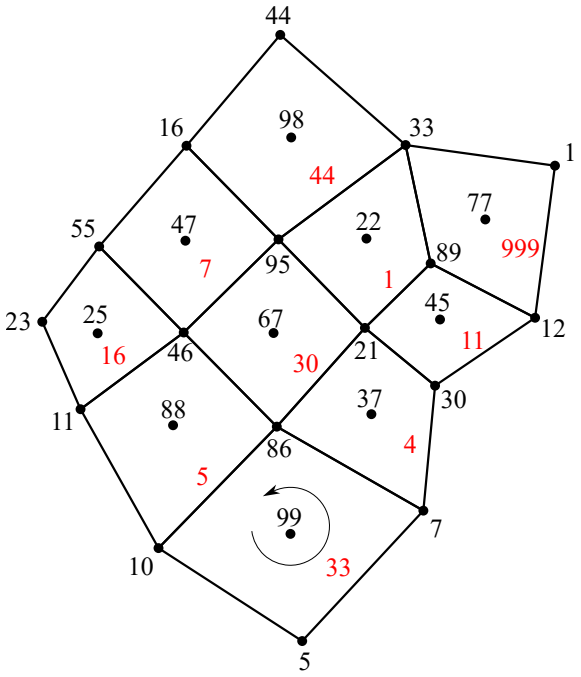

Figure 3.9: Example of a quad mini mesh to illustrate the data structures used in the code.

In order to assemble the global finite element matrices a connectivity array is exported with the generated mesh. In this work, the array chosen was the IEN structure. Considering the mesh shown in Fig. 3.9, the IEN for elements 30 and 999 are:

```
IEN[30] = [21, 95, 46, 86, 67]
IEN[999] = [89, 12, 1, 33, 77]
```

where the first four numbers indicate the vertex nodes and the last number, the bubble node. Every element must be numbered following the same orientation, in this work the orientation chosen was anti-clockwise.

3.3.2 Data Structures

In order to facilitate the implementation of some of the methods used, different data structures were needed.

The first of them was the neighbouring elements with respect to node i. For example, consider the nodes 16 and 95 in the mesh shown in Fig. 3.9. The neighbouring elements for these nodes are:

```
neighElem[16] = [7, 44]
neighElem[95] = [30, 1, 44, 7]
```

It is clear that boundary nodes will have less neighbouring elements than a node deeper into the domain.

An essential data structure for the semi-Lagrangian method is the opposite element to an element edge. It is with this structure that the method knows in which element it should search for the departure point. Considering elements 30 and 33 from the mesh in Fig. 3.9, their opposite elements are:

```
oElem[30] = [1, 7, 5, 4]
oElem[33] = [-1, 4, 5, -1]
```

The -1 value indicates that there is no opposite element to that edge.

Finally, the minimum distance structure is used to impose a mesh velocity based on the distance between the rigid body and a node inside a specific mesh region. Two lists are stored, one with the index of the boundary node which is closer to node i and another storing the distance between node i and the closest boundary node. Figure 3.10 is referenced to better visualize this data structure. The mesh which is subjected to movement is defined by the region inside the pink coloured circumference, hence the mesh outside this circle, gray coloured, is fixed. The minimum distance data structure is assembled only for the black coloured mesh and each node inside this region has a distance to a node lying on the boundary of the moving geometry, which is represented by the blue circumference in Fig. 3.10. However only the smallest distance is stored, that is, the distance to a specific node lying on the blue boundary. This structure is used to apply a linearly decaying velocity up to the pink boundary, which always has a mesh velocity equal to zero.

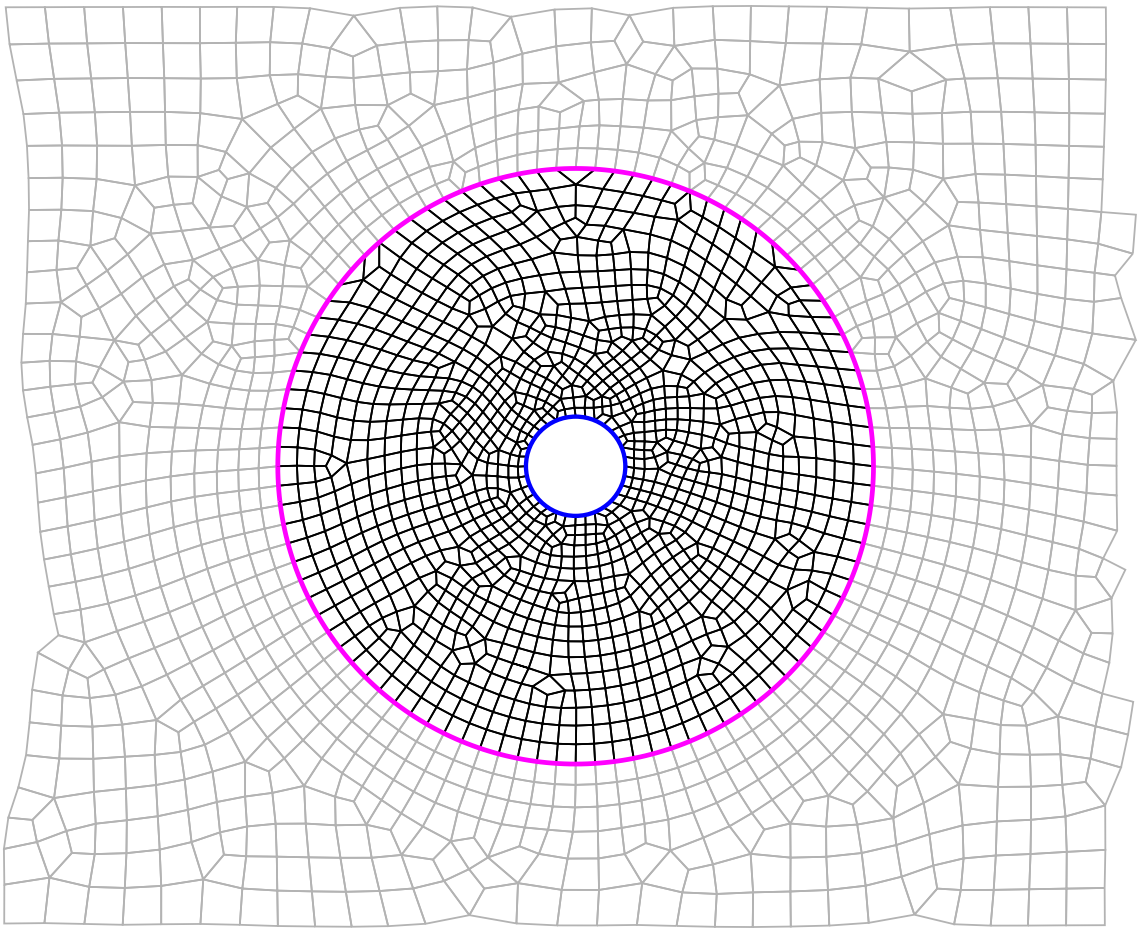

Figure 3.10: Illustration of the minimum distance data structure.

3.3.3 Algorithm

A general description of the proposed algorithm is presented below, emphasizing each of the necessary steps performed during the computations.

The algorithm begins with the loop responsible for time marching, in which it calculates a user specified number of iterations, `nIter`. Then an arbitrary mesh velocity is calculated. In this work, this velocity is proportional to the calculated moving boundary velocity. After that the mesh nodes are moved with the calculated mesh velocity. With the new mesh nodes coordinates, the element matrices are computed and the assembly procedure for the global matrices takes place.

After assembling the finite element matrices the block matrix is built following Eq. (3.81) and the constant vector is initialized, line 5 of Algorithm 1. The boundary conditions are then applied to the matrix system. For Dirichlet type condition, the row is zeroed while the main diagonal component of the row is equal to 1.

Now, the semi-Lagrangian scheme begins with the calculation of the departure

points, following the equation in line 7 of Algorithm 1. Then the search-interpolation procedure starts, according to the previously described theory. For the sake of clarity, this procedure does not loop through all mesh nodes, `nnodes`, which are the original mesh nodes *Gmsh* provides plus the added node at the centroid of each element. Therefore, `nnodes = npoints + ne`, where `npoints` are the mesh nodes at each vertex of the quadrilateral elements and `ne` is the number of elements. The search-interpolation scheme yields the interpolated velocity vector based on the calculated departure points, subjected to the previously defined velocity boundary conditions.

After that, the previously initialized **b** vector is populated based on Eq. (3.81) and the boundary conditions for velocity and pressure are applied on it. The following step is the solution of the matrix system, in which the objective is to find vector **x**, where the velocity and pressure vectors are stored.

From line 14 onwards of the algorithm, the velocity and pressure fields used are those yielded by the solution of the matrix system. The computation of the stress tensor is done following Eqs. (3.94), (3.95) and (3.96). The stress tensor is then projected onto the nodal normals of the boundary of interest and integrated along it to calculate the fluid forces acting on it. The last step of the algorithm consists of determining the moving boundary velocity based on the calculated forces, which can be evaluated in multiple ways. These different methods are made explicit later on.

Algorithm 1

1: **for** n $<$ nIter **do** ▷ ODE time loop
2: Calculate mesh velocity: $\hat{\mathbf{v}}$
3: Move mesh nodes with: $\mathbf{x}^{n+1} = \mathbf{x}^n + \hat{\mathbf{v}}\Delta t$
4: Assemble FE matrices: $\mathbf{M}, \mathbf{K}, \mathbf{G_x}, \mathbf{G_y}, \mathbf{D_x}, \mathbf{D_y}, \mathbf{G_{v_x}}, \mathbf{G_{v_y}}$
5: Build block matrix $\mathbf{A}$ and initialize $\mathbf{b}$ vector
6: Apply boundary conditions on $\mathbf{A}$ for $\mathbf{v}$ and p
7: Compute the departure points: $\mathbf{x}_d^n = \mathbf{x}^{n+1} - (\mathbf{v} - \hat{\mathbf{v}})\Delta t$
8: **for** i $<$ nnodes **do**
9: Search-interpolation procedure
10: **end for**
11: Apply boundary conditions on interpolated velocity vector $\mathbf{v}_d$
12: Compute $\mathbf{b}$ vector and apply boundary conditions for $\mathbf{v}$ and p
13: Solve linear system for $\mathbf{v}$ and p: $\mathbf{Ax} = \mathbf{b}$
14: Extract the $\mathbf{v}$ and p vectors from $\mathbf{x}$ and apply boundary conditions
15: Compute stress tensor: $\boldsymbol{\sigma} = -p\mathbf{I} + \mu[\nabla\mathbf{v} + (\nabla\mathbf{v})^T]$
16: Calculate aerodynamic forces: $\mathbf{F} = \mathbf{M}_{\boldsymbol{\Gamma}}\boldsymbol{\sigma}_n$
17: Compute moving boundary velocity: $\mathbf{v}_{\boldsymbol{\Gamma}}$
18: **end for**

Chapter 4

Results and Discussion

In this chapter, the validation problems are presented and their solutions are compared with the obtained results from the methodology previously described in this work. After that, a series of simulations involving vortex-induced vibrations are performed in order to test the capability of the present methodology to properly capture and predict this fluid-structure interaction problem. These simulations include forced and free oscillations in the transverse direction as well as an elastically mounted geometry which is free to vibrate in the two translational degrees of freedom present in a plane.

4.1 Hagen Poiseuille

The Hagen Poiseuille flow describes the laminar flow inside a circular pipe. It has an analytical velocity profile which makes this problem a sort of benchmark in order to validate the accuracy of the computational code, considering laminar flows. Figure 4.1 illustrates the geometry and boundary conditions of this type of flow.

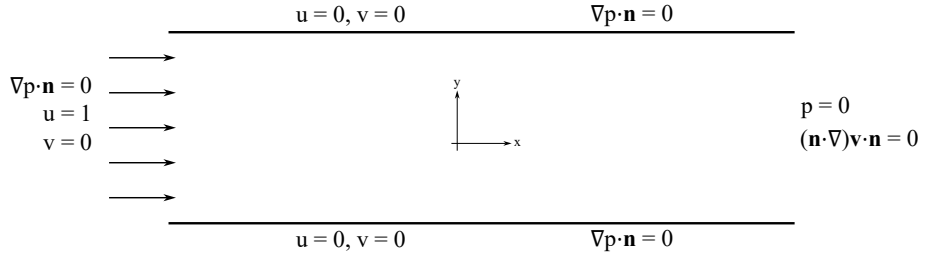

Figure 4.1: Schematics of the Hagen Poiseuille flow with boundary conditions.

According to Batchelor [50], the velocity profile for this problem is:

$$u(y) = -\frac{1}{2\mu}\frac{\partial p}{\partial x}(yh - y^2), \tag{4.1}$$

where h is the distance between horizontal plates. The pressure gradient in this example is given by:

$$\frac{\partial p}{\partial x} = -12\mu\frac{Q}{h^3},$$

where Q is the volumetric flow rate. Considering that the velocity magnitude at the entrance is U, and by definition

$$Q = \int_A \mathbf{v}\cdot\mathbf{n}\,\mathrm{d}A = Uh,$$

substitution of the flow rate per unit length into the pressure gradient expression yields:

$$\frac{\partial p}{\partial x} = -12\mu\frac{U}{h^2}. \tag{4.2}$$

Plugging Eq. (4.2) into Eq. (4.1) results in:

$$u(y) = 6\frac{U}{h^2}(yh - y^2). \tag{4.3}$$

For simulation purposes, $U = 1$ and $h = 1$, hence the maximum value for the velocity profile must have a magnitude of $u_{\max} = 1.5$ and occur at $y = h/2$. The mesh geometry has $L = 5$ and the velocity profile was evaluated at $L = 4.9$, to ensure the flow is fully developed. Based on inlet flow velocity and mesh geometry the simulated Reynolds number was equal to 10, while the time step used was equal to 0.001 and 4000 iterations were computed.

Three different mesh refinements were used to simulate this problem, their information is available in Table 4.1. The computational time required to perform the simulations are also available in Tab. 4.1. The u-velocity profile for each of the simulations is presented in Fig. 4.2. It is clear that the current methodology correctly predicts the velocity profile despite a small error that tends to decrease as the mesh is further refined. The velocity and pressure contours can be seen in Fig. 4.3.

Table 4.1: Computational time for the three meshes employed in the Hagen Poiseuille flow.

Identification	No. Elements	Total time [h]	Time per iteration [s]
Mesh 18k	17641	6	5
Mesh 50k	50000	29	30
Mesh 200k	200000	262	240

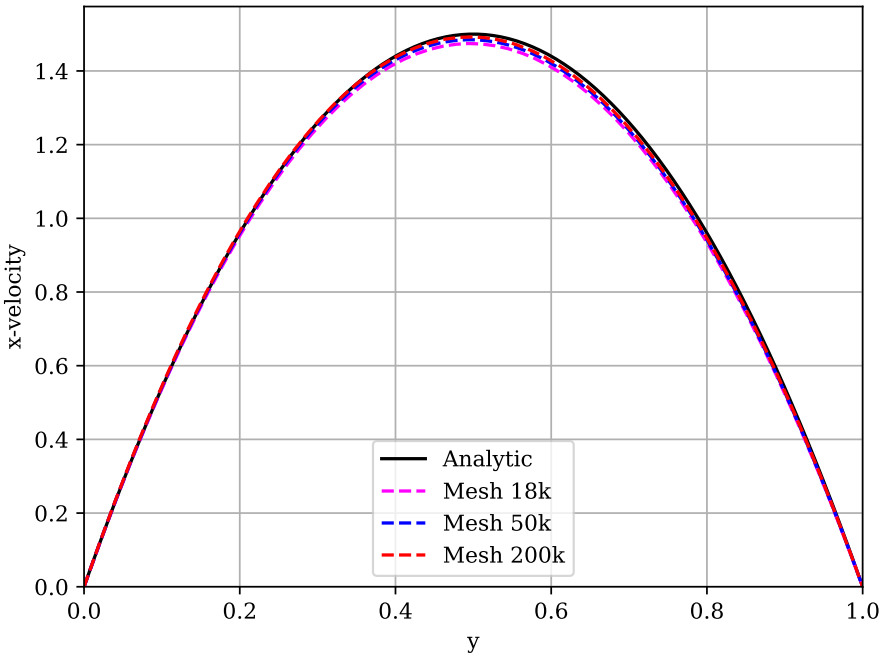

Figure 4.2: Comparison between the simulated u-velocity profile at $L = 4.9$ and the analytical velocity profile.

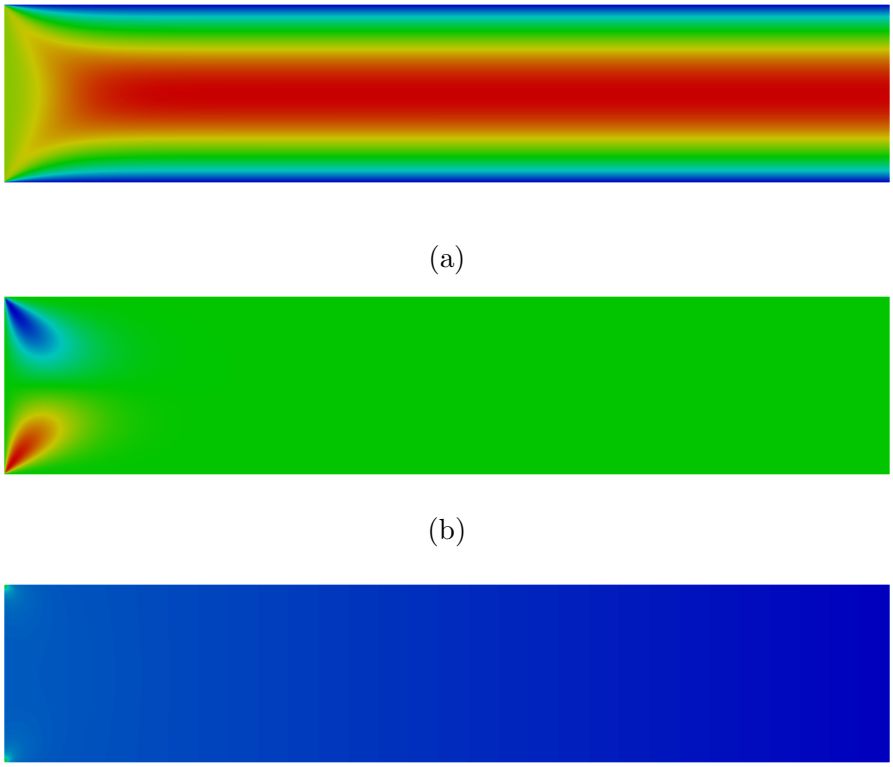

(a)

(b)

(c)

Figure 4.3: Contours for Mesh 200k for $Re = 10$. (a) u-velocity; (b) v-velocity; (c) pressure.

4.2 Lid-Driven Cavity

The lid-driven cavity problem consists of the flow inside a box that has an infinite moving lid. This problem has long been used to validate CFD codes for multiple Reynolds numbers since it has been studied by a number of researchers such as Ghia *et al.* [63] and Zienkiewicz *et al* [7]. Despite the absence of an analytical solution this problem is considered a benchmark because its laminar solution is steady and the boundary conditions are compatible with most numerical approaches. Figure 4.4 illustrates the driven cavity geometry and boundary conditions. The mesh geometry is a 1 by 1 square composed by 16384 quadrilateral elements and 33025 nodes, while the time step used was $\Delta t = 0.001$.

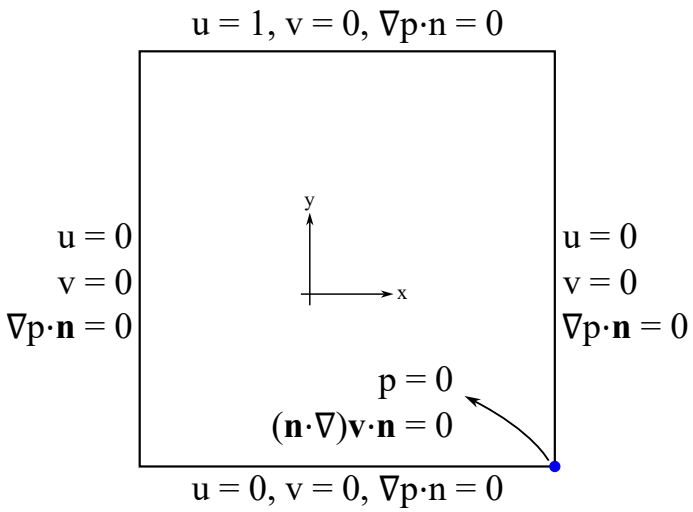

Figure 4.4: Schematics of the lid-driven problem with boundary conditions.

Table 4.2: Computational time for the three driven cavity simulations.

Re	Iterations	Total time [h]	Time per iteration [s]
100	25000	52	8
400	50000	85	6
1000	50000	85	6

The driven cavity was simulated at three different Reynolds numbers: 100, 400 and 1000. The computational time spent on each case is shown in Tab. 4.2. The results were then compared to those from Ghia *et al.* [63], which can be seen in Figs. 4.5 and 4.6.

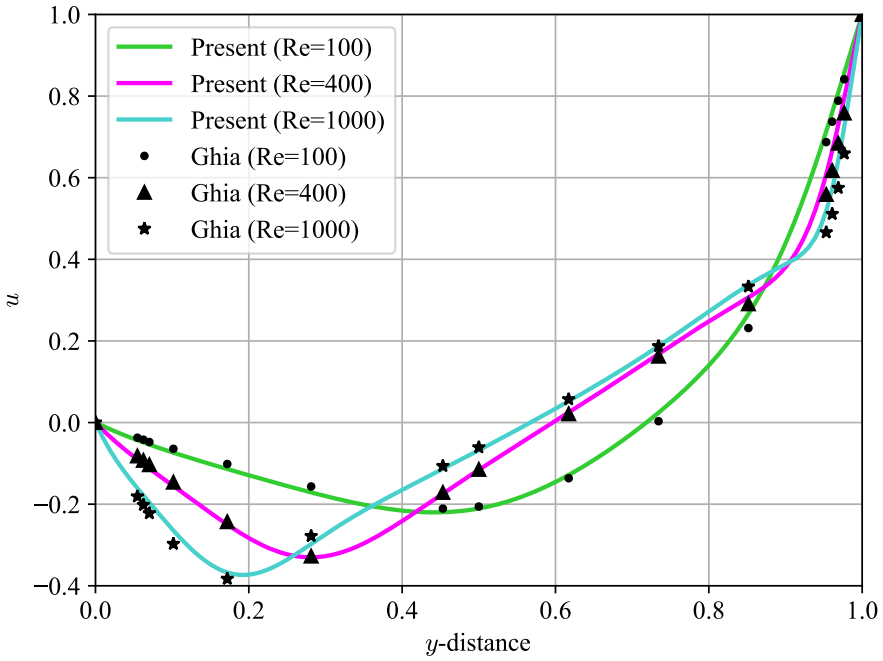

Figure 4.5: u-velocity profiles along the vertical line passing through the geometric centre of the fluid domain.

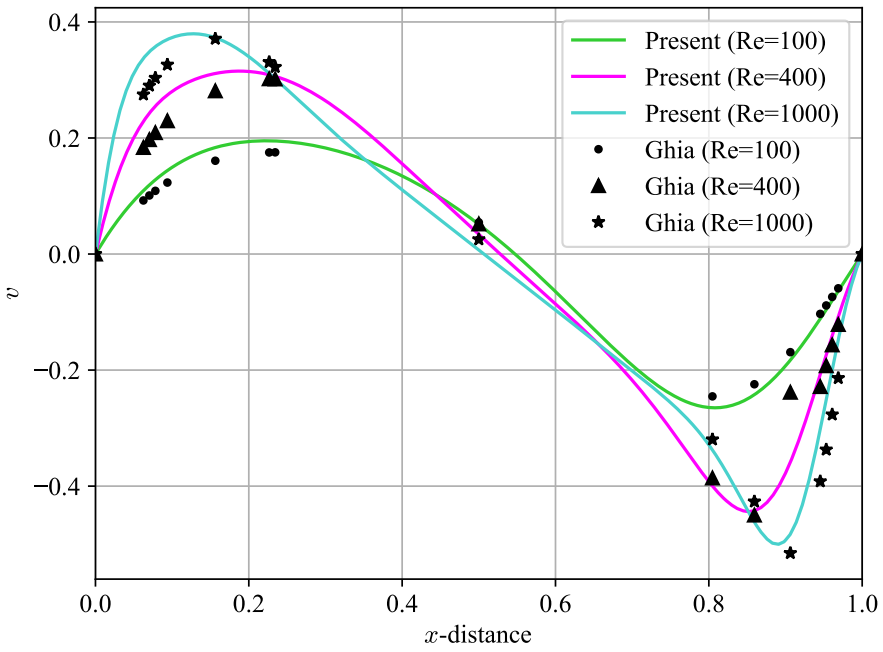

Figure 4.6: v-velocity profiles along the horizontal line passing through the geometric centre of the fluid domain.

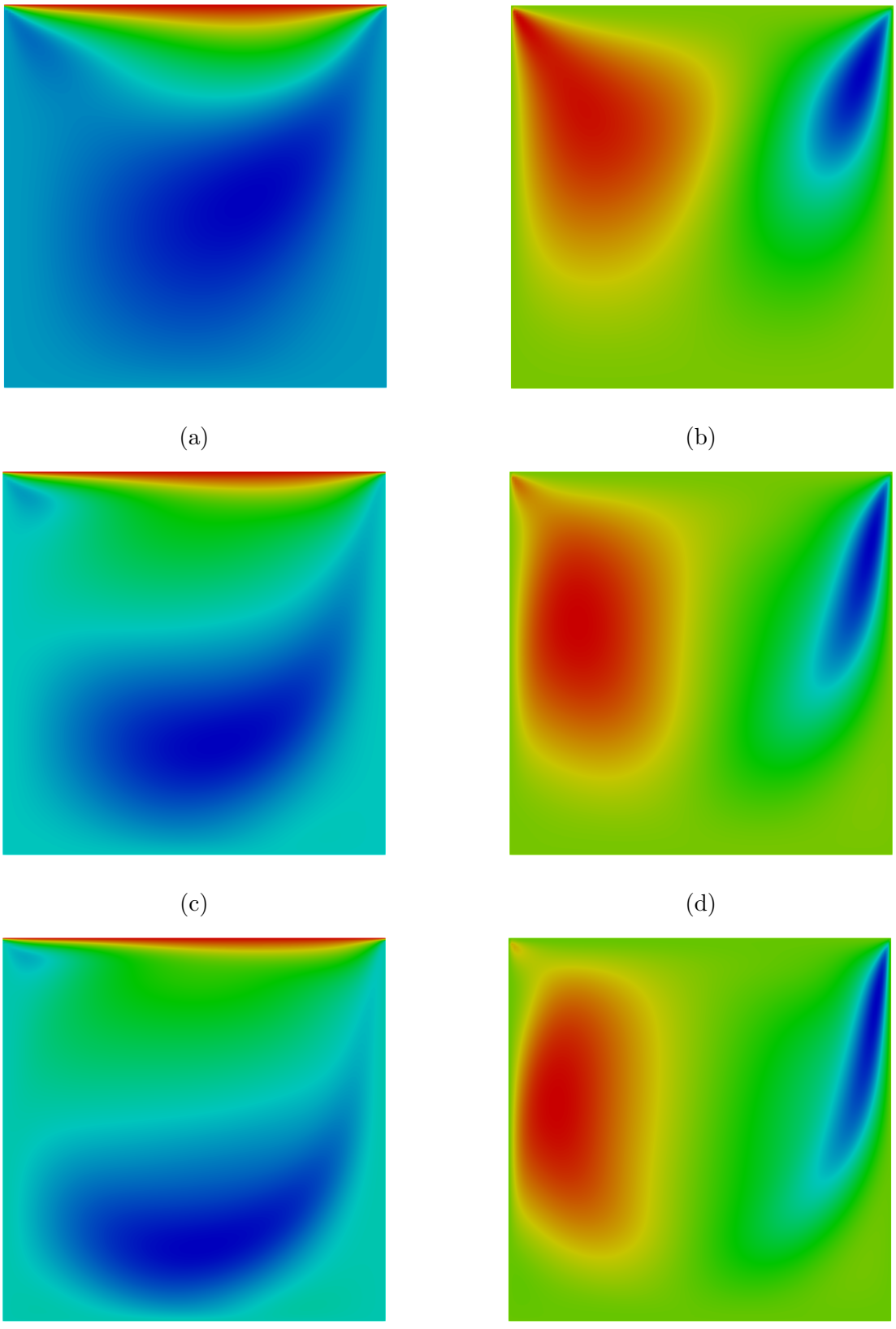

Figure 4.7: Velocity contours for the driven cavity. Left column represents u-velocity while the right one presents v-velocity. (a) and (b) $Re = 100$; (c) and (d) $Re = 400$; (e) and (f) $Re = 1000$.

4.3 Flow Past a Cylinder

This problem can used to validate the computational code as well as the method utilized to compute the fluid forces since it has been studied by multiple researchers utilizing different numerical methods. Hence, there is a lot of available data in the literature.

4.3.1 Fixed

Simulations were performed with a fixed cylinder in order to evaluate the force computation algorithm. A mesh and time step sensitivity analysis were also conducted so as to understand the influence of h-refinement and time step decrease on the calculated results. In order to make these assessments the results obtained from the presented methodology were compared to the example 4.4 from Zienkiewicz [7].

To study the influence of h-refinement, 6 different meshes were used, which are identified in Table 4.3.

Table 4.3: Mesh identification and its details.

Mesh	No. Elements	No. Nodes
h_1	4358	8847
h_2	6236	12627
h_3	9722	19615
h_4	15312	30867
h_5	22086	44571
h_6	33058	66605

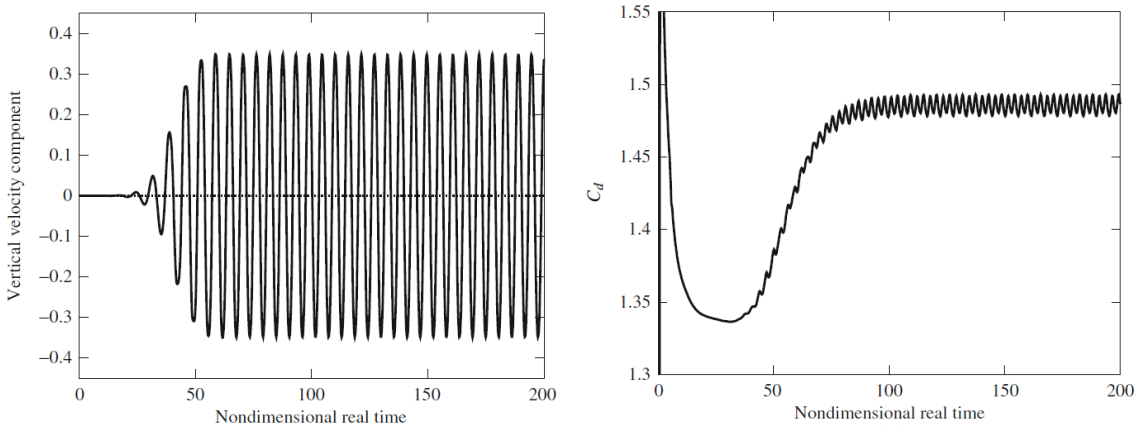

(a) (b)

Figure 4.8: Reference results from Zienkiewicz [7] - (a) Vertical velocity component at the mid-point of the outlet boundary; (b) drag history.

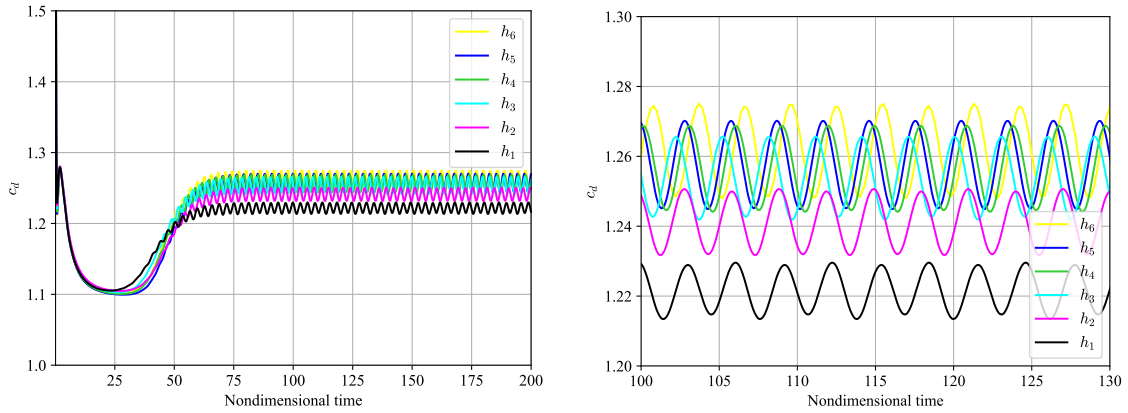

(a) (b)

Figure 4.9: Drag time history for six different mesh refinements - (a) Full time history; (b) zoomed in view.

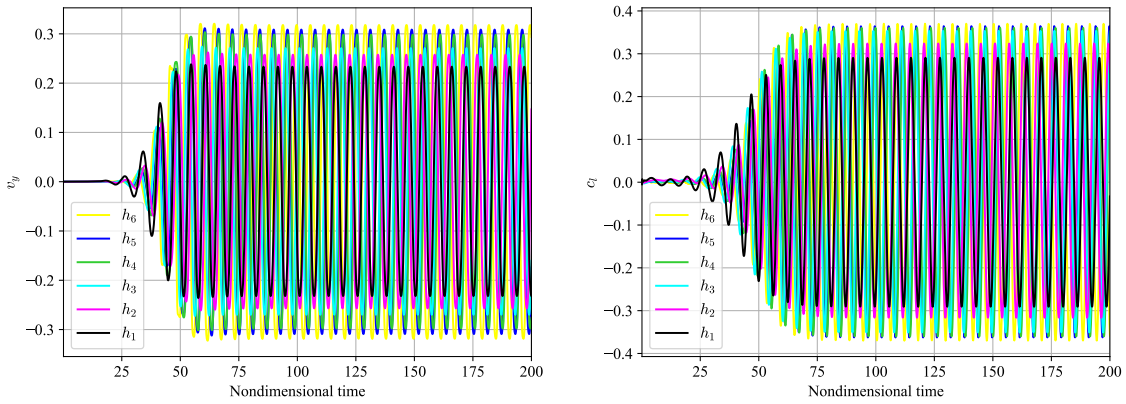

(a) (b)

Figure 4.10: Time histories for six different mesh refinements - (a) Vertical velocity component; (b) Lift coefficient.

From Figs. 4.9 and 4.10 it is clear that by refining the computational mesh the mean drag coefficient increases slightly, a minor phase shift is observed and an increase in amplitude for the drag coefficient is noticed. While the amplitudes of v_y and lift coefficient increases as well. Table 4.4 quantitatively summarizes the variables of interest for these simulations.

Table 4.4: Comparison of the results obtained for different h-refinements.

Mesh	c_d^{mean}	$c_l^{\max}$	$c_l^{\mathbf{rms}}$	St
h_1	1.22	0.29	0.18	0.160
h_2	1.23	0.32	0.20	0.165
h_3	1.24	0.35	0.22	0.170
h_4	1.24	0.36	0.22	0.170
h_5	1.24	0.36	0.23	0.170
h_6	1.25	0.37	0.23	0.170

For the time step refinement analysis, the h_3 mesh was employed, see Fig. 4.11. The different time steps are presented in Table 4.5.

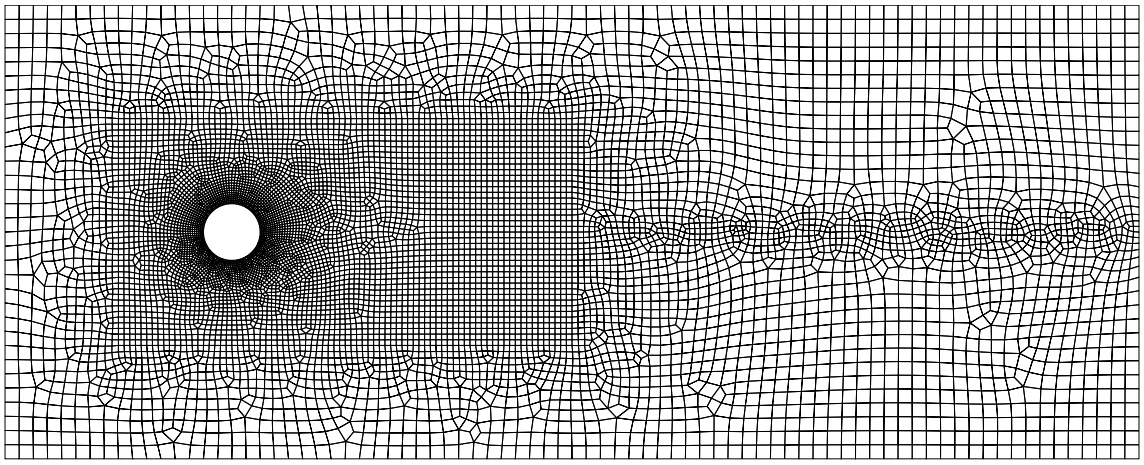

Figure 4.11: Mesh h_3 used for the time step sensitivity analysis.

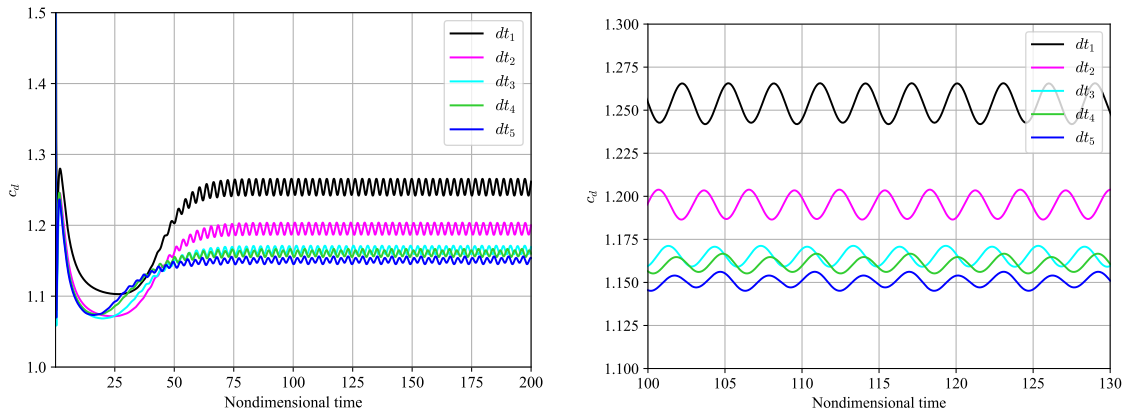

(a) (b)

Figure 4.12: Drag time history for five different dt refinements - (a) Full time history; (b) zoomed in view.

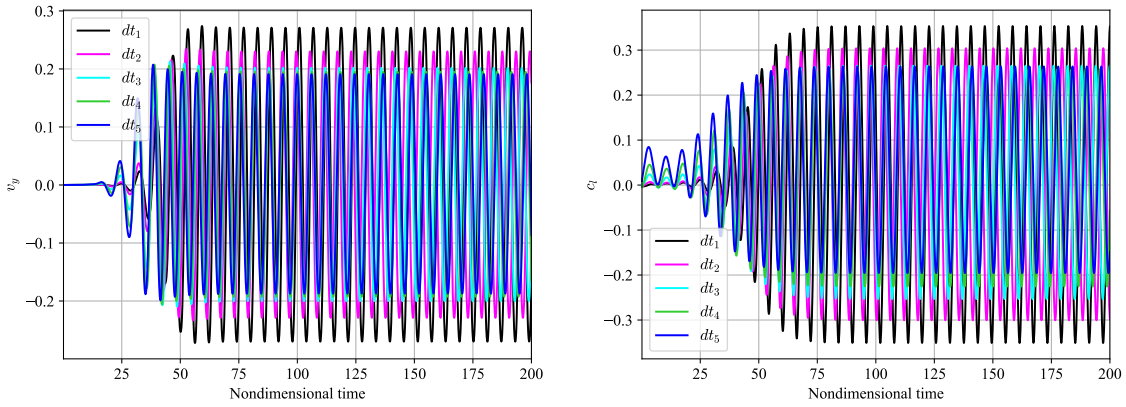

(a) (b)

Figure 4.13: Time histories for five different dt refinements - (a) Vertical velocity component; (b) Lift coefficient.

By analysing Figs. 4.12 and 4.13 it becomes clear that by decreasing the time step of the simulation the mean drag coefficient decreases and so does its oscillation amplitude. An interesting thing to notice is that for dt_5 a new oscillation frequency appears in the drag coefficient, which the author believes has no physical meaning and is a result of numerical errors. The amplitude of v_y and lift coefficient also decreases, however its mean value grows further from zero as the time step is refined. Table 4.5 quantitatively summarizes the variables of interest.

Table 4.5: Time step value and comparison of the results obtained for different dt-refinements.

Time step	Δt	c_d^{mean}	$c_l^{\max}$	$c_l^{\mathbf{rms}}$	St
dt_1	0.1	1.24	0.35	0.22	0.170
dt_2	0.05	1.19	0.30	0.19	0.170
dt_3	0.02	1.17	0.26	0.16	0.165
dt_4	0.01	1.17	0.26	0.15	0.165
dt_5	0.005	1.16	0.26	0.15	0.165

All in all, it is apparent that h-refinement and dt decrease have opposite effects, hence a balance between them must be found so as to guarantee optimal results. It is also clear that the present methodology slightly underestimates the aerodynamic coefficients despite their proper qualitative behaviour, see Tab. 4.6. The author

Table 4.6: Comparison of the results obtained by different researchers for the flow past a cylinder at $Re = 100$.

Reference	c_d^{mean}	$c_l^{\max}$	$c_l^{\mathbf{rms}}$	St
Shiels *et al.* [21]	1.33	-	0.30	0.17
Singh and Mittal [20]	1.35	-	0.25	0.17
Posdziech and Grundmann [64]	1.31	-	0.32	0.16
Wanderley *et al.* [65]	1.30	-	0.22	0.16
Placzek *et al.* [23]	1.37	0.33	0.23	0.17
Decuyper [66]	1.37	-	0.23	0.17
Present	1.19	0.30	0.19	0.17

attributes this discrepancy to the type of finite element employed in this work, the Mini quadrilateral. Therefore, a further study is needed to properly verify this hypothesis.

4.3.2 Forced Oscillation

A set of forced cross-flow oscillations were performed in order to capture the lock-in phenomenon based on an amplitude versus frequency map according to the experiments of Koopmann [8], which is shown in Fig. 4.15.

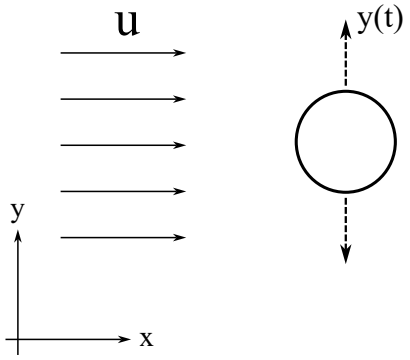

Figure 4.14: Illustration of the prescribed oscillation problem.

A similar methodology to the ones adopted by Nobari [22] and Placzek *et al.* [23] is used to prescribe the cylinder's oscillation. In these simulations the cylinder had a prescribed displacement governed by Eq. (4.4):

$$y(t) = A \sin(2\pi f_0 t), \tag{4.4}$$

where A represents the cylinder's non-dimensional amplitude of vibration and f_0 the frequency in which the cylinder is forced to oscillate, while Fig. 4.14 illustrates the cylinder motion. However, a non-dimensional frequency is defined as $F = f_0/f_s$, in which f_s represents the Strouhal frequency at the simulated Reynolds number.

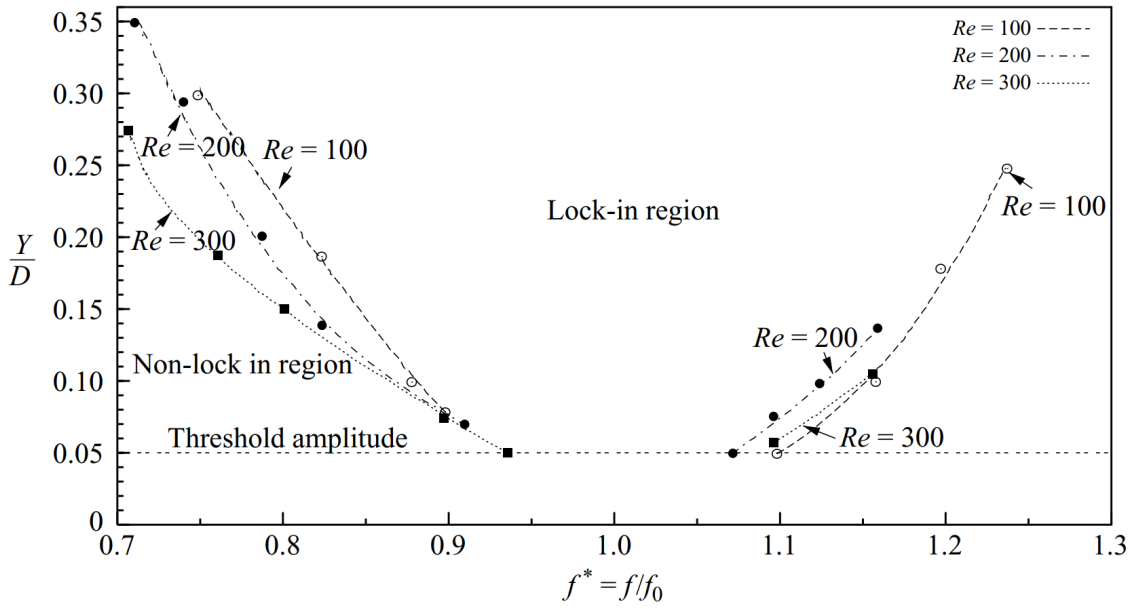

Figure 4.15: Lock-in region for different Reynolds numbers based on the experimental data for forced oscillations from Koopmann [8]. The y-axis represents the cross-flow oscillation amplitude while the x-axis gives the ratio between the vortex shedding frequency for the vibrating (f) and stationary (f_0) cylinder, figure from Prasanth and Mittal [9].

The occurrence of lock-in is determined by a spectral analysis of the temporal evolution of the lift coefficient. Whenever a second peak frequency appears on the Power Spectral Density (PSD) of the lift coefficient, the configuration is unlocked, meaning their is no synchronization based on the specified amplitude (A) and frequency ($f_0 = f_s F$). Not only this, but the phase plot for c_l versus y^* is analysed, since the lock in region is defined as the domain in which the temporal evolution of lift coefficient is purely sinusoidal and governed by forced oscillation frequency Nobari and Naredan [22].

In order to study forced response oscillations, a prescribed amplitude of $A = 0.30$ was adopted while varying the non-dimensional frequency $0.50 \leq F \leq 1.50$. The computational domain used to perform the simulations is based on the geometry

presented in Placzek *et al.* [23], which can be seen in Fig. 4.16. The mesh used in the following simulations is shown in Fig. 4.17, it has 22310 elements and 44968 nodes.

The boundary condition for the cylinder is known as kinematic coupling, and it states: $\mathbf{v}_\Gamma = \dot{\mathbf{x}}$, where $\mathbf{v}_\Gamma$ is the boundary velocity vector and $\dot{\mathbf{x}}$ is the displacement time derivative of the cylinder.

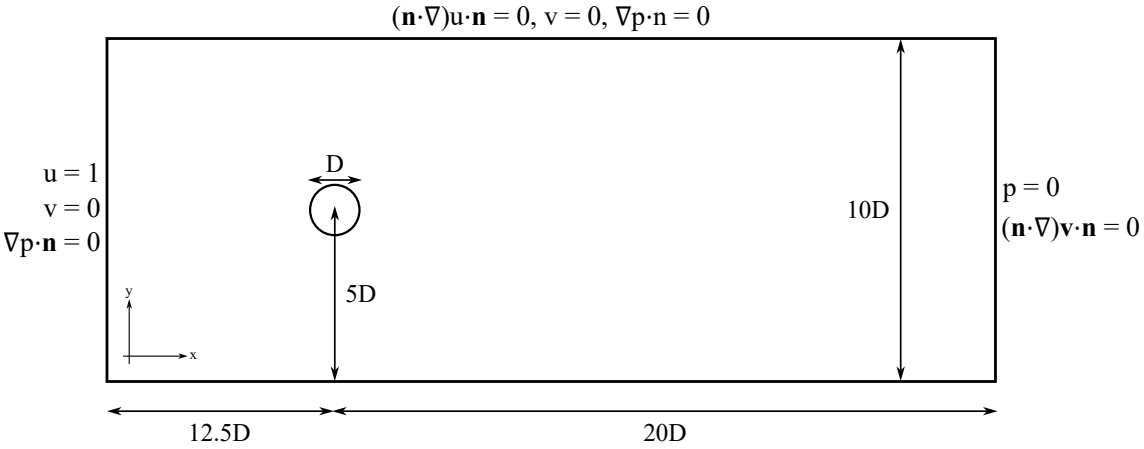

Figure 4.16: Schematics of the flow past a cylinder problem with its boundary conditions.

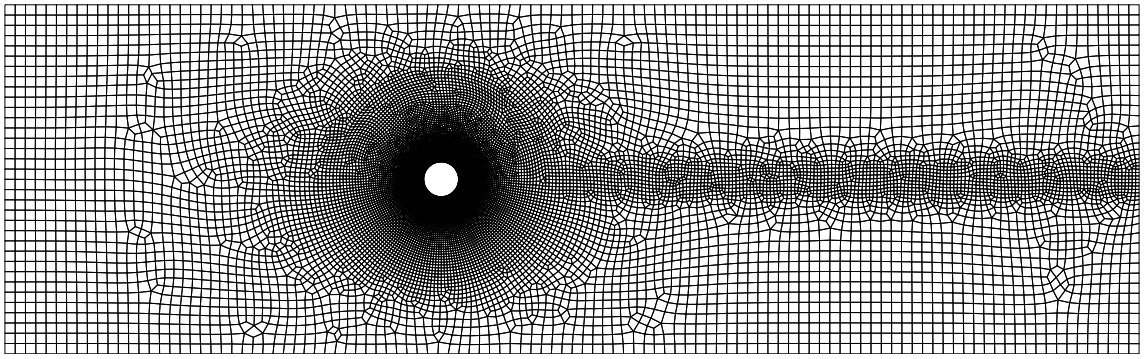

Figure 4.17: Mesh used to perform forced and free oscillation, as well as elastically mounted cylinder simulations.

Five different cases, considering cross-flow forced oscillations, were simulated. Three of them illustrate the lock-in phenomenon: $F = 0.80$, $F = 0.95$ and $F = 1.05$, while the other two present the unlocked configuration. As previously mentioned, the locked configuration is determined by analysing the PSD, lift coefficient time series and phase plots.

The unlocked configurations considered $F = 0.60$ and $F = 1.30$. Their respective results are shown in Figs. 4.18 and 4.22. It is clear that there is more than one frequency present in the time history of the lift coefficient, which is shown by the two peaks present in the PSD.

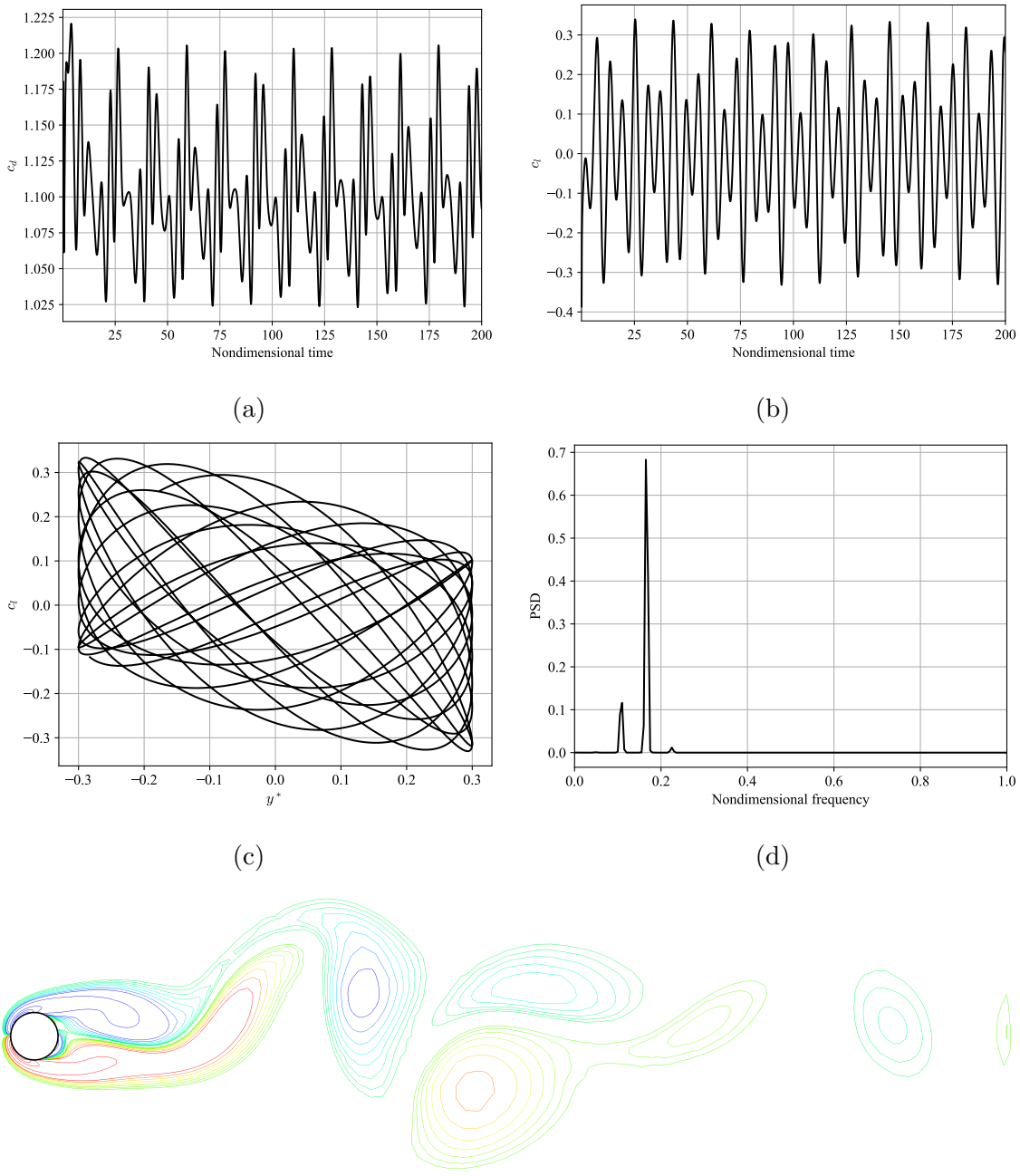

Figure 4.18: Results obtained for $A = 0.30$ and $F = 0.60$, in which (a) represents the temporal evolution of the drag coefficient, (b) temporal evolution of the lift coefficient, (c) phase diagram between the lift coefficient and the cross-flow displacement, (d) PSD and (e) vorticity contour at non-dimensional time 100.

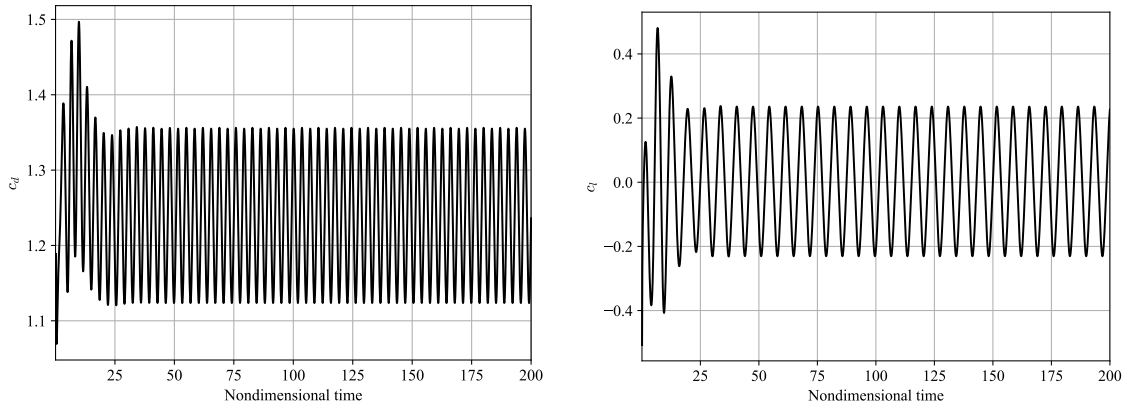

(a)

(b)

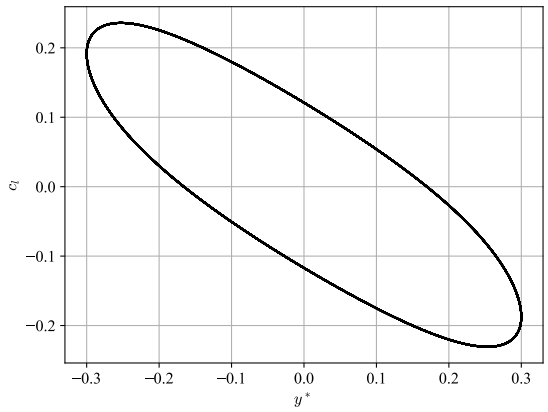

(c)

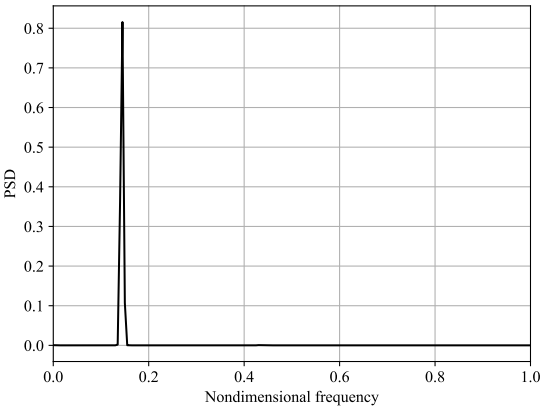

(d)

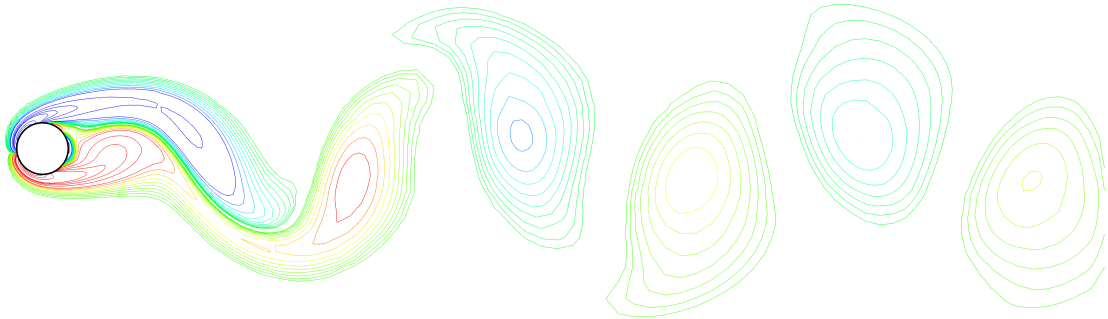

(e)

Figure 4.19: Results obtained for $A = 0.30$ and $F = 0.80$, in which (a) represents the temporal evolution of the drag coefficient, (b) temporal evolution of the lift coefficient, (c) phase diagram between the lift coefficient and the cross-flow displacement, (d) PSD and (e) vorticity contour at non-dimensional time 100.

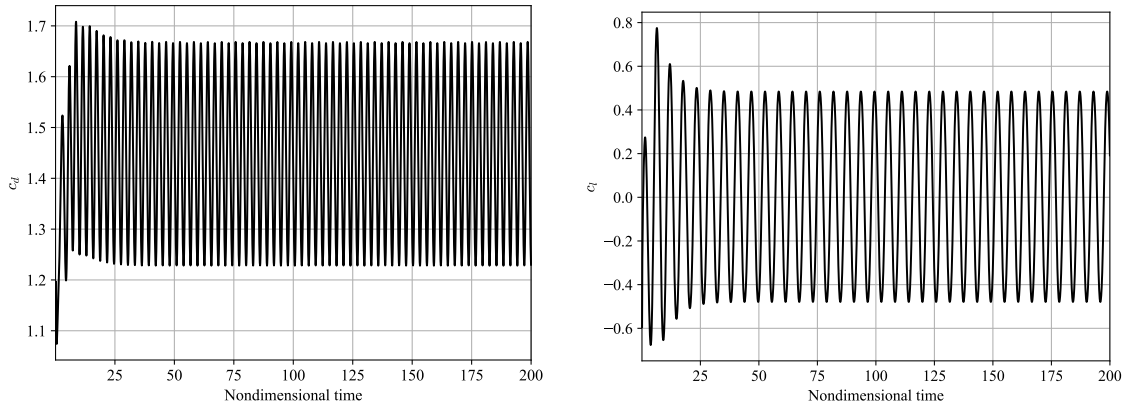

(a)

(b)

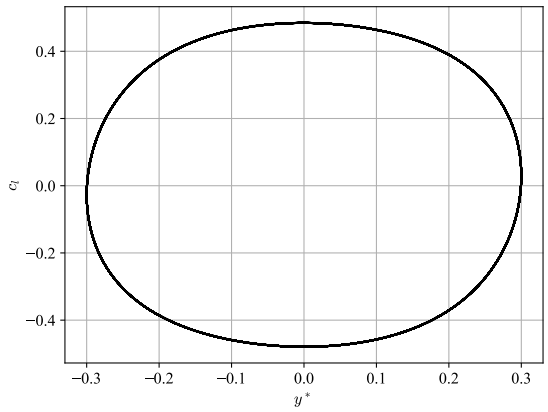

(c)

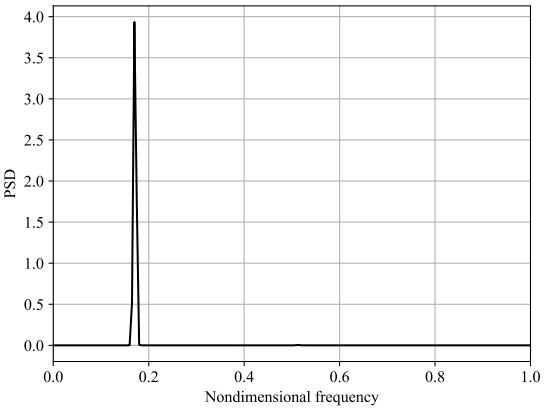

(d)

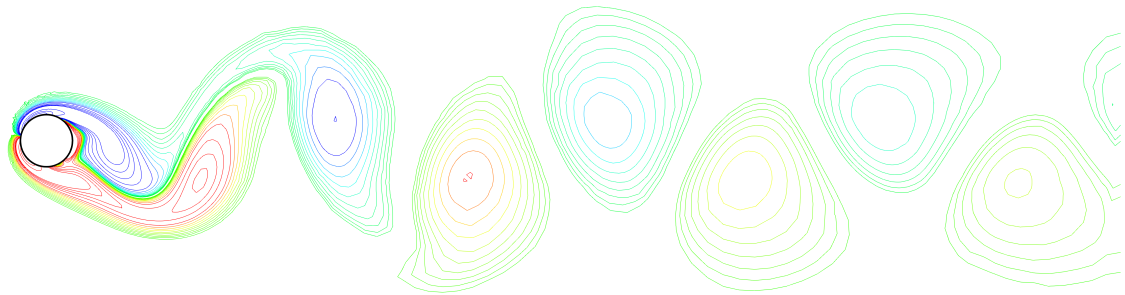

(e)

Figure 4.20: Results obtained for $A = 0.30$ and $F = 0.95$, in which (a) represents the temporal evolution of the drag coefficient, (b) temporal evolution of the lift coefficient, (c) phase diagram between the lift coefficient and the cross-flow displacement, (d) PSD and (e) vorticity contour at non-dimensional time 100.

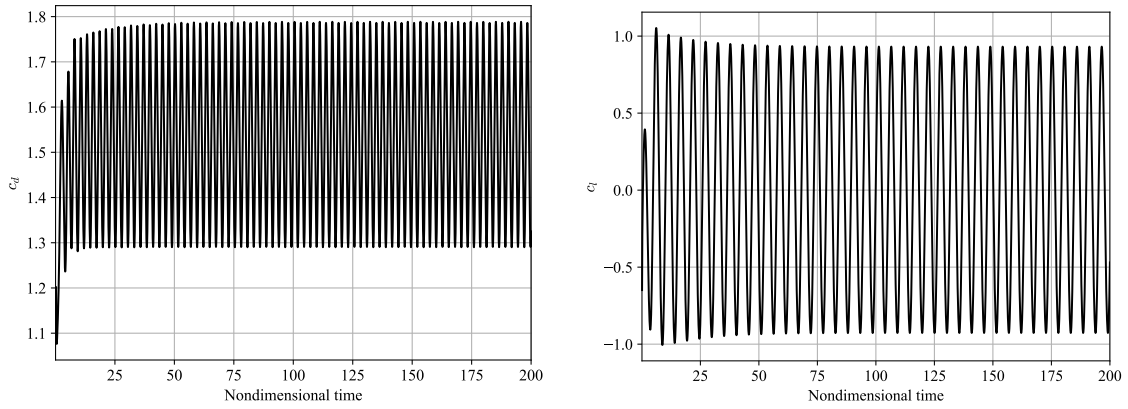

(a)

(b)

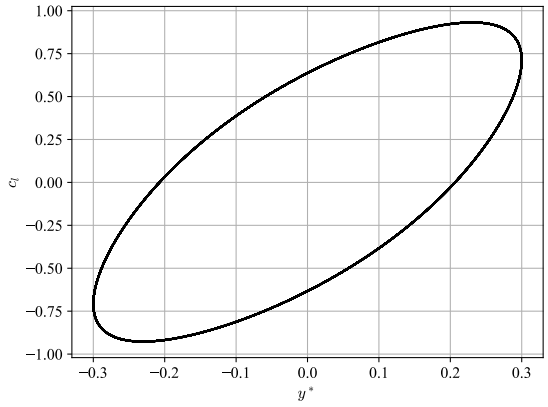

(c)

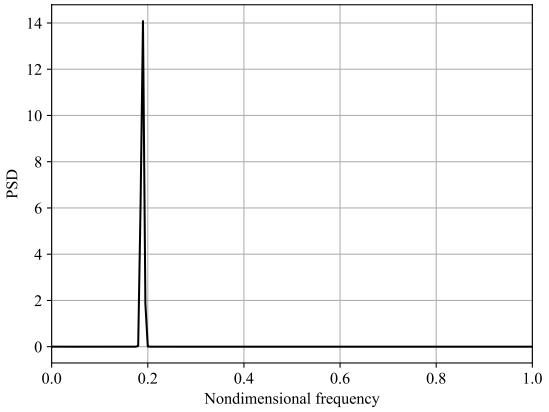

(d)

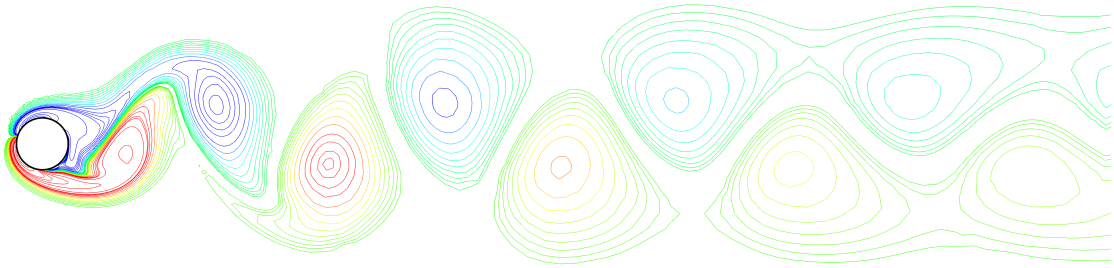

(e)

Figure 4.21: Results obtained for $A = 0.30$ and $F = 1.05$, in which (a) represents the temporal evolution of the drag coefficient, (b) temporal evolution of the lift coefficient, (c) phase diagram between the lift coefficient and the cross-flow displacement, (d) PSD and (e) vorticity contour at non-dimensional time 100.

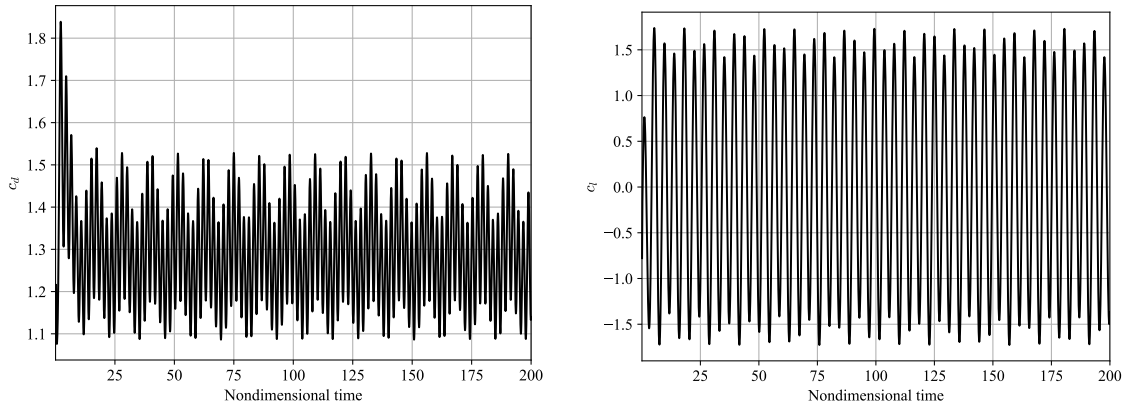

(a)

(b)

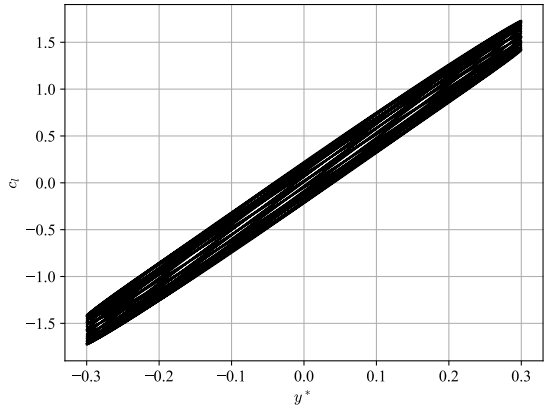

(c)

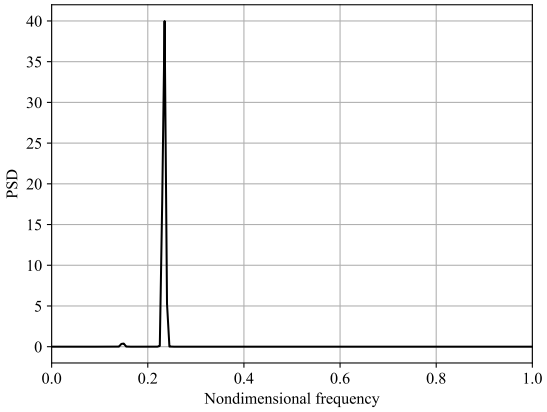

(d)

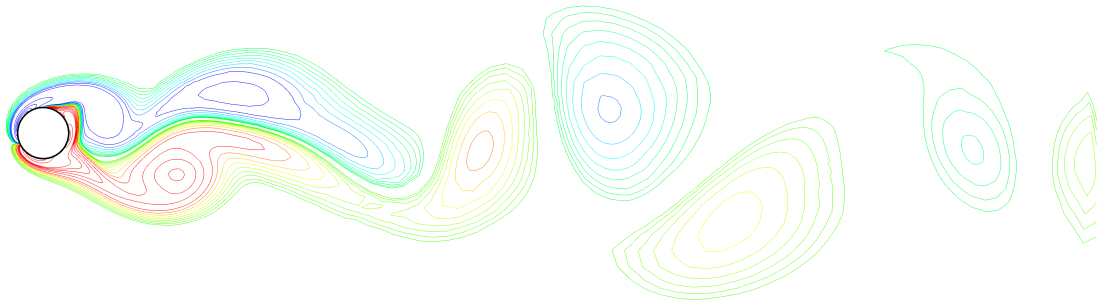

(e)

Figure 4.22: Results obtained for $A = 0.30$ and $F = 1.30$, in which (a) represents the temporal evolution of the drag coefficient, (b) temporal evolution of the lift coefficient, (c) phase diagram between the lift coefficient and the cross-flow displacement, (d) PSD and (e) vorticity contour at non-dimensional time 100.

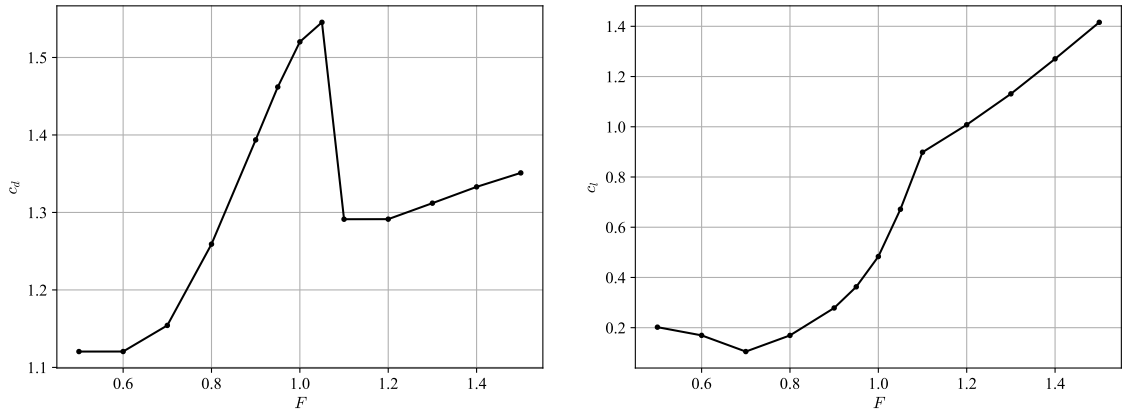

(a) (b)

Figure 4.23: Variation of the aerodynamic coefficients with the frequency ratio F, in which (a) presents the drag coefficient and (b) the lift coefficient.

Three different frequency ratios were selected to illustrate the lock-in phenomenon: $F = 0.80, 0.95$ and 1.05, their results are plotted in Figs 4.19, 4.20 and 4.21. These results dramatically differ from the previous ones, the evolution of the aerodynamic coefficients are purely sinusoidal, PSDs now appear with only one peak frequency, while the phase diagrams between the lift coefficient and the transverse displacement show only the limit cycles. The lock-in phenomenon can also be seen in the vorticity contours since the vortices are shed in a regular way due to the synchronization between cylinder motion and vortex shedding, Nobari and Naderan [22].

The behaviour of the aerodynamic coefficients follow the pattern described by Nobari and Naderan [22], Placzek *et al.* [23]. That is, the drag coefficient achieves a maximum value inside the lock-in zone and suddenly drops after, while the lift coefficient starts with an slight decrease and begins to exponentially grow at the lower boundary of the lock-in region until its upper boundary. Then the growth continues but in a linear fashion, these behaviours are shown in Fig. 4.23.

The simulations performed took about 45 hours to complete 5000 iterations using a time step of $\Delta t = 0.04$ and each iteration took around 33 seconds. The time spent per iteration in these simulations increase because as the cylinder moves, the mesh nodes coordinates also change, hence the assembly of the FEM matrices needs to be done at each iteration.

4.3.3 Free Oscillation

In this section, the cylinder's motion is governed by Newton's second law, hence it is freely moving in the fluid domain. Its non-dimensional form it is equal to:

$$\mathbf{F} = m^* \frac{\mathrm{d}\mathbf{v}_\Gamma}{\mathrm{d}t}, \tag{4.5}$$

where the derivative is treated explicitly:

$$\mathbf{F} = m^* \frac{\mathbf{v}_\Gamma^{n+1} - \mathbf{v}_\Gamma^n}{\Delta t}. \tag{4.6}$$

Hence, the cylinder's boundary has a velocity based on the calculated forces and this velocity is used to move it inside the domain with a mesh velocity proportional to the cylinder's velocity. The non-dimensional mass used in these simulations was $m^* = 5$ and the cylinder's motion is represented by Fig. 4.24.

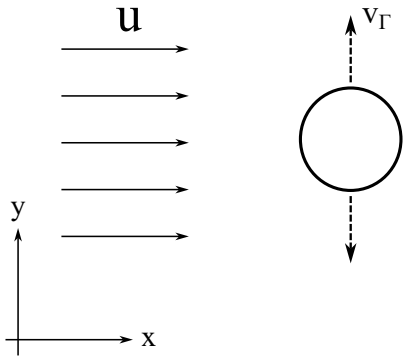

Figure 4.24: Illustration of the free oscillation problem.

The mesh shown in Fig. 4.17 was also employed to perform the current simulations. Five different scenarios were simulated for the freely moving cylinder: $Re = 100, 200, 300, 500, 1000$. In these simulations only transverse movement was considered, hence there is no movement in the horizontal direction. The total simulated time was 1000 non-dimensional time units using a 0.1 time step.

The results, shown in Fig. 4.26, illustrate the time series of the drag and lift coefficients, as well as the non-dimensional cross-flow displacement. As the Reynolds number increased, so did the aerodynamic coefficients, which was to be expected. However, when analysing the behaviour of the cylinder's oscillations it is clear that the rigid body finds a new equilibrium coordinate when it starts to feel the fluid forces. Upon reaching this new equilibrium point, y_{eq} the cylinder vibrates around it and the amplitude of this vibration also increased as the Reynolds number got

higher. The values for the aerodynamic coefficients and the y-coordinate of the new equilibrium point are presented in Tab. 4.7.

Table 4.7: Summary of the obtained results for the freely vibrating cylinder.

Re	c_d^{mean}	$c_l^{\mathbf{rms}}$	y_{eq}
100	1.14	0.19	0.09
200	1.17	0.33	0.11
300	1.20	0.41	0.10
500	1.22	0.48	0.08
1000	1.28	0.59	0.06

A freely vibrating ellipse was also considered during these simulations, the ellipse was defined with $r_x = 0.5$ and $r_y = 0.4$. The characteristic length chosen in order to determine the Reynolds number for the flow was $2r_x$ and four different Re were considered: 100, 300, 500 and 1000. The mesh used has the same geometric configuration as the mesh employed in the cylinder simulations, its details are presented in Tab. 4.9. The results are plotted in Fig. 4.27 and the behaviour of the aerodynamic coefficients is similar to that observed for the cylinder. The main difference between the ellipse and the cylinder is that the amplitude of the three analysed variables are lower for the ellipse case.

Table 4.8: Summary of the obtained results for the freely vibrating ellipse.

Re	c_d^{mean}	$c_l^{\mathbf{rms}}$	y_{eq}
100	0.78	0.09	0.03
300	0.78	0.23	0.05
500	0.78	0.28	0.06
1000	0.79	0.33	0.03

Finally, tandem cylinders were also simulated under this scenario at $Re = 100$. The geometry used for this case is seen in Fig. 4.25. From the calculated results, it is clear that the cylinder in the wake of the first one suffers higher amplitude oscillations due to the fact that the lift coefficient amplitude is also larger, while the mean drag coefficient is lower in spite of the fact that its oscillation amplitude is

higher, see Fig. 4.28. Quantitatively, the $c_{d,\,\text{mean}}^{\Gamma_1} = 1.07$ while $c_{d,\,\text{mean}}^{\Gamma_2} = 0.62$ and the $c_{l,\,\mathbf{rms}}^{\Gamma_i}$ jumps from 0.21 to 0.78, which is a significant difference. The new equilibrium coordinates for the cylinders are almost the same, $y_{\text{eq}}^{\Gamma_1} = 0.188$ and $y_{\text{eq}}^{\Gamma_2} = 0.187$.

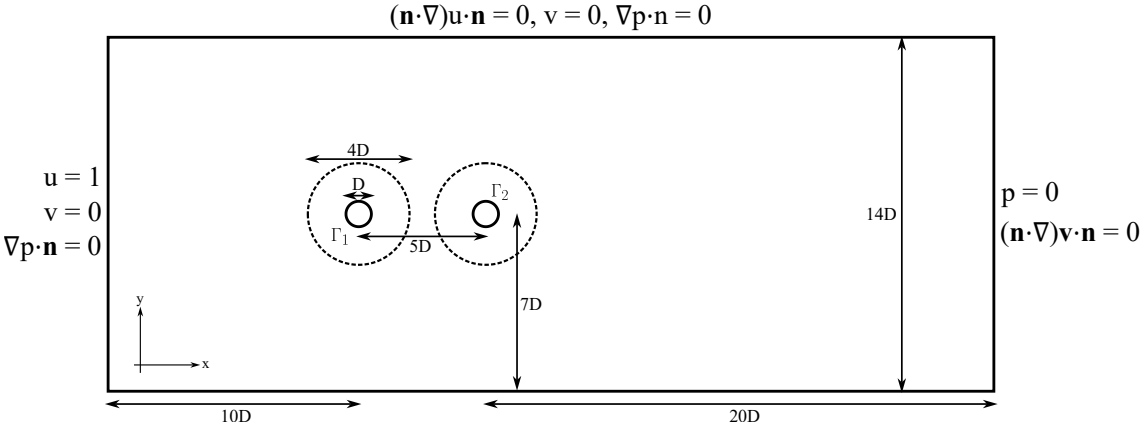

Figure 4.25: Mesh geometry employed for the tandem cylinders with boundary conditions.

Table 4.9: Mesh details for the ellipse and tandem cylinders geometries.

Mesh	No. Elements	No. Nodes
Ellipse	24327	49014
Tandem	33371	67343

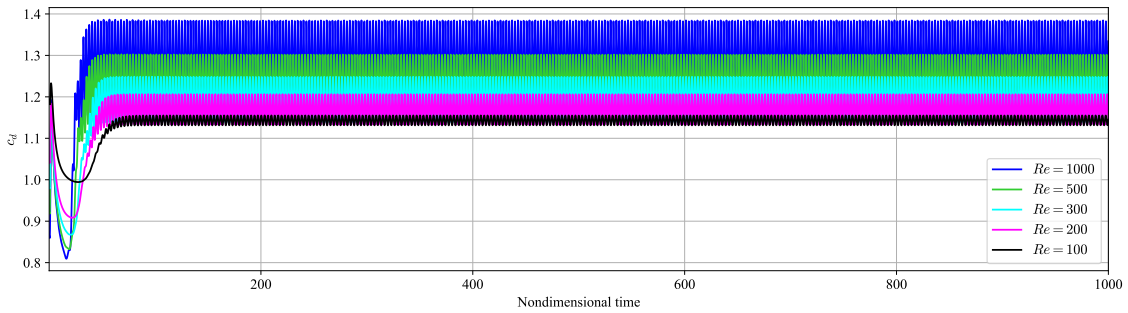

(a)

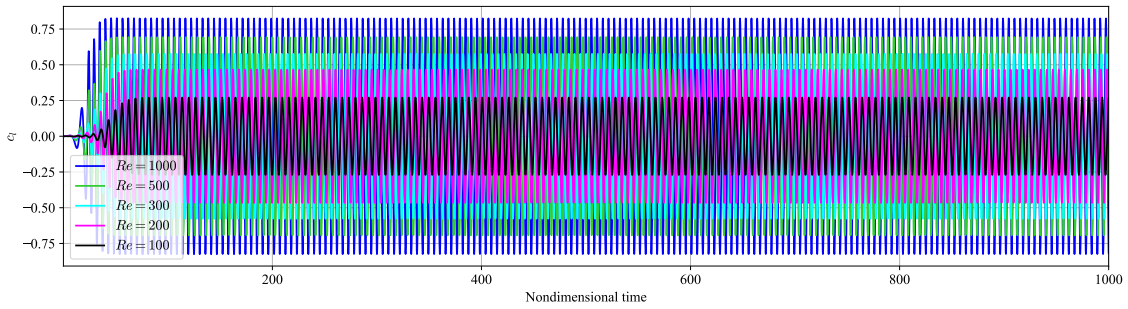

(b)

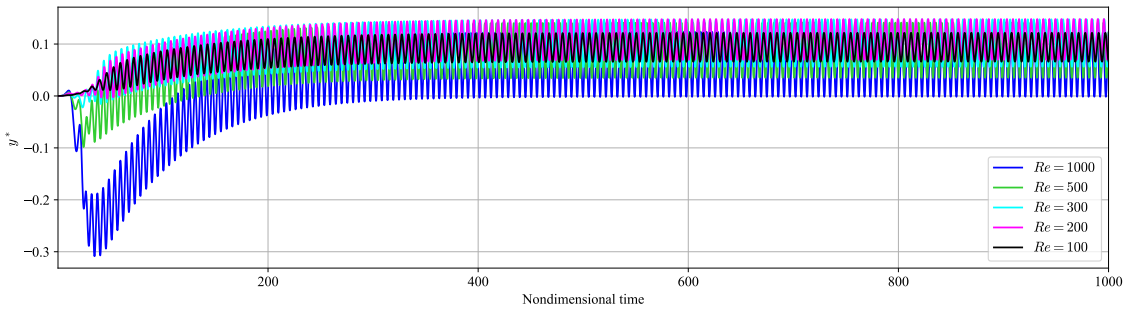

(c)

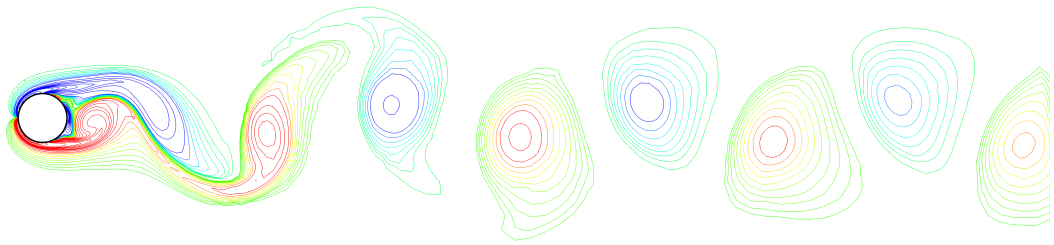

(d)

Figure 4.26: Comparison between the results obtained for the freely vibrating cylinder under different Reynolds numbers. (a) Drag coefficient; (b) lift coefficient; (c) y^* displacement; (d) vorticity field at non-dimensional time 996.5 for the $Re = 300$ case.

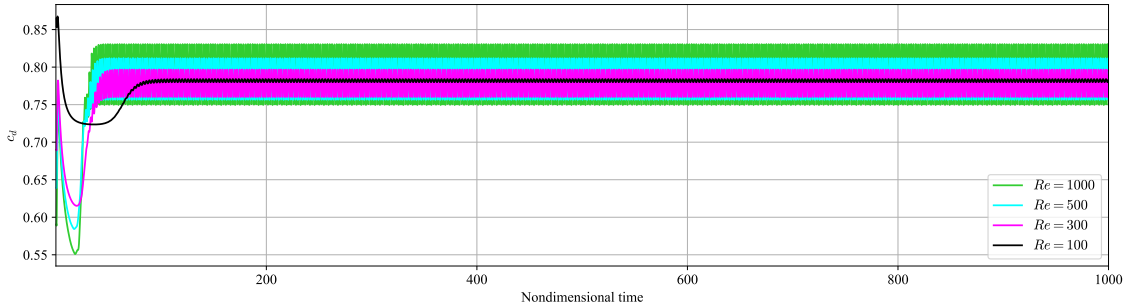

(a)

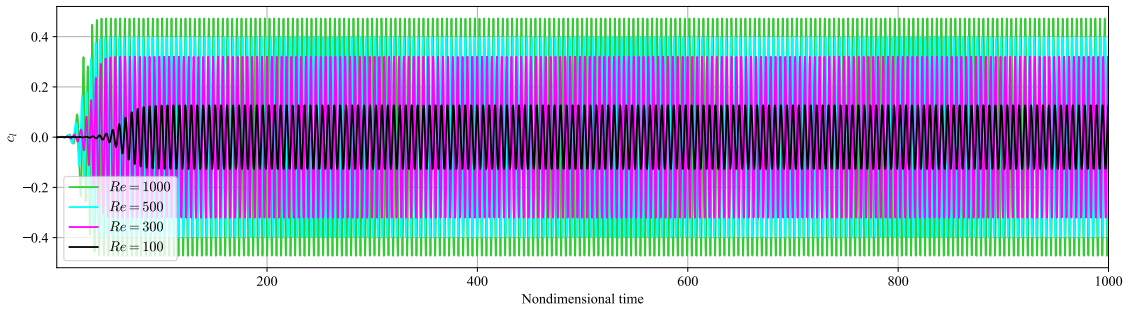

(b)

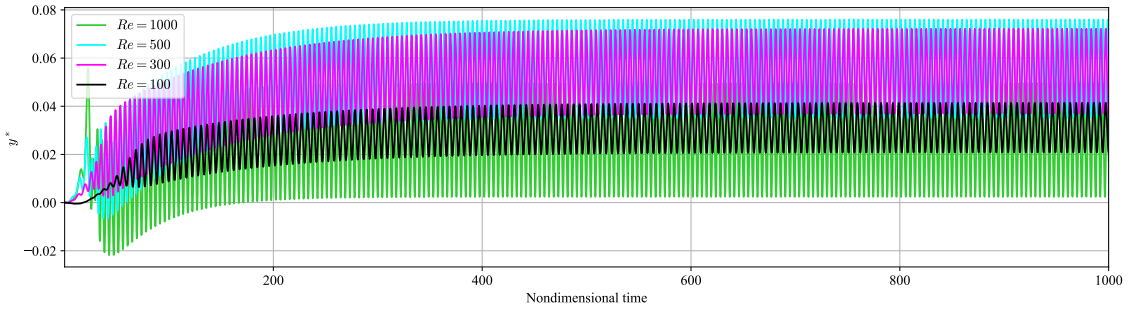

(c)

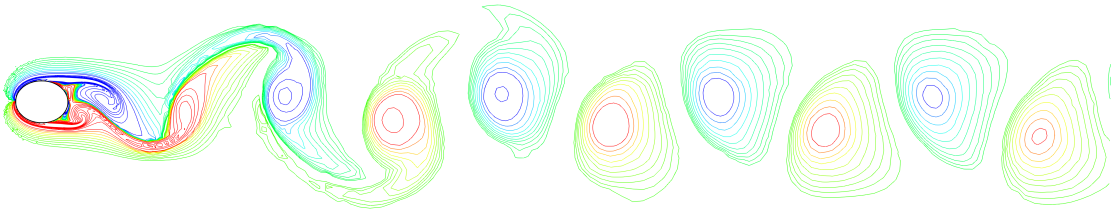

(d)

Figure 4.27: Comparison between the results obtained for the freely vibrating ellipse under different Reynolds numbers. (a) Drag coefficient; (b) lift coefficient; (c) y^* displacement; (d) vorticity field for $Re = 1000$.

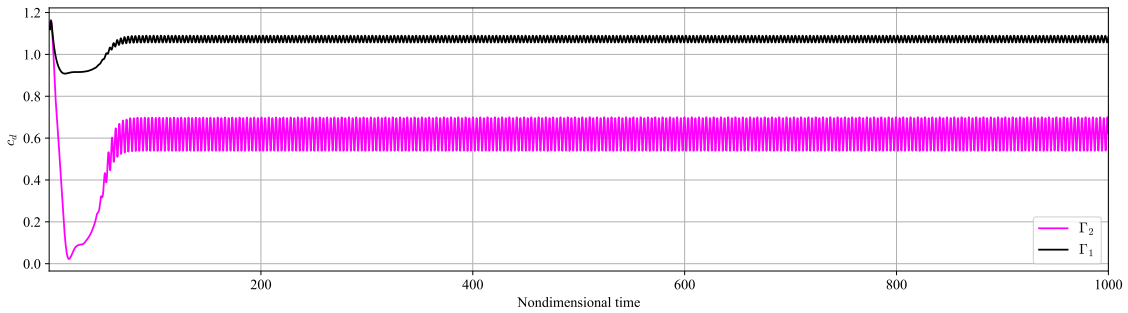

(a)

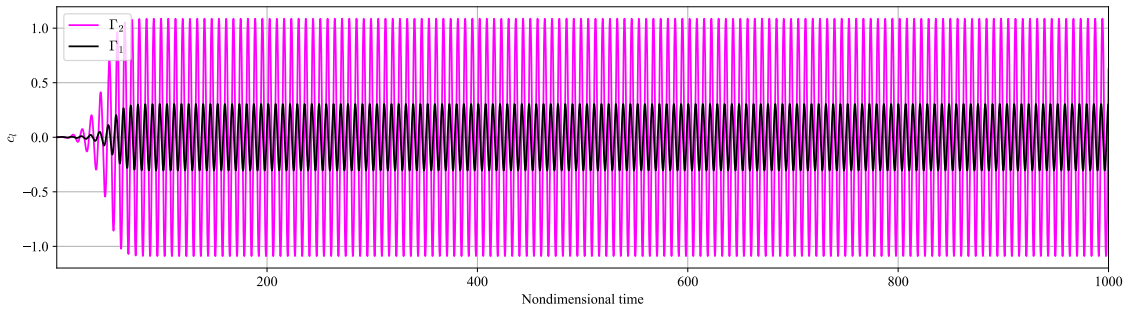

(b)

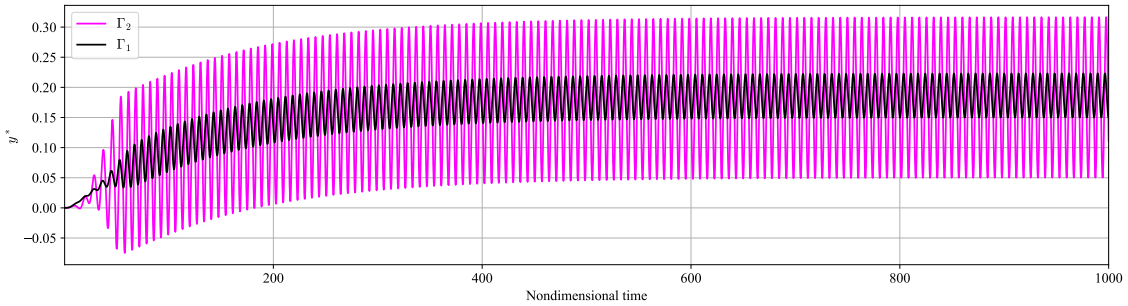

(c)

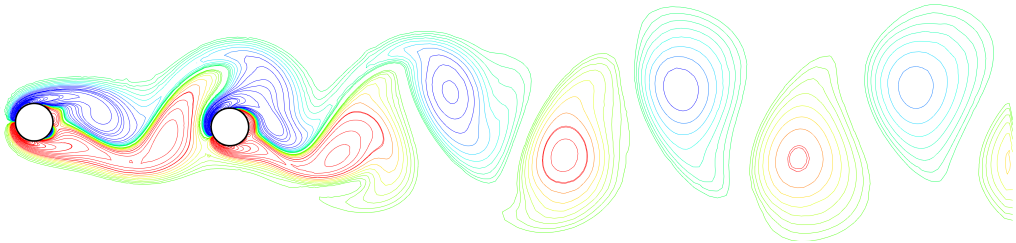

(d)

Figure 4.28: Comparison between the results obtained for the freely vibrating tandem cylinders, Γ_1 represents the cylinder in front, while Γ_2, the one behind it. (a) Drag coefficient; (b) lift coefficient; (c) y^* displacement; (d) vorticity field for $Re = 100$.

4.3.4 Elastically Mounted

In this section, the cylinder's motion is governed by a second order differential equation from Prasanth and Mittal [9], while Fig. 4.29 illustrates the problem.

$$\begin{bmatrix} \ddot{x} \\ \ddot{y} \end{bmatrix} + 4\pi\zeta F_n \begin{bmatrix} \dot{x} \\ \dot{y} \end{bmatrix} + (2\pi F_n)^2 \begin{bmatrix} x \\ y \end{bmatrix} = \frac{2}{\pi m^*} \begin{bmatrix} c_d \\ c_l \end{bmatrix}, \tag{4.7}$$

in which x and y are the displacements, ζ is the damping ratio, F_n is the reduced natural frequency, m^* is a non-dimensional mass, c_d and c_l are the drag and lift coefficients, computed by Eqs. (3.104) and (3.105). The non-dimensional mass is defined as:

$$m^* = \frac{4m}{\pi\rho D^2}, \tag{4.8}$$

while the reduced natural frequency, which is related to the reduced velocity is equal to:

$$U^* = \frac{U}{f_n D} = \frac{1}{F_n}. \tag{4.9}$$

Nevertheless, the current simulations use $m^* = 10$, $F_n = 16.6/Re$ and $\zeta = 0$, therefore the reduced velocity varies with the Reynolds number.

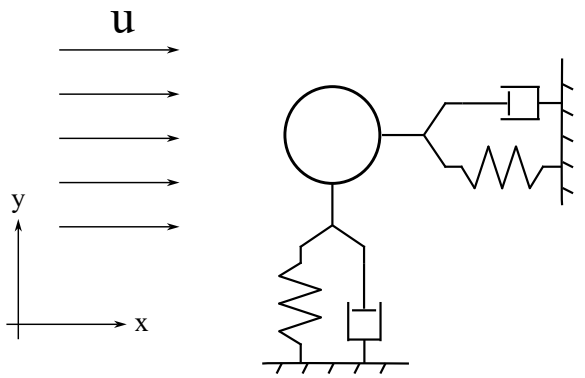

Figure 4.29: Illustration of the elastically supported cylinder.

The equation of motion is solved by an explicit scheme, described below:

$$\mathbf{y}^{n+1} = \mathbf{y}^n + \dot{\mathbf{y}}^n \Delta t + \frac{1}{2}\ddot{\mathbf{y}}^n \Delta t^2, \tag{4.10}$$

$$\dot{\mathbf{y}}^{n+1} = \dot{\mathbf{y}}^n + \ddot{\mathbf{y}}^n \Delta t, \tag{4.11}$$

where $\ddot{\mathbf{y}}^n$ is given by:

$$\ddot{\mathbf{y}}^n = \frac{2c_{d,l}}{\pi m^*} - 4\pi\zeta F_n \dot{\mathbf{y}}^n - (2\pi F_n)^2 \mathbf{y}^n. \tag{4.12}$$

It is important to notice that the boundary velocity, $\mathbf{v}_\Gamma = \dot{\mathbf{y}}^{\mathbf{n+1}}$.

Simulations were performed varying the Reynolds number from 60 to 180 (or $3.61 \leq U^* \leq 10.87$) and the maximum transverse oscillation amplitude for each Re is plotted in Fig. 4.30. Differently from the other sections, here the cylinder has two degrees of freedom, therefore in-line and cross-flow oscillations are present in the current scenario. Three different Reynolds numbers were chosen arbitrarily to illustrate the results obtained with this analysis: $Re = 75$, 88 and 100. The aerodynamic coefficients, orbit and vorticity contour are presented in Figs. 4.32, 4.33 and 4.34. It is important to notice that the orbit graphs were plotted using only the values of displacement at the last 40 non-dimensional time units.

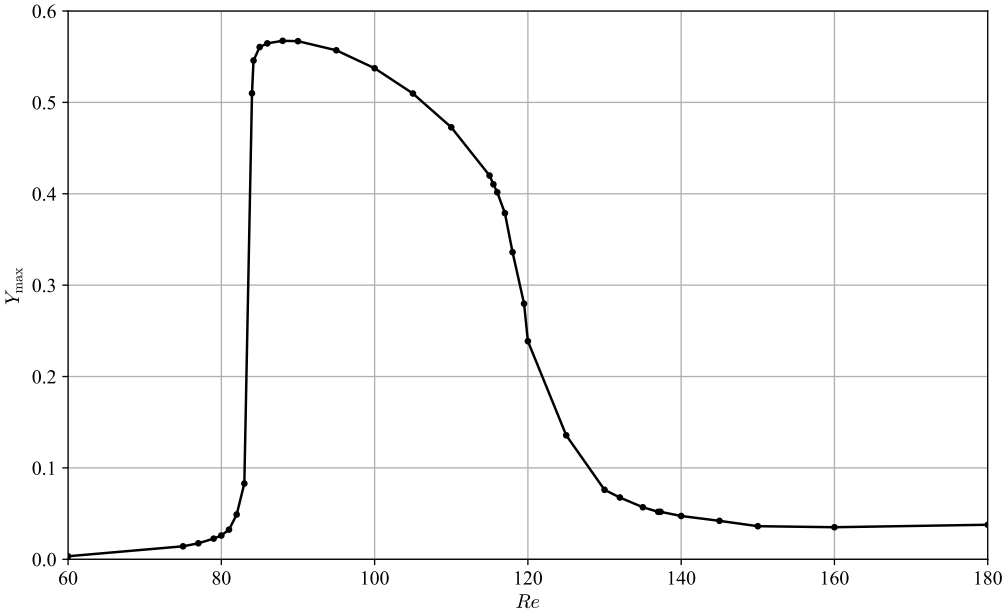

Figure 4.30: Variation of maximum cross-flow oscillation amplitude with Re.

The obtained results are in agreement with the one presented by Prasanth and Mittal [9], especially when comparing the behaviour of the maximum transverse amplitude versus Re. An analysis of Fig. 4.30 clearly indicates the presence of a lock-in region, which starts around $Re \approx 80$ and ends at $Re \approx 130$. The maximum amplitude of transverse vibration was nearly $0.6D$ at $Re = 88$.

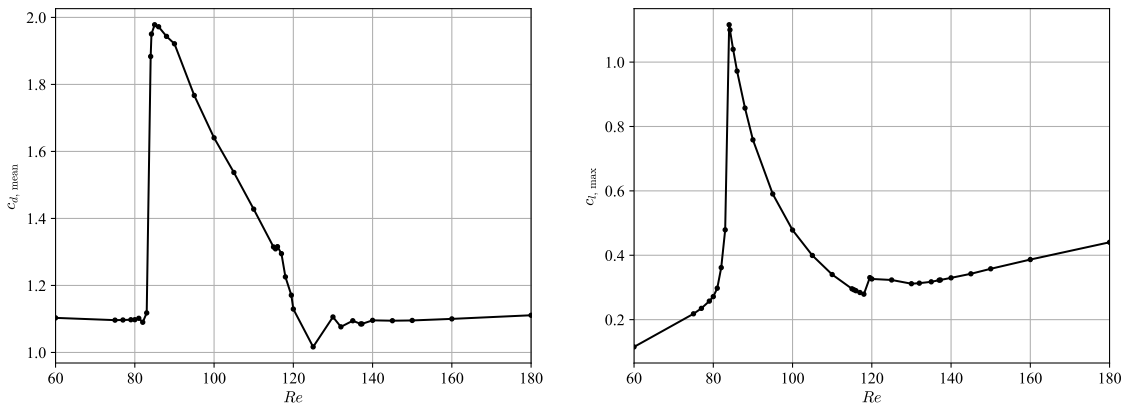

(a) (b)

Figure 4.31: Variation of the drag and lift coefficients as a function of Re, in which (a) presents the mean drag coefficient while (b) shows the max lift value.

Figure 4.31 presents the behaviour of the aerodynamic coefficients as a function of the Reynolds number. As previously seen on the forced oscillation section, the drag coefficient achieves a maximum value inside the lock-in zone and the decreases as Re grows. While the lift coefficient sharply grows at the lower boundary of the synchronization region and decays up to the upper limit of the lock-in zone. Then it starts to linearly grow until the last simulated Re.

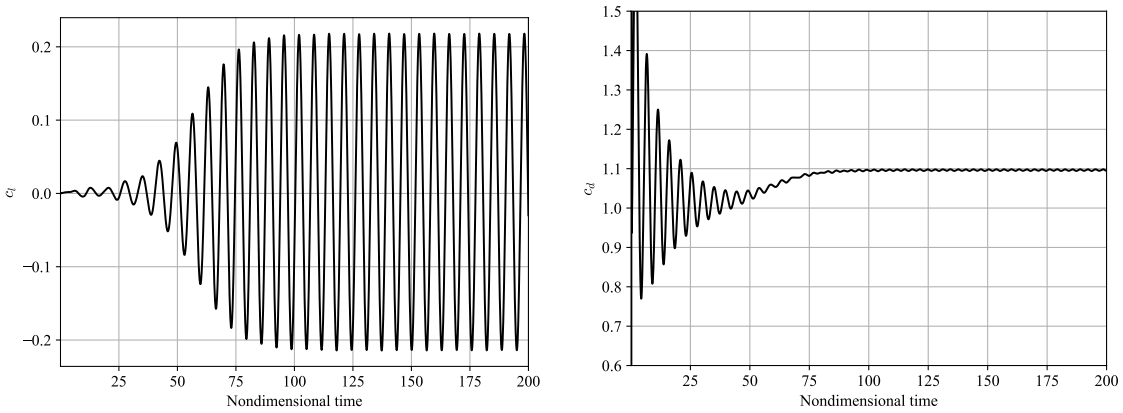

(a)

(b)

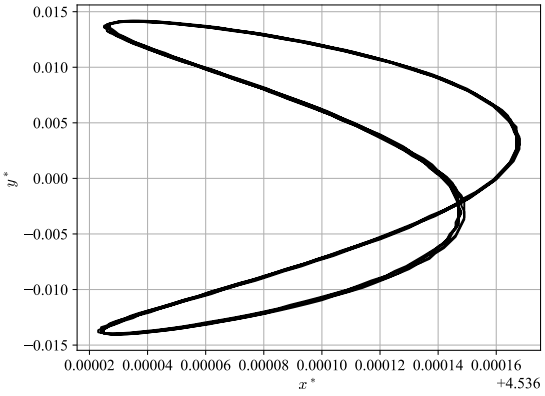

(c)

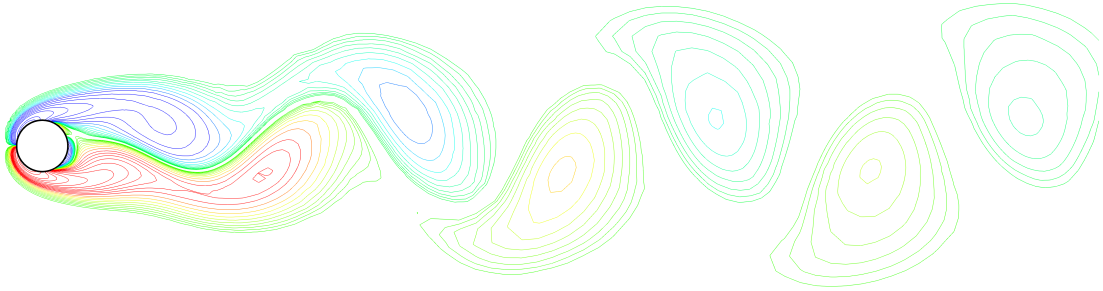

(d)

Figure 4.32: Results obtained for the elastically mounted cylinder at $Re = 75$. (a) Time history of the lift coefficient; (b) time history of the drag coefficient; (c) cylinder orbit; (d) vorticity contour at non-dimensional time 150.

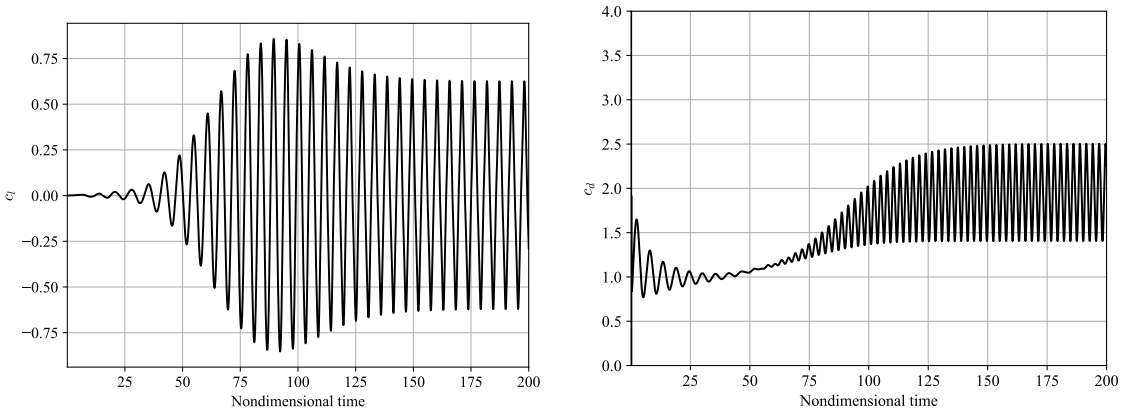

(a)

(b)

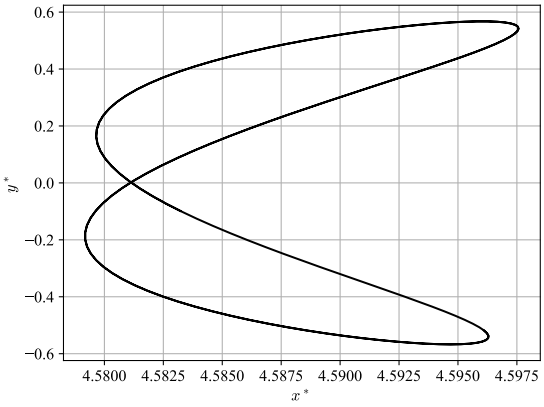

(c)

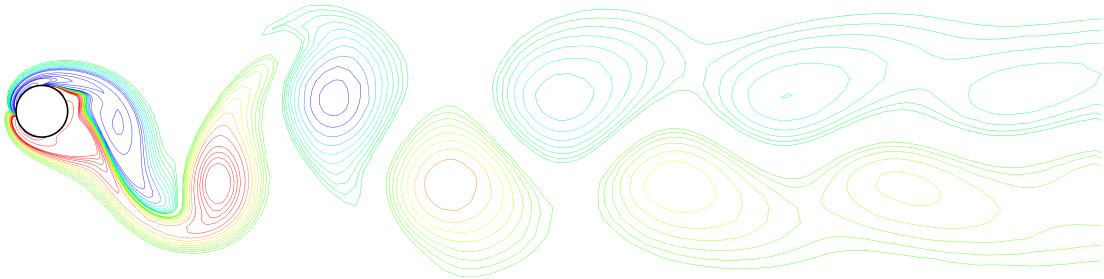

(d)

Figure 4.33: Results obtained for the elastically mounted cylinder at $Re = 88$. (a) Time history of the lift coefficient; (b) time history of the drag coefficient; (c) cylinder orbit; (d) vorticity contour at non-dimensional time 150.

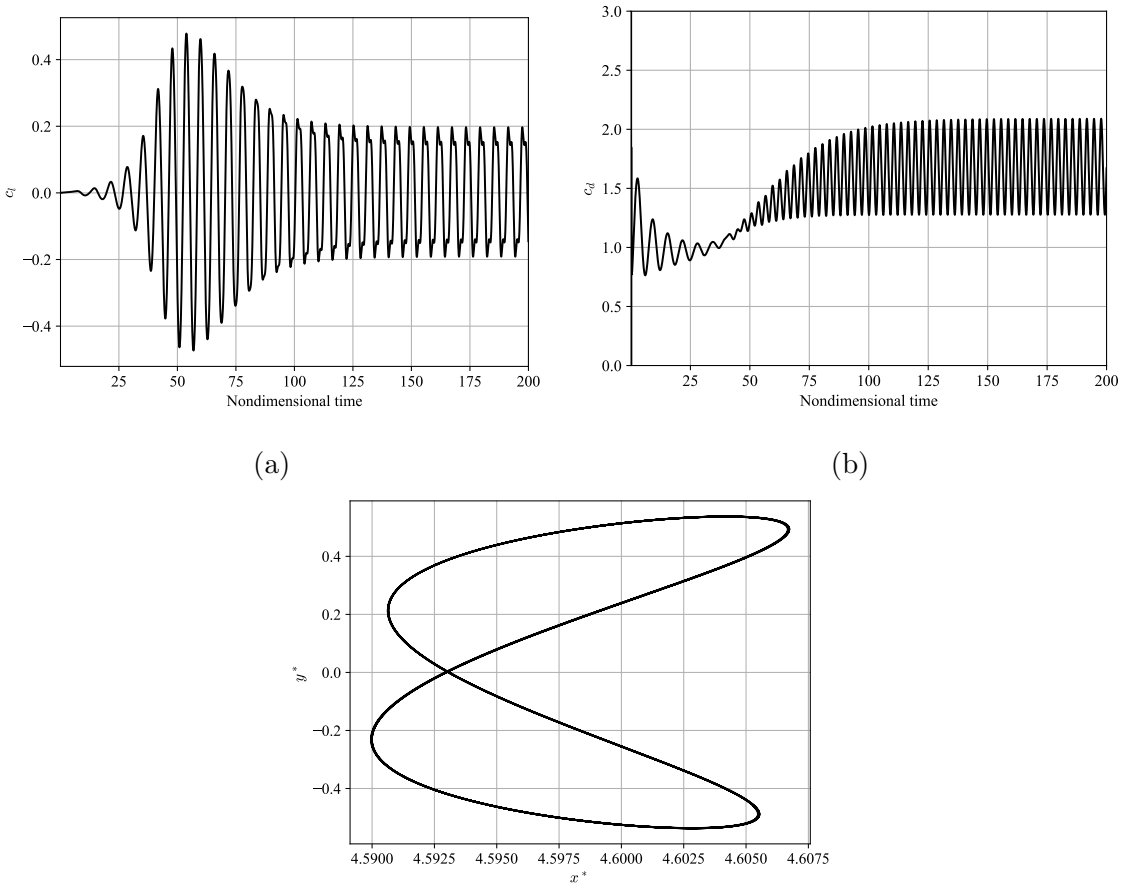

(a) (b)

(c)

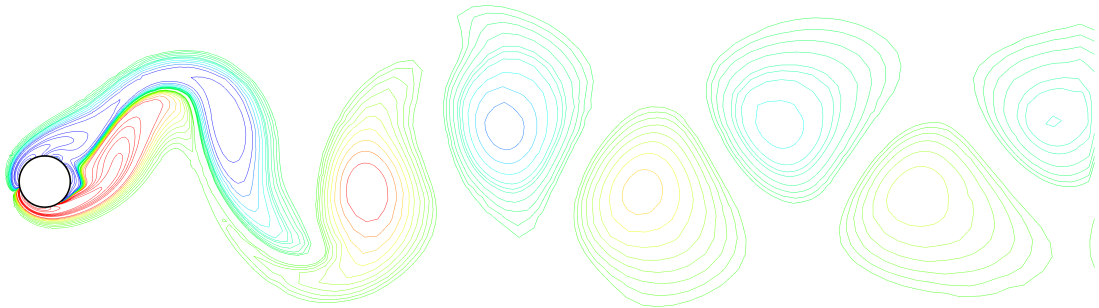

(d)

Figure 4.34: Results obtained for the elastically mounted cylinder at $Re = 100$. (a) Time history of the lift coefficient; (b) time history of the drag coefficient; (c) cylinder orbit; (d) vorticity contour at non-dimensional time 150.

4.4 Flow Past a Square

The flow past an elastically supported square was also considered. The dynamics of the rigid body is governed by the same equation as in the cylinder case, Eq. (4.7). However, the structural parameters considered for this simulation were different and include a small damping ratio, all simulation parameters are displayed in Tab. 4.10. It is important to notice that the reduced velocity is related to the reduced natural frequency through Eq. (4.9).

Table 4.10: Simulation parameters for the flow past an elastically mounted square.

m^*	U^*	ζ	Re	Δt
20	7	0.0037	250	0.04

The mesh geometry used is similar to the one previously shown in Fig. 4.16. The square is defined with an edge size equal to 1, such that its characteristic length is also 1. The mesh used to perform the simulation had 18917 quadrilateral elements and 38153 nodes.

The equations of motion of the elastically mounted square are similar to Eq. (4.7), except for the right hand side, which is now given by $c_i/2m^*$. As the displaced fluid volume per unit length of an object with a rectangular cross-section is ρDL, while one with a circular cross-section is $\rho\pi D^2/4$.

The obtained results are seen in Fig. 4.35. The **rms** value of the fluctuating lift coefficient is $c_l^{\mathbf{rms}} = 0.29$, while the mean drag coefficient is $c_d^{\text{mean}} = 1.69$ and the Strouhal number is equal to 0.165. The amplitude of vibration is larger in the transverse direction than the horizontal one.

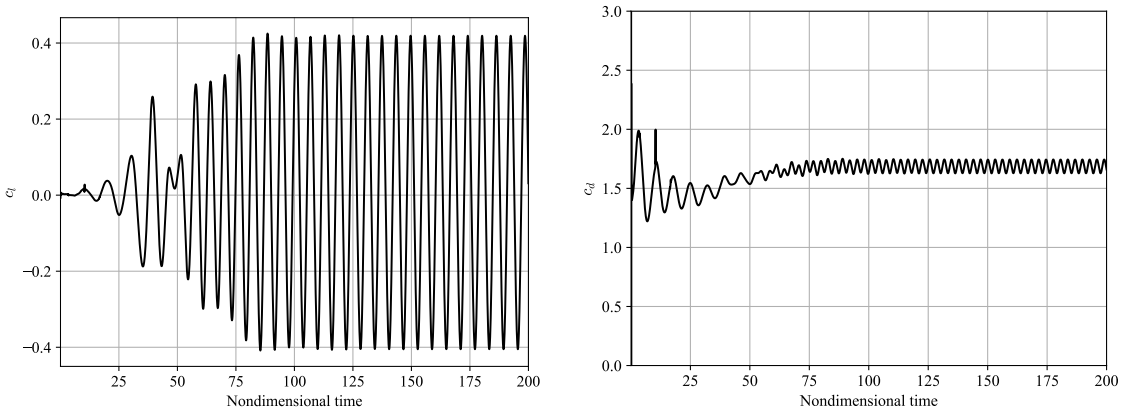

(a)

(b)

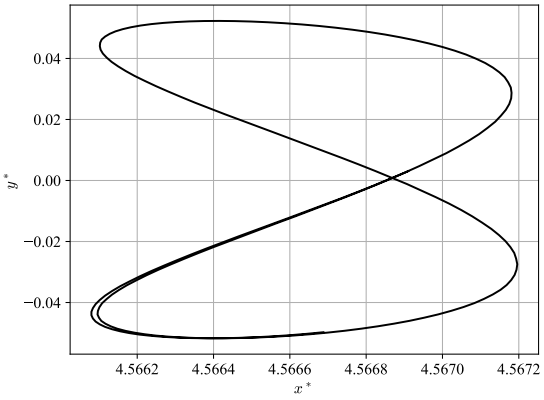

(c)

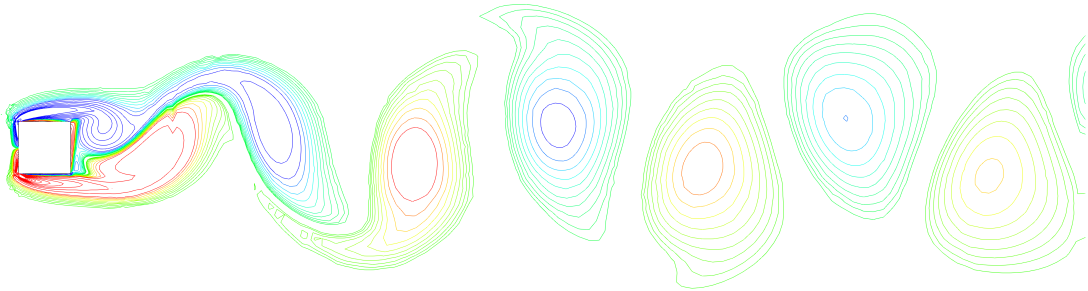

(d)

Figure 4.35: Results obtained for the elastically mounted square at $Re = 250$. (a) Time history of the lift coefficient; (b) time history of the drag coefficient; (c) cylinder orbit; (d) vorticity contour at an arbitrary non-dimensional time.

Chapter 5

Conclusion and Suggestions

The current work proposes a coupled FEM-ALE methodology to simulate fluid-structure interaction phenomenon, which demonstrated satisfactory results when compared to the available literature on vortex-induced vibrations. The chapter then ends with a few suggestions on the possible future developments in order to improve the methodology, particularly in terms of performance and accuracy.

5.1 Conclusion

This work presents a complete methodology to simulate the fluid-structure interaction between a rigid body and an incompressible fluid. The finite element method is used to discretize the Navier Stokes equations, which are written in an arbitrary Lagrangian-Eulerian framework, thus allowing the mesh nodes to move. The coupling between FEM and ALE methods provides an accurate description of a moving boundary inside the fluid domain, which is essential to properly study vortex-induced vibrations.

In order to stabilize the numerical scheme for higher Reynolds numbers, a semi-Lagrangian method is also employed to discretize the material derivative in the Navier-Stokes equations. The utilization of this stabilizing technique requires an efficient search-interpolation procedure to evaluate the variable of interest at the departure point, which was also implemented into the methodology herein described.

Different benchmark simulations were performed, which yielded satisfactory results when compared to analytical solutions or the available literature. Despite a

slight underestimation of the aerodynamic coefficients, which were attributed to the type of finite element employed, the proposed methodology adequately captures the intricate dynamics of a system subjected to fluid-structure interactions due to the FEM-ALE coupling. As demonstrated by the computed results for forced oscillations in the transverse direction as well as the results obtained for the two degree of freedom elastically mounted cylinder.

In summary, the proposed methodology has proven it can properly simulate vortex-induced vibrations in spite of its main drawback: underestimation of the aerodynamic coefficients. The author does not exclude the possibility of an implementation error that can be attributed as the cause of the main drawback. However, to investigate this further a new finite element must be employed first.

5.2 Future Work

During the development of the proposed methodology multiple difficulties were tackled. While some were successfully overcome, others were only bypassed. Notwithstanding these difficulties, the author is satisfied with the developed work. However, it is also clear that multiple changes can be made to improve the performance and mainly the accuracy of the proposed method. The author believes future work should tackle the following topics:

- Higher-order shape functions: improves accuracy and will allow the development of an explanation as to why the current methodology underestimates the aerodynamic coefficients.

- Higher-order semi-Lagrangian schemes: improves accuracy and reduces numerical diffusion.

- Laplacian smoothing: this technique improves mesh quality by repositioning the nodes in order to satisfy a certain element aspect ratio.

- Matrix assembly process: currently all element matrices are reassembled at each iteration when mesh movement is present, in spite of the fact that only a small region requires this reassembly process, which is one of the most time consuming steps in the proposed algorithm.

- Elastically supported under different structural parameters.

Bibliography

[1] Kaneko, S., Nakamura, T., Inada, F., et al. (Eds.). *Flow-Induced Vibrations*. Elsevier, 2014.

[2] Lienhard, J. H. "Synopsis of lift, drag, and vortex frequency data for rigid circular cylinders". 1966.

[3] Williamson, C., Roshko, A. "Vortex formation in the wake of an oscillating cylinder", *Journal of Fluids and Structures*, v. 2, pp. 355–381, 7 1988.

[4] Khalak, A., Williamson, C. "Dynamics of a hydroelastic cylinder with very low mass and damping", *Journal of Fluids and Structures*, v. 10, pp. 455–472, 7 1996.

[5] Feng, C. "The measurement of vortex induced effects in flow past stationary and oscillating circular and D-section cylinders". 1968.

[6] Huyakorn, P., Taylor, C., Lee, R., et al. "A comparison of various mixed-interpolation finite elements in the velocity-pressure formulation of the Navier-Stokes equations", *Computers & Fluids*, v. 6, pp. 25–35, 3 1978.

[7] Zienkiewicz, O. C., Taylor, R. L., Nithiarasu, P. *The Finite Element Method for Fluid Dynamics*. Elsevier, 2014.

[8] Koopmann, G. H. "The vortex wakes of vibrating cylinders at low Reynolds numbers", *Journal of Fluid Mechanics*, v. 28, pp. 501–512, 5 1967.

[9] Prasanth, T. K., Mittal, S. "Vortex-induced vibrations of a circular cylinder at low Reynolds numbers", *Journal of Fluid Mechanics*, v. 594, pp. 463–491, 1 2008.

[10] Chandrasekaran, S. *Design of Marine Risers with Functionally Graded Materials*. Elsevier, 2021.

[11] Vandiver, J. K. "Drag Coefficients of Long Flexible Cylinders". 1983.

[12] Williamson, C., Govardhan, R. "Vortex-Induced Vibrations", *Annual Review of Fluid Mechanics*, v. 36, pp. 413–455, 1 2004.

[13] Strouhal, V. "Ueber eine besondere Art der Tonerregung", *Annalen der Physik*, 1878.

[14] Kármán, T. "On the mechanism of the drag a moving body experiences in a fluid", *Progress in Aerospace Sciences*, v. 59, pp. 13–15, 5 2013.

[15] Bishop, R., Hassan, A. "The lift and drag forces on a circular cylinder oscillating in a flowing fluid", *Proceedings of the Royal Society of London. Series A. Mathematical and Physical Sciences*, v. 277, pp. 51–75, 1 1964.

[16] Blevins, R. "Flow Induced Vibration of Bluff Structures". 1974.

[17] Blackburn, H. M., Karniadakis, G. "Two and Three-Dimensional Simulations of Vortex-Induced Vibration of a Circular Cylinder". 1993.

[18] Newman, D., Karniadakis, G. "Direct numerical simulations of flow over a flexible cable". 1995.

[19] Mittal, S., Kumar, V. "Finite element study of vortex-induced cross-flow and in-line oscillations of a circular cylinder at low reynolds numbers", *International Journal for Numerical Methods in Fluids*, v. 31, pp. 1087–1120, 1999.

[20] Singh, S., Mittal, S. "Vortex-induced oscillations at low Reynolds numbers: Hysteresis and vortex-shedding modes", *Journal of Fluids and Structures*, v. 20, pp. 1085–1104, 11 2005.

[21] Shiels, D., Leonard, A., Roshko, A. "Flow-induced vibration of a circular cylinder at limiting structural parameters", *Journal of Fluids and Structures*, v. 15, pp. 3–21, 1 2001.

[22] Nobari, M., Naderan, H. "A numerical study of flow past a cylinder with cross flow and inline oscillation", *Computers & Fluids*, v. 35, pp. 393–415, 5 2006.

[23] Placzek, A., Sigrist, J.-F., Hamdouni, A. "Numerical simulation of an oscillating cylinder in a cross-flow at low Reynolds number: Forced and free oscillations", *Computers & Fluids*, v. 38, pp. 80–100, 1 2009.

[24] Tamura, Y. "Mathematical models for understanding phenomena: Vortex-induced vibrations", *Japan Architectural Review*, v. 3, pp. 398–422, 10 2020.

[25] Wu, Y., Cheng, Z., McConkey, R., et al. "Modelling of Flow-Induced Vibration of Bluff Bodies: A Comprehensive Survey and Future Prospects", *Energies*, v. 15, pp. 8719, 11 2022.

[26] Huera-Huarte, F. "Vortex-Induced Vibration of Flexible Cylinders in Cross-Flow", *Annual Review of Fluid Mechanics*, v. 57, pp. 285–310, 1 2025.

[27] Clough, R. W. "The finite element method in plane stress analysis", 1960.

[28] Hughes, T. R. *The Finite Element Method: Linear Static and Dynamic Finite Element Analysis*. Dover, 2000.

[29] Zienkiewicz, O. C., Taylor, R. L., Fox, D. *The Finite Element Method for Solid and Structural Mechanics*. Elsevier, 2014.

[30] Bathe, K.-J. *Finite Element Procedures*. Prentice Hall, 2014.

[31] Zienkiewicz, O. C., Cheung, Y. K. "Finite elements in the solution of field problems", 1965.

[32] Ladyzhenskaya, O. A. *The Mathematical Theory of Viscous Incompressible Flow*. Gordon and Breach, 1963.

[33] Babuška, I. "The finite element method with Lagrangian multipliers", *Numerische Mathematik*, v. 20, pp. 179–192, 6 1973.

[34] Brezzi, F. "On the existence, uniqueness and approximation of saddle-point problems arising from lagrangian multipliers", *Revue française d'automatique, informatique, recherche opérationnelle. Analyse numérique*, v. 8, pp. 129–151, 5 1974.

[35] Taylor, C., Hood, P. "A numerical solution of the Navier-Stokes equations using the finite element technique", *Computers & Fluids*, v. 1, pp. 73–100, 1 1973.

[36] Gresho, P. M., Lee, R. L., Chan, S. T., et al. *Solution of the time-dependent incompressible Navier-Stokes and Boussinesq equations using the Galerkin finite element method*. Springer, 1980.

[37] Hirt, C., Amsden, A., Cook, J. "An arbitrary Lagrangian-Eulerian computing method for all flow speeds", *Journal of Computational Physics*, v. 14, pp. 227–253, 3 1974.

[38] Hughes, T. J., Liu, W. K., Zimmermann, T. K. "Lagrangian-Eulerian finite element formulation for incompressible viscous flows", *Computer Methods in Applied Mechanics and Engineering*, v. 29, pp. 329–349, 12 1981.

[39] Donea, J., Giuliani, S., Halleux, J. "An arbitrary lagrangian-eulerian finite element method for transient dynamic fluid-structure interactions", *Computer Methods in Applied Mechanics and Engineering*, v. 33, pp. 689–723, 9 1982.

[40] Brooks, A. N., Hughes, T. J. "Streamline upwind/Petrov-Galerkin formulations for convection dominated flows with particular emphasis on the incompressible Navier-Stokes equations", *Computer Methods in Applied Mechanics and Engineering*, v. 32, pp. 199–259, 9 1982.

[41] Pironneau, O. "On the transport-diffusion algorithm and its applications to the Navier-Stokes equations", *Numerische Mathematik*, v. 38, pp. 309–332, 10 1982.

[42] Codina, R. "Comparison of some finite element methods for solving the diffusion-convection-reaction equation", *Computer Methods in Applied Mechanics and Engineering*, v. 156, pp. 185–210, 4 1998.

[43] Anjos, G. R. *Solução do Campo Hidrodinâmico em Células Eletroquímicas pelo Método de Elementos Finitos*. MSc Thesis, 2007.

[44] Anjos, G. R. *A 3D ALE Finite Element Method for Two-Phase Flows with Phase Change*. PhD Thesis, 2012.

[45] Sun, P., Zhang, C.-S., Lan, R., et al. "An advanced ALE-mixed finite element method for a cardiovascular fluid–structure interaction problem with multiple moving interfaces", *Journal of Computational Science*, v. 50, pp. 101300, 3 2021.

[46] Darbhamulla, N. B., Jaiman, R. K. "A finite element framework for fluid–structure interaction of turbulent cavitating flows with flexible structures", *Computers & Fluids*, v. 277, pp. 106283, 6 2024.

[47] Palmer, H., Zhao, M., Wu, H., et al. "Comparison between linear and quadratic power take off for a single chamber land-fixed oscillating water column (OWC)", *Renewable Energy*, v. 235, pp. 121329, 11 2024.

[48] Sun, Z., Zeng, Z., Li, J., et al. "An immersed multi-material arbitrary Lagrangian–Eulerian finite element method for fluid–structure-interaction problems", *Computer Methods in Applied Mechanics and Engineering*, v. 432, pp. 117398, 12 2024.

[49] Panton, R. L. *Incompressible Flow*. Wiley, 7 2013.

[50] Batchelor, G. K. *An Introduction to Fluid Dynamics*. Cambridge University Press, 2 2000.

[51] Donea, J., Huerta, A., Ponthot, J., et al. "Arbitrary Lagrangian–Eulerian Methods". 8 2004.

[52] Quarteroni, A. *Numerical Models for Differential Problems*. Springer Milan, 2009.

[53] Fjørtoft, R. "On a Numerical Method of Integrating the Barotropic Vorticity Equation", *Tellus*, v. 4, pp. 179–194, 8 1952.

[54] Wiin-Nielsen, A. "On the Application of Trajectory Methods in Numerical Forecasting", *Tellus*, v. 11, pp. 180–196, 5 1959.

[55] Robert, A. "A stable numerical integration scheme for the primitive meteorological equations", *Atmosphere-Ocean*, v. 19, pp. 35–46, 3 1981.

[56] Bates, J. R., McDonald, A. "Multiply-Upstream, Semi-Lagrangian Advective Schemes: Analysis and Application to a Multi-Level Primitive Equation Model", *Monthly Weather Review*, v. 110, pp. 1831–1842, 12 1982.

[57] Anjos, G., Mangiavacchi, N., Thome, J. "An ALE-FE method for two-phase flows with dynamic boundaries", *Computer Methods in Applied Mechanics and Engineering*, v. 362, pp. 112820, 4 2020.

[58] Xiu, D., Karniadakis, G. E. "A Semi-Lagrangian High-Order Method for Navier–Stokes Equations", *Journal of Computational Physics*, v. 172, pp. 658–684, 9 2001.

[59] Arnold, D. N., Brezzi, F., Fortin, M. "A stable finite element for the stokes equations", *Calcolo*, v. 21, pp. 337–344, 12 1984.

[60] Bai, W. "The quadrilateral 'Mini' finite element for the Stokes problem", *Computer Methods in Applied Mechanics and Engineering*, v. 143, pp. 41–47, 4 1997.

[61] Zienkiewicz, O. C., Taylor, R. L., Zhu, J. Z. *The Finite Element Method: its Basis and Fundamentals*. Elsevier, 2013.

[62] Geuzaine, C., Remacle, J. "Gmsh: A 3-D finite element mesh generator with built-in pre- and post-processing facilities", *International Journal for Numerical Methods in Engineering*, v. 79, pp. 1309–1331, 9 2009.

[63] Ghia, U., Ghia, K., Shin, C. "High-Re solutions for incompressible flow using the Navier-Stokes equations and a multigrid method", *Journal of Computational Physics*, v. 48, pp. 387–411, 12 1982.

[64] Posdziech, O., Grundmann, R. "A systematic approach to the numerical calculation of fundamental quantities of the two-dimensional flow over a circular cylinder", *Journal of Fluids and Structures*, v. 23, pp. 479–499, 4 2007.

[65] Wanderley, J. B., Souza, G. H., Sphaier, S. H., et al. "Vortex-induced vibration of an elastically mounted circular cylinder using an upwind TVD two-dimensional numerical scheme", *Ocean Engineering*, v. 35, pp. 1533–1544, 10 2008.

[66] Decuyper, J., Troyer, T. D., Tiels, K., et al. "A nonlinear model of vortex-induced forces on an oscillating cylinder in a fluid flow", *Journal of Fluids and Structures*, v. 96, pp. 103029, 7 2020.